

An Experimental Investigation
of Thermoacoustic Instability

By

WALTER R. KAMINSKI

A DISSERTATION PRESENTED TO THE GRADUATE COUNCIL OF
THE UNIVERSITY OF FLORIDA
IN PARTIAL FULFILLMENT OF THE REQUIREMENTS FOR THE
DEGREE OF DOCTOR OF PHILOSOPHY

UNIVERSITY OF FLORIDA
1972

DEDICATION

This book is dedicated to my wife and children who have waited so patiently for me to complete my dissertation, for what seemed like such an infinitely long time.

ACKNOWLEDGEMENTS

This program was supervised by Dr. R. K. Irey, to whom I express my deepest gratitude for his guidance and advice throughout the work. I also thank Dr. C. C. Oliver, Dr. R. A. Gater, Dr. U. H. Kerzweg, and Dr. B. S. Thomas for their services on my advisory committee.

My appreciation is extended to the management of the Pratt & Whitney Aircraft Company and the United Aircraft Corporation for their most generous sponsorship of my doctoral program. I am deeply grateful to all those people at the Florida Research and Development Center who have helped me make this program a success. Special thanks to Dr. R. A. Schmidtke for his support and counsel. Also, I would like to thank Mr. G. H. Knowles for his most able assistance in preparing this book.

Finally, I want to especially thank my wife, Mary, for the support that she offered and the many sacrifices that she had to endure during this entire period.

TABLE OF CONTENTS

	PAGE
ACKNOWLEDGEMENTS	iii
LIST OF TABLES	vi
LIST OF FIGURES	ix
NOMENCLATURE	xiii
ABSTRACT	xviii
 CHAPTER	
I. INTRODUCTION AND LITERATURE REVIEW.	1
Introduction.	1
Literature Review	9
Rijke Instability	9
Sondhauss Instability	13
Purpose of Research Program	15
II. TEST APPARATUS AND INSTRUMENTATION.	17
General Description	17
Test Apparatus.	18
Rijke Configuration	20
Sondhauss Configuration	25
Instrumentation Systems	27
Electrical.	27
Acoustic.	30
Temperature	34
Velocity.	38
III. THE EXPERIMENT.	42
Introduction.	42
Experimental Program.	44
Test Summary.	44
Description of Tests.	46
Rijke tests	47
Sondhauss tests	53

	PAGE
Measurements	54
Electrical	54
Acoustic	54
Calibration	56
Measurement uncertainty	61
Gas Temperature	62
Heater Surface Temperature	63
Radiation thermometry	63
Calibration	65
Measurement uncertainty	67
Velocity	69
Hot-wire anemometry	69
Calibration	78
Measurement uncertainty	88
Experimental Procedure	90
IV. RESULTS AND CONCLUSIONS	92
Results of Rijke Experiments	92
Acoustic Measurements	92
Velocity Measurements	99
Heater Surface Temperature Measurements	107
Gas Stream Temperature Measurements	111
Controlled Inlet Flow Tests	115
Results of Sondhauss Experiments	117
Acoustic Measurements	117
Velocity Measurements	122
Gas Stream Temperature Measurements	124
Discussion	127
Conclusions	140
Recommendations	141
APPENDICES	
A. MEASUREMENT UNCERTAINTY THEORY	144
B. MEASUREMENT UNCERTAINTY ANALYSIS	149
C. TABULATED TEST DATA	160
D. DATA REDUCTION	182
BIBLIOGRAPHY	188
BIOGRAPHICAL SKETCH	191

LIST OF TABLES

TABLE	PAGE
1. Rijke Configuration Dimensions From Previous Investigations	20
2. Rijke Configuration Test Summary	45
3. Sondhauss Configuration Test Summary	46
4. Summary of Measurement Uncertainty Calculations for Rijke Configuration Tests	61
5. Summary of Measurement Uncertainty Calculations for Sondhauss Configuration Tests	61
6. Summary of Gas Stream Temperature Measurement Uncertainty	64
7. Summary of Measurement Uncertainty Analysis for the Basic Rijke Test Series	69
8. Laminar Flow Calibration Tube Data	81
9. Summary of Velocity Ratio \tilde{v}/V for Tubes and Probes Used	84
10. Hot-Wire Probe Preliminary Calibration Data Using a DISA 55A01 Constant Temperature Anemometer and a 20 Meter Long Cable	84
11. Estimated Hot-Wire Probe Measurement Uncertainties	89
12. Radial Measurements of Sound Pressure	95
13. Summary of Fundamental and First Harmonic Sound Pressure Data for 1200 Watts of Heater Power	97
14. Correlation of $2\sqrt{2} \pi/U$ and V_b/V_a	106
15. Summary of Calculated Parameters for 1200 Watts	135
B-1. Instrument Bias and Precision Errors	159
C-1. Microphone Data Reduction for Rijke Configuration, Test No. 12	161
C-2. Microphone Data Reduction for Rijke Configuration, Test No. 1	161

TABLE	PAGE
C-3. Microphone Data Reduction for Rijke Configuration, Test No. 2	162
C-4. Microphone Data Reduction for Rijke Configuration, Test No. 3	162
C-5. Microphone Data Reduction for Rijke Configuration, Test No. 4	163
C-6. Microphone Data Reduction for Rijke Configuration, Test No. 17	164
C-7. Microphone Data Reduction for Rijke Configuration, Test No. 18	165
C-8. Microphone Data Reduction for Rijke Configuration, Test No. 18	166
C-9. Microphone Data Reduction for Rijke Configuration, Test No. 18	166
C-10. Microphone Data Reduction for Rijke Configuration, Test No. 16	167
C-11. Microphone Data Reduction for Rijke Configuration, Test No. 16	167
C-12. Hot-Wire Data Reduction for Rijke Configuration, Test No. 1, Fitting 12	168
C-13. Hot-Wire Data Reduction for Rijke Configuration, Test No. 1, Fitting 13	168
C-14. Hot-Wire Data Reduction for Rijke Configuration, Test No. 2, Fitting 12	169
C-15. Hot-Wire Data Reduction for Rijke Configuration, Test No. 2, Fitting 13	169
C-16. Hot-Wire Data Reduction for Rijke Configuration, Test No. 3, Fitting 12	170
C-17. Hot-Wire Data Reduction for Rijke Configuration, Test No. 3, Fitting 13	170
C-18. Hot-Wire Data Reduction for Rijke Configuration, Test No. 4, Fitting 12	171
C-19. Hot-Wire Data Reduction for Rijke Configuration, Test No. 4, Fitting 13	171
C-20. Hot-Wire Data Reduction for Rijke Configuration, Test No. 5, Fitting 14	172

TABLE	PAGE
C-21. Hot-Wire Data Reduction for Rijke Configuration, Test No. 5, Fitting 15	172
C-22. Hot-Wire Data Reduction for Rijke Configuration, Test No. 5, Fitting 16	173
C-23. Hot-Wire Data Reduction for Rijke Configuration, Test No. 5, Fitting Exit	173
C-24. Heater Surface Temperature for Rijke Configuration, Test No. 1, 1000 Watts	174
C-25. Heater Surface Temperature for Rijke Configuration, Test No. 2, 1200 Watts	175
C-26. Heater Surface Temperature for Rijke Configuration, Test No. 3, 1400 Watts	176
C-27. Heater Surface Temperature for Rijke Configuration, Test No. 4, 1600 Watts	177
C-28. Microphone Data Reduction for Sondhauss Configuration Test No. 22	178
C-29. Microphone Data Reduction for Sondhauss Configuration Test No. 20	178
C-30. Hot-Wire Data Reduction, Sondhauss Configuration, Test No. 21, Fitting 13 Sensor Pointing Toward Heater	179
C-31. Hot-Wire Data Reduction, Sondhauss Configuration, Test No. 21, Fitting 13 Sensor Pointing Away from Heater	179
C-32. Hot-Wire Data Reduction, Sondhauss Configuration, Test No. 21, Fitting 14 Sensor Pointing Toward Heater	180
C-33. Hot-Wire Data Reduction, Sondhauss Configuration, Test No. 21, Fitting 14 Sensor Pointing Away from Heater	180
C-34. Hot-Wire Data Reduction, Sondhauss Configuration, Test No. 21, Fitting 15 Sensor Pointing Toward Heater	181
C-35. Hot-Wire Data Reduction, Sondhauss Configuration, Test No. 21, Fitting 17 Sensor Pointing Toward Heater	181

LIST OF FIGURES

FIGURE		PAGE
1.	Simple configurations displaying thermoacoustic instability.	3
2.	Vector diagram illustrating Rayleigh's Criterion.	9
3.	Double walled (cooled) Rijke configuration.	19
4.	Rijke thermoacoustic instability rig assembly drawing.	22
5.	Heater assembly drawing.	23
6.	Sondhauss thermoacoustic instability rig assembly drawing.	26
7.	Schematic diagram of electrical system.	29
8.	Bruel and Kjaer 1/4 and 1/8 inch condenser microphone assemblies.	31
9.	Schematic drawing of sound measuring system.	32
10.	Schematic diagram of temperature and velocity measuring systems.	35
11.	Shielded gas temperature probe assembly drawing.	36
12.	Hot-wire probes used in experimental program.	40
13.	Hot-wire probe positioning device employing a dial indicator to measure probe position.	41
14.	Rijke configuration test apparatus and associated instrumentation in position for testing.	43
15.	Sondhauss configuration test apparatus in position for testing.	43
16.	Location of probe fittings on Rijke test apparatus.	48
17.	Location of probe fittings on Sondhauss test apparatus.	49
18.	Test setup for controlled inlet flow tests.	51
19.	Schematic construction of a condenser microphone cartridge.	55

FIGURE	PAGE
20. Microphone probe extension tube assembly.	57
21. Arrangement for the calibration of a probe tube.	59
22. Microphone sensitivity change due to damping of probe extension tube.	60
23. Heater foils partially fill reticle.	65
24. Heater surface temperature calibration.	68
25. Typical hot-wire anemometer calibration curve.	74
26. Typical hot-wire anemometer sensitivity curve.	75
27. Hot-wire probe fluctuating voltage output as a function of time mean velocity and frequency after Rasmussen (31).	76
28. Hot-wire calibration fixture.	80
29. Flow schematic diagram of hot-wire probe calibration system.	82
30. Hot-wire sensor located at centerline of laminar flow tube.	83
31. Static calibration curves for hot-wire probes 1, 5 and 6.	86
32. Static calibration curves for hot-wire probes 1H and 2H.	87
33. Variation of maximum sound pressure level and frequency with heater power input for the Rijke configuration.	93
34. Axial variation of sound pressure in the Rijke apparatus for several values of heater power.	95
35. Spectral distribution of sound pressure level showing the fundamental and first harmonic frequencies in the Rijke apparatus.	96
36. The effects of cooling on the generation of sound in the Rijke apparatus.	100
37. Variation of centerline time mean and fluctuating velocity with heater power for the Rijke configuration.	102
38. Time mean and fluctuating velocity profiles for the Rijke device for 1200 watts of heater power.	103
39. Oscilloscope photographs of sound pressure and fluctuating velocity for various positions along the Rijke apparatus at 1200 watts of heater power.	105

FIGURE		PAGE
40.	Photographs of heater taken from above exit plane of Rijke apparatus.	108
41.	Location of targets on heater photograph for 1600 watts.	110
42.	Equi-area averaged heater surface temperature distribution for Basic Rijke Test Series.	112
43.	Centerline gas stream temperature distribution for the Basic Rijke Test Series.	113
44.	Time mean gas stream temperature profiles for the Rijke device for 1200 watts of heater power.	114
45.	Gas temperature profile in wake region of heater foils.	115
46.	Results of controlled inlet flow tests on Rijke configuration.	116
47.	Variation of maximum sound pressure level and frequency with input electrical power for Sondhauss configuration.	119
48.	Axial variation of sound pressure in the Sondhauss apparatus.	120
49.	Transition from Sondhauss mode to Rijke mode instability in same apparatus by gradually varying inlet area.	121
50.	Cross-sectional view through 55F33 hot-wire probe at sensor showing wake region formed by support prong when sensor points away from the direction of the flow.	123
51.	Illustration of velocity profiles at tube exit for the case of hot-wire sensor pointing toward and away from heater.	125
52.	Time mean and fluctuating velocity profiles for Sondhauss configuration for 700 watts of heater power.	125
53.	Time mean gas stream temperature profiles for the Sondhauss device at 700 watts of heater power.	126
54.	Centerline gas temperature profile through Sondhauss apparatus.	128
55.	Axial variation of averaged values of sound pressure, phase angle and time mean and fluctuating velocity for the Rijke configuration.	130
56.	Relationship between sound pressure and velocity waves in an open-open tube.	131

FIGURE	PAGE
57. Spatial distribution of phase angle, sound pressure and fluctuating velocity for an open-open tube.	132
58. Vector diagram for acoustic parameters.	133
59. Calculated air flow rate through apparatus for the Basic Rijke Test Series.	134
60. Real and imaginary parts of the function T_m for a flat ribbon heater, after Merk (15).	137
A-1. Precision error.	145
A-2. Bias error.	145
A-3. Measurement uncertainty.	148
B-1. Precision error in ΔT correction.	153
D-1. Geometry for mass flow calculation.	186

NOMENCLATURE

Symbol	Description	Units
A_1	Maximum Amplitude of Sound Pressure Wave	psia
A_w	Constant Defined by Equation [15]	amps ²
a_o	Speed of Sound	ft/sec
B	Bias Error Limit (Takes Dimension of Variable Assigned by Subscript)	
B_w	Constant Defined by Equation [16]	amps ² /(ft-sec) ^{$\frac{1}{2}$}
C	Unit Conversion Constant in Equation [12]	$\frac{\text{watts-ft-hr}}{\text{Btu-in.}}$
C_c	Constant Defined by Equation [B-4]	ft-lb _f /lb _m -in ²
C_n	Curve Fit Constant, n = 1, 2 ..., (See Appendix D)	
C_p	Specific Heat of Fluid in Thermoacoustic Device	Btu/lb _m -deg F
C_w	First Temperature Coefficient of Resistivity	ohms/deg F
D	Duct Inner Diameter	in.
D_L	Laminar Flow Tube Inner Diameter	in.
E_m	Real Part of Function T_m	dimensionless
ΔE	Energy Transferred to Fluid per Cycle	Btu/in ² -sec
$F(r)$	Function Defined by Equation [D-9]	
F_M	Imaginary Part of Function T_m	dimensionless
f_o	Fundamental Frequency	Hz
f_1	First Harmonic Frequency	Hz
$G(r)$	Function Defined Equation [D-13]	
g	Gravitational Constant, 32.17	lb _m -ft/lb _f -sec ²

Symbol	Description	Units
H	Overheat Ratio	dimensionless
h	Fluid Enthalpy	Btu/lb _m -deg F
I	Electrical Current	amps
I _s	Acoustic Intensity	watts/in ²
J	Energy - Work Constant, 778.16	ft-lb _f /Btu
k	Thermal Conductivity of Fluid	Btu/hr-ft-deg F
k _f	Thermal Conductivity of Fluid Evaluated at Film Temperature	Btu/hr-ft-deg F
k _n	Curve Fit Constant, n = 1, 2 (See Appendix D)	
L	Length of Thermoacoustic Device	in.
L _e	Effective Length of Thermoacoustic Device	in.
L _w	Hot-Wire Sensor Length	in.
\dot{m}	Mass Flow Rate Through Thermoacoustic Device	lb _m /sec
\dot{m}_L	Mass Flow Rate Through Laminar Flow Tube	lb _m /sec
N	Number of Measurements	dimensionless
N _p	Curve Fit Normalization Parameter	
n	Exponent On Time Mean Velocity in Equation [17]	dimensionless
P	Fluid Pressure	psia
(Pr) _f	Prandtl Number Evaluated at Film Temperature	dimensionless
P _{av}	Average Sound Pressure in Heater Zone	psia
P _{ori}	Orifice Upstream Pressure	psia
ΔP _{ori}	Orifice Differential Pressure	psi
P _o	Steady Part of Fluid Pressure Defined by [5]	psia
p	Sound Pressure	psia
P _{amb}	Ambient Pressure	psia

p_1	Sound Pressure Upstream of Heater	psia
p_2	Sound Pressure Downstream of Heater	psia
Q	Heat Transfer	Btu/sec
q	Fluctuating Heat Transfer	Btu/sec
q'	Component of Fluctuating Heat Transfer in Phase with Sound Pressure	Btu/sec
R	Gas Constant	ft-lb _f /lb _m -° R
$(Re)_f$	Reynolds Number Evaluated at Film Temperature	dimensionless
R_r	Hot-Wire Electrical Resistance Evaluated at Reference Temperature, T_r	ohms
R_w	Hot-Wire Electrical Resistance Evaluated at T_w	ohms
r	Radius	inches
Δr	Radial Increment	in.
SPL	Sound Pressure Level	db
SPV	Sound Pressure Voltage Signal	volts
S_{hw}	Hot-Wire Sensitivity	volts/ft/sec
S_m	Microphone Sensitivity	db
s	Precision Index	dimensionless
T_{av}	Bulk Averaged Fluid Temperature in Thermo-acoustic Device	deg F
T_{blk}	Fluid Temperature at Hot-Wire Calibration Block	deg F
T_g	Gas Temperature	deg F
T_o	Steady Part of Temperature Defined by Equation [5]	deg F
T_h	Corrected Heater Surface Temperature	deg F
$T_{h'}$	Indicated Heater Surface Temperature	deg F
ΔT	Heater Surface Temperature Correction from Figure 24	deg F

Symbol	Description	Units
T_m	Parameter Defined by Equation [28]	dimensionless
T_{ori}	Orifice Fluid Temperature	deg F
T_r	Reference Temperature for Electrical Resistance	deg F
T_w	Hot-Wire Sensor Temperature	deg F
U	Time Mean Velocity	ft/sec
U^*	Velocity Defined in Figure 25	ft/sec
U_{av}	Bulk Averaged Fluid Velocity in Thermo-acoustic Device	ft/sec
U_{cal}	Time Mean Velocity, Hot-Wire Calibration	ft/sec
U_o	Steady Part of Velocity Defined by Equation [5]	ft/sec
u	Fluctuating Velocity	ft/sec
V	Voltage	volts
V_{ac}	Anemometer AC Bridge Voltage	volts
V_{DC}	Anemometer DC Bridge Voltage	volts
V_o	Hot-Wire Zero Velocity Voltage	volts
\tilde{v}	Velocity Defined in Figure 30	ft/sec
\bar{v}	Velocity Defined in Figure 30	ft/sec
x	Distance Variable	in.
x_h	Position of Heater Relative to Inlet Plane	in.
α	Percent Reticle Filled by Target	dimensionless
β_{ori}	Orifice Flow Calibration Coefficient	dimensionless
γ	Ratio of Specific Heats	dimensionless
ϵ_w	Heater Surface Emissivity	dimensionless
ϵ_F	Estimated Error in Function F (Takes Dimension of Function F)	

Symbol	Description	Units
$\eta_{t.a.}$	Thermoacoustic Efficiency	dimensionless
θ	Fluctuating Temperature	deg F
ν	Parameter Defined by Equation [27]	in^{-1}
ρ	Density of Fluid in Thermoacoustic Device	lb_m/ft^3
$\bar{\rho}$	Fluctuating Density	lb_m/ft^3
ρ_o	Steady Part of Density Defined by Equation [5]	lb_m/ft^3
ρ_{av}	Bulk Averaged Fluid Density in Thermoacoustic Device	lb_m/ft^3
σ	Precision Error (Takes Dimension of Variable Assigned by Subscript)	
ϕ	Angular Position	degrees
x_i	Measurement	dimensionless
\bar{x}	Average Value of Measurement	dimensionless
ψ	Phase Angle	degrees
ψ_{p_2}	Phase Angle Between Sound Pressures Upstream and Downstream of Heater	degrees
ψ_{av}	Phase Angle Between Fluctuating Heat Transfer and the Average Sound Pressure in Heater Zone	degrees
ψ_r	Phase Angle Between Sound Pressure and Fluctuating Heat Transfer	degrees
Ω	Measurement Uncertainty (Takes Dimension of Variable Assigned by Subscript)	
Δ_f	Microphone Sensitivity Frequency Correction	db
Δ_{amb}	Microphone Sensitivity Ambient Pressure Correction	db

Abstract of Dissertation Presented to the
Graduate Council of the University of Florida in Partial Fulfillment
of the Requirements for the Degree of Doctor of Philosophy

AN EXPERIMENTAL INVESTIGATION
OF THERMOACOUSTIC INSTABILITY

By

Walter R. Kaminski

December, 1972

Chairman: Professor Richard K. Irey
Major Department: Mechanical Engineering

An experimental research program was conducted to investigate the phenomenon of thermoacoustic instability. To gain a basic understanding of the processes involved, two simple types of thermoacoustically unstable systems, the Rijke and Sondhauss devices, were built and tested. Rijke type instability occurs in a vertically oriented open-open tube possessing an internal heat source which forces air to flow upward through the tube by buoyancy effects. Sondhauss type instability occurs in a gas filled, vertically oriented, closed-open tube, where heat is added internally or externally at the closed end. The net flow for this system is zero. The frequency of the resulting acoustic oscillations corresponds to the fundamental mode of each system.

Two goals were established at the outset of this research. The primary goal was to experimentally investigate the thermoacoustic transduction process by measuring time mean and fluctuating pressures, velocities and temperatures. Emphasis was placed on the "near field" of the heat source where both theory and data were lacking. A secondary goal was to experimentally investigate the relationships existing be-

tween the Rijke and Sondhauss modes of instability.

The majority of tests were conducted using the Rijke apparatus to study the energy transfer process between the thermal and acoustic fields. Electrical power levels ranged from 900 to 1600 watts. Test results showed that thermoacoustic transduction is promoted when a steep gas temperature gradient is established which allows interaction between the fluctuating thermal and acoustic energy modes with a subsequent energy transfer.

During a series of controlled inlet flow tests using the Rijke device, the free convection configuration, that is, unaugmented by externally supplied flow, was found to be most efficient in terms of sound production. Any attempts to decrease or to add to the free convection flow resulted in a reduced sound output. These tests also showed that the Rijke device is unstable over a very narrow range of inlet velocities.

A particularly interesting result showed that both Rijke and Sondhauss modes of thermoacoustic instability can occur in the same device, operating at the same power level, simply by changing inlet end conditions. Therefore, these two types of instabilities which have been historically treated as distinct, are really one and the same phenomenon.

Non-linear behavior in the sound output of both Rijke and Sondhauss devices was observed as heater power was progressively increased. The sound output was found to be saturated above 1400 watts for the Rijke device and above 800 watts for the Sondhauss device. This behavior is not predictable using linear acoustic theory.

CHAPTER I

INTRODUCTION AND LITERATURE REVIEW

Introduction

Numerous instances of oscillatory phenomena, often accompanying the operation of gaseous systems containing a thermal energy source, have been reported during the past one and one-half centuries. The systems referred to were considerably varied in their construction and included various types of thermal energy sources such as flames, hot parts immersed within the fluid or steep temperature gradients along flow confining channels.

Byron Higgins (1)¹ appears to have made the first recorded observation of an organ-pipe oscillation caused by combustion, in 1777, when he enclosed a hydrogen diffusion flame in a large tube open at both ends. This type of phenomenon has subsequently been referred to as the "singing flame ." In 1850, Sondhauss (2) published the results of an experimental study of heat-generated sound often observed by glass blowers when blowing a bulb on the end of a narrow tube. Rijke (3), in 1859, reported results of an experiment where sound was generated in a vertically oriented pipe, open at both ends and containing a heated grid in the lower half of the tube. In the years that followed these early experiments, oscillatory performance of domestic and commercial oil and gas fired combustion devices were often reported. The development of

¹Numbers in parenthesis designate references which are found in the Bibliography.

rocket and jet engine combustion chambers after World War II uncovered various new types of heat-generated oscillations often referred to as combustion instability. The effects of these combustion chamber oscillations often caused destruction or degradation in performance. Similar thermally induced oscillations have been observed in certain cryogenic experiments where a gas column has a large temperature gradient imposed along its length (4, 5, 6, 7). More recently, during supercritical pressure heat transfer testing of JP type fuels, similar oscillatory behavior was observed and reported (8).

The situations described above are examples of thermoacoustic instability and relate to devices where the pressure fluctuations are maintained by a heat source of sufficient strength. These unstable devices possess the characteristic that small disturbances, random in nature, can grow in amplitude until the energy input to the system is exactly balanced by the losses of the system per cycle of oscillation. These losses are due to friction, heat transfer and thermal and acoustic radiation. A steady heat source supplies the necessary energy for sustaining oscillations if correctly positioned so that the fluctuating heat transfer is in phase with the sound pressure for the major part of a cycle of oscillation. The oscillations are of an acoustic nature, that is, sound is produced by the pressure fluctuations. The phenomenon is then one of transduction of thermal energy into acoustic energy.

Thermoacoustic instability has been separated into two distinct types, Rijke type and Sondhauss type. Rijke type instability occurs in a flowing system possessing an internal heat source and positioned at a location where the heat transfer is in phase with the acoustic pressure. Figure 1a shows the simplest of configurations demonstrating the Rijke

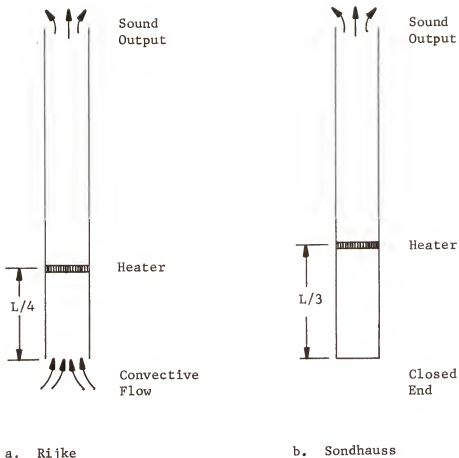


Figure 1. Simple configurations displaying thermoacoustic instability.

effect where heat is supplied by an electric grid heater and air is caused to flow through the tube by buoyancy effects. The flow can be forced by a fan or pump in some of the more complex systems which may also contain other physical ramifications.

Numerous experiments have shown that the maintenance of the oscillations depends on the position of the heater. It has been observed that the strongest oscillations occur when the grid is approximately one-quarter of the way from the bottom end of the tube. For heater positions in the upper half of the tube damping instead of driving results. By supplying heat to the grid from a source of electrical power, the oscillations can be maintained indefinitely.

Sondhauss mode instability occurs when heat is added internally or externally to the closed end of a gas filled pipe having at least one closed end and having no net flow of gas through the pipe. Figure 1b shows a simple Sondhauss pipe with heat added near the closed end. Again, as in the previous case, many ramifications of this physical system are possible.

Experiments with Sondhauss pipes have indicated that the sound output maximizes when the heater is located one-third of the distance from the closed end. Sondhauss devices have varied considerably in the configuration of the closed end. Some Sondhauss devices had bulb ends whereas others had volumes of various shapes. Like the Rijke device, the Sondhauss device will oscillate indefinitely when the heater is supplied by an electrical power source. It becomes apparent at this stage that many features of the Rijke and Sondhauss devices are similar, although, historically they have been treated as separate types of thermoacoustic instability.

Thermoacoustic instability depends upon two processes. The first process involves the conversion of thermal energy to acoustic energy and will be referred to as thermoacoustic transduction. The second process involves the phase relationship between the fluctuating heat transfer and sound pressure that is necessary to sustain the oscillations. This process will be referred to as maintenance of oscillations.

As a starting point in trying to understand thermoacoustic instability and the concepts underlying the thermoacoustic transduction process and maintenance of oscillations, an explanation of the operation of an electrically supplied Rijke tube will be made. Below a certain level of electrical power, oscillations cannot grow because the heat

input does not equal or exceed the system losses which are composed of viscous losses, heat losses and thermal and acoustic radiation losses out the open ends. As the power is increased, a thermal field is established in the tube which is characterized by a temperature peaked region near the heater. This region is set up by free convective flow resulting from heating a vertically oriented air column. A random sound source such as speech, a handclap or snap of the fingers introduced near the heated tube causes oscillations to grow in time and to finally reach a limit cycle where the heat input balances the systems losses. Internally what happens is this. Sound waves entering the tube from the bottom, for example, encounter the temperature peaked region and extract energy from it. A portion of the wave is reflected back toward the bottom end (inlet end) while the remainder is transmitted through the steep temperature gradient region where amplification occurs. The upward traveling wave eventually reflects off the top or exit end and travels toward the heater while a portion is transmitted into the room and lost to the system. A similar occurrence takes place at the inlet end. If the heat source is strategically located within the tube, the reflected waves traveling toward the heater are energetically reinforced upon passing through the heater zone and overcome losses. A standing wave pattern is eventually established and sound, which is predominantly at the fundamental frequency of the tube, is produced.

From this discussion we recognize that thermoacoustic transduction involves the transfer of energy from the fluctuating thermal field to the acoustic field, in a region of a steep temperature gradient which is steady and fixed in space. The oscillations are maintained when a heater, of sufficient strength, is located in a position where fluctuating heat transfer can be properly phased with the acoustic waves. Later,

Rayleigh's Criterion for the maintenance of oscillations will be presented because of its widespread acceptance as a reasonable explanation of the process involved.

The essential features of thermoacoustic transduction can be further appreciated by studying the simple case of an invicid, one-dimensional fluid flow of a perfect gas with constant properties. Conservation equations for mass, momentum and energy and the equation of state follow, subject to the above restrictions:

Mass:

$$\frac{\partial \rho}{\partial t} + \frac{\partial (\rho U)}{\partial x} = 0 \quad [1]$$

Momentum:

$$\rho \frac{\partial U}{\partial t} + \rho U \frac{\partial U}{\partial x} = - \frac{\partial P}{\partial x} \quad [2]$$

Energy:

$$C_P \rho \frac{\partial T}{\partial t} + \rho C_P U \frac{\partial T}{\partial x} = k \frac{\partial^2 T}{\partial x^2} \quad [3]$$

State:

$$P = \rho R T \quad [4]$$

In the above equations the symbols have their customary meaning and are defined in the Nomenclature section. Following Mawardi's (9) derivation, a perturbation technique is used to obtain a linearized set of equations of motion. Density, pressure, temperature and velocity are expressed as in terms of a steady component plus a fluctuating part. A sinusoidal time dependence is also assumed.

$$\begin{aligned} \rho &= \rho_0 + \bar{\rho} e^{-i\omega t} \\ T &= T_0 + \bar{\theta} e^{-i\omega t} \\ U &= U_0 + \bar{u} e^{-i\omega t} \\ P &= P_0 + \bar{p} e^{-i\omega t} \end{aligned} \quad [5]$$

After some manipulation Mawardi obtains the following pair of equations:

$$\frac{\partial^2 \bar{u}}{\partial x^2} + \frac{\omega^2 \rho_o}{p_o} \bar{u} = i\omega \frac{\partial}{\partial x} \left(\frac{\theta}{T_o} \right) \quad [6]$$

$$\frac{\partial^2 \theta}{\partial x^2} - \frac{i\omega \theta}{K} - a^2 \frac{\partial \theta}{\partial x} = \bar{u} \frac{\partial T_o}{\partial x} \quad [7]$$

In equations [6] and [7], $K = k/\rho c_p$ and $a = U_o \rho c_p/k$.

It is now apparent by inspection of equation [7] that the appearance of the fluctuating velocity \bar{u} implies an interaction between the fluctuating temperature field, θ , and the fluctuating velocity field \bar{u} . Another point of interest is that the right-hand side also contains the quantity $\partial T_o/\partial x$, thus proving the statement that strong temperature gradients will tend to increase the interaction.

We now examine the concepts underlying the process of maintenance of oscillations. Lord Rayleigh stated his criterion for maintenance of oscillations without any mathematical proof in 1878 when he published his now classic works on sound (10). However, it was not until the 1950's that his criterion was put in terms of a precise mathematical statement by Putnam and Dennis (11) and Chu (12). As background for the work which follows, it is worthwhile to give Rayleigh's statement of his criterion here. Rayleigh stated:

If heat be given to the air at the moment of greatest condensation or taken from it at the moment of greatest rarefaction, the vibration is encouraged. On the other hand, if heat is given at the moment of greatest rarefaction or abstracted at the greatest condensation the vibration is

discouraged; however, there is no effect in encouraging or discouraging the vibration if the air concerned is at a loop, that is, a place where the density does not vary, or if the communication of heat is the same at any stage of rarefaction as at the corresponding stage of condensation.

Chu's mathematical statement of the Rayleigh Criterion is given by equation [8].

$$\Delta E_{\text{cycle}} = \left(\frac{\gamma_1 - 1}{\gamma_1} \right) \frac{\pi D^2}{4 P_1} \int_{\text{cycle}} p \, q \, dt \quad [8]$$

Note that all properties are referred to the upstream side of the heater which are essentially those corresponding to ambient conditions. The symbols p and q refer to fluctuating pressure and heat transfer, respectively. Thus equation [8] clearly states that the local heat addition or abstraction must be positively correlated with a naturally available pressure fluctuation in the system to produce spontaneous amplification of that particular pressure fluctuation. If $\Delta E > 0$, disturbances will be amplified in time, if $\Delta E < 0$, disturbances will be damped and if $\Delta E = 0$, disturbances will be neither damped nor amplified in time.

As a final elaboration of Rayleigh's Criterion, we turn to Kerwin's work (13). Kerwin paraphrased Rayleigh's Criterion in a particularly useful manner, one which will be used in Chapter IV. "When heat is added periodically to an oscillatory system, the oscillations tend to be driven if the periodic part of the heat addition rate has a component in phase with the acoustic pressure, and tend to be damped if the heat addition rate has a component out of phase with the pressure." The

meaning of the above statement becomes clear when examining the vector diagram shown in figure 2.²

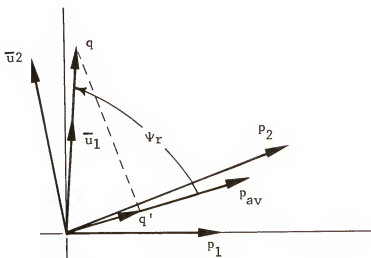


Figure 2. Vector diagram illustrating Rayleigh's Criterion.

Figure 2 shows that amplification occurs when $|\psi_r| < \pi/2$ and damping occurs when $|\psi_r| > \pi/2$.

Literature Review

The literature review contained herein is very brief and is only intended to introduce the reader to some of the work which is referenced in the chapters that follow. An extensive literature review was conducted by Putman and Dennis (11) and Feldman (16, 17). Feldman's review of both Rijke and Sondhauss instability is especially good.

Rijke Instability

Kerwin presented a study of the Rijke oscillation in his Sc. D. dissertation (13). This work included both a theoretical and an experimental investigation, specifically to explain the onset and decay of

²Actually, the fluctuating heat transfer lags the fluctuating velocity as pointed out by Carrier (14) and Merk (15). This topic will be discussed at length in Chapter IV.

oscillations. The theoretical model for small signal oscillations, incorporating a heater of finite thickness, enabled the calculation of the phase difference between the periodic heat addition rate and the acoustic pressure in the heater zone. This resulted in driving or damping of the oscillations in agreement with Rayleigh's Criterion.

Kerwin's experimental work was excellent. He employed a square tube (2 inches by 2 inches) which could be varied in length from 18 to 72 inches, giving a variable heater relative position. Each end of the duct was fitted with acoustically lined plenum chambers to nullify room coupling effects. The experiments were conducted under steady state conditions to determine growth and decay of oscillations by introducing losses into the system. The losses were introduced by progressively opening holes in the sides of the duct walls just downstream of the heater. Compared to experimental results, his theory was qualitatively correct but quantitatively he was off by a factor of approximately 10.

Carrier (14) performed a theoretical study of the Rijke tube. Carrier's chief contribution to the general theory of thermoacoustic instability was an analysis describing the fluctuating heat release from a heated strip immersed in a pulsating flow. The object of his work was to arrive at an estimate of the interaction between the thermal and acoustic fields in the vicinity of the heat source. Carrier's heater strip model has been the starting point for several analyses because no others were available.

Mawardi wrote two papers dealing with the thermoacoustic transduction process. In 1955, he wrote a theoretical paper dealing with the interaction of thermal and acoustic fields in a duct containing a heat source which was immersed in a potential flow (9). This analysis,

restricted to invicid fluids, shows that the magnitude of the sound wave is reinforced as it propagates through the thermal field. The paper very clearly shows that thermoacoustic transduction takes place in a region of a steep temperature gradient and that the sound waves amplify upon leaving the thermal field.

In a second paper written in 1956, Mawardi reviews the general area of aero-thermoacoustic (18). Mawardi used an analysis, first presented by Kováznay (19), to show that the general equations for conservation of mass, momentum and energy and the equation of state lead to the identification of three modes of energy associated with the fluid when perturbations are introduced. The three modes of energy are vorticity, entropy and compression. Interaction between any of these modes produces sound. Interaction of the entropy and compression modes leads to thermoacoustic oscillations such as the Rijke phenomenon.

Mawardi critiqued a number of papers in the area of aero-thermoacoustics. He concluded his paper by stating that the main features of the Rijke phenomena are essentially understood. However, a general treatment of the Rijke phenomena for large amplitudes of motion and the ability to predict the intensity of sound even for small amplitudes, still awaits a solution.

In a manner very similar to Carrier and Kerwin, Merk also analyzed the Rijke phenomenon by requiring that the pressure, temperature and mean velocity satisfy the conservation equations (15). Transfer functions for a wire gauze and flat ribbon heater were developed. Merk found that the solution to his characteristic equation leads to a proper description of the major features of the phenomenon. Neutral curves for the fundamental frequency are presented which show that for excitation to occur, the Strouhal number of the heater must have a value within a critical

range. This means that for any given dimensions of the tube and heater, there corresponds a critical range of values of mean velocity over which there should be no sound generation. Neutral curves for the first harmonic are also given which show that it is possible to excite both frequencies if the heater is located in a prescribed position. Several investigators following Merk have concluded that his analysis predicts too wide a range of mean flow velocities over which oscillations will occur.

Malling (20) presented an analysis which described many of the important features of the Rijke tube but was much simpler than the formal approaches discussed previously. Malling started with the wave equation including a heat source term to perform a small signal analysis of the Rijke phenomenon. He assumed that the heat source could be represented by a delta function in space, and the fluctuating part of the heat addition per unit mass was proportional to the fluctuating velocity of the gas just upstream of the heater. Carrier's heat transfer function for a ribbon heater was used in the analysis to obtain a relation between fluctuating heat release and fluctuating velocity. The resulting solution to Malling's analysis gave good agreement with his experimental observations.

Malling's experimental apparatus consisted of a brass pipe, 36 inches long by 3.5 inches in diameter that contained a nichrome ribbon heater and was mounted over a large plenum chamber at the inlet end. A blower supplied the test apparatus with air during testing. A flow meter was used to measure the flow from which the inlet velocity was calculated. Crude measurements of heater surface temperature were made using a temperature sensitive paint. Three levels of heater power were

investigated. One of the main results of his test program was the measurement of the upper cut-off velocity for each heater power level.

Friedlander (21) performed experiments in what he called a horizontal Rijke tube with closed ends (an inversion of the classical open-ended apparatus) which was provided with forced convection into and out of the closed ends. The reason for the closed ends was to eliminate radiation end losses and standing wave coupling with the room. The tube was fitted with movable closed ends which allowed a variety of changes in the dimensions of the tube, while still maintaining control of the operating conditions. Experimental data agreed well with previous theoretical work performed by Kerwin and Maling.

Some of the more important results of his experiments showed that tube length as well as velocity are critical factors in enabling the heater to drive the oscillations. For a constant heater position the amplitude of the sound pressure level varies directly with tube length. For a constant tube length, the amplitude increases with increasing inlet velocity until it reaches a maximum; thereafter, it decreases until it is damped out. Another interesting fact which was experimentally observed was that the longer the time spent by a single particle of the oscillating gas in translation through the heater region, the greater the sound pressure. No explanation was given for this phenomenon.

Sondhauss Instability

Sondhauss instability has not received as much attention as the corresponding Rijke instability. With the exception of Sondhauss's initial work only a handful of authors have contributed to the subject during the years which followed (22, 23, 24, 25, 26). Only Feldman's work (24, 25) will be reviewed here.

An extensive experimental and analytical investigation of Sondhauss type thermoacoustic instability was conducted by Feldman and reported in his Ph.D. dissertation (24). Later, Feldman and Carter presented a paper on the same subject matter (25).

This paper describes the experiments and offers a physical explanation for the heat exchange mechanism causing Sondhauss thermoacoustic instability. Two types of Sondhauss apparatus were fabricated and tested. The first consisted of a Pyrex glass tube with a bundle of small diameter glass tubes inserted adjacent to and in contact with an electrical heater. External cooling was supplied in order to increase the sound intensity. The second type of Sondhauss pipe was a closed, double ended configuration which consisted of two pipes of the first kind but joined at their open ends. This configuration produced a "push-pull" type of oscillator.

Based upon results of experimental studies, Feldman attributes the driving mechanism to two separate components. Driving is caused by simple periodic thermal expansions and also by expansions due to mixing of hot and cold gasses in a pipe. The driving process was found to be analogous to that occurring in a regenerative heat engine. The Sondhauss oscillator operates on a definite thermodynamic cycle and requires a steady high power density heat source at high temperature and a heat sink at low temperature. A tube bundle or other restriction of low thermal conductivity is required to separate the heat source and heat sink, to provide a small regenerative effect, and to provide a phase shift between the acoustic pressure and velocity waves. An interesting result was observed during testing, a toroidal flow pattern was observed at the tube exit where a continuous inflow occurred at the tube periphery and an outward flow resulted along the axis of the pipe. The inflow was

observed to extend only 1 or 2 inches into the interior of the pipe.

Feldman also performed an extensive analog computer study which gave good agreement with test data. Sound pressure level and frequency of the acoustic output was accurately predicted.

Purpose of Research Program

After reviewing the works of other researches, two goals were established for this dissertation. The primary goal was to experimentally investigate the thermoacoustic transduction process by measuring pertinent time mean and fluctuating parameters, especially in the near field of the heat source. A secondary goal was to experimentally investigate the relationships existing between the Rijke and Sondhauss modes of instability.

The following objectives were planned to achieve the stated goals.

1. Probing studies will be performed on the thermoacoustically unstable Rijke device to measure time mean and fluctuating components of pressure, temperature and velocity. Data will be acquired in both the axial and radial directions with emphasis on the near field of the heat source.
2. Heater surface temperatures will be measured for various levels of electrical power input to the heater.
3. Heat losses will be measured for the Rijke device in order to estimate the thermoacoustic efficiency.
4. The effect of varying the inlet mass flow rate through the Rijke device will be investigated in an attempt to determine those conditions which maximize the sound pressure level in the device.
5. An attempt will be made to generate both Rijke and Sondhauss type instability in the same device with the same heater power

level just by changing inlet and end conditions from open (Rijke) to closed (Sondhauss).

6. Time mean and fluctuating measurements of pressure, temperature and velocity will be taken in the Sondhauss device at one heater power level to compare with Rijke data. An attempt will be made to find similarities and differences between Rijke and Sondhauss type instability.

CHAPTER II

TEST APPARATUS AND INSTRUMENTATION

General Description

In order to accomplish the objectives stated in the last section of Chapter I, it was necessary to design and fabricate a certain amount of hardware and to select and adapt the appropriate instrumentation. This chapter is devoted to a discussion of the test apparatus and instrumentation that was used.

The test hardware basically consisted of an upstream and downstream duct, heater assembly, extra spacer sections to allow variation in length, and hardware to change end conditions. Flexibility was designed into the hardware by making all major parts of uniform internal diameter with connecting flanges. Thus, the Sondhauss configuration could be built up from the Rijke configuration by simply adding spacer sections to maintain certain geometric proportions and closing the inlet end. Additional hardware was fabricated to adapt the various instruments to the test apparatus.

To investigate the phenomenon of thermoacoustic instability experimentally, temperature, pressure, and velocity measurements had to be made throughout the test apparatus. The instrumentation that was used to make these measurements was, for the most part, conventional; however some innovation was necessary to adapt the instruments to particular situations.

Test Apparatus

The experimental program was primarily formulated to investigate Rijke mode instability; however, several Sondhauss mode tests were also planned. For this reason, the hardware was designed for the optimum Rijke configuration but with the capability of being simply converted to the Sondhauss configuration.

A brief account of the historical development of the hardware is now presented to explain the reasons for selecting the configurations that will be subsequently discussed. The first set of Rijke hardware was fabricated with a cooling means provided for measuring the heat losses from the test apparatus. Thermal energy transferred from the heater to the fluid could then be estimated since both input electrical power and heat loss were measured quantities. Figure 3 shows the cooled Rijke configuration in which coolant was circulated through an annular passage formed between two concentric tubes. Inlet and outlet manifolds were provided with fittings for insertion of thermocouple probes. The upstream ducts could be individually cooled or could be connected in series by the use of connecting tubing as shown in figure 3 .

Design calculations indicated that air or gaseous nitrogen would be a better choice of coolant than water because of the greater temperature rise possible for a given amount of heat transferred. Subsequent pressure testing of the cooling system, using gaseous nitrogen, disclosed extensive leakage around each of the instrumentation adaptors. All of the leaks were internal, that is, from the cooling jacket to the chamber that was formed by the two ducts. Weld repair of all 15 instrumentation adaptors was estimated to be very costly so an attempt



Figure 3. Double walled (cooled) Rijke Configuration.

was made to repair the leaks by flowing sodium silicate followed by a curing cycle. After several attempts the holes were sealed to the point where it was feasible to use water as the coolant. Care had to be taken to maintain as low a pressure as possible while circulating the water through the cooling jacket. However, the capability of measuring heat losses accurately was lost due to the resulting small temperature rise.

Because of the problems encountered with the cooled hardware, a new set of upstream and downstream ducts were fabricated which were uncooled in the sense of forced convection. The cooled hardware was relegated to a minor role in the Rijke configuration testing, that of making some comparative measurements of cooling versus no cooling. However, the cooled hardware was used in the Sondhauss configuration for reasons which will be apparent later.

Rijke Configuration

This section contains a description of the apparatus used to study Rijke mode instability. Since the objective of this program was to investigate the phenomenon of thermoacoustic instability, it was not necessary to innovate new types of unstable systems. Thus the design of the Rijke apparatus used in this investigation was based upon information gained from previous investigations. As mentioned in the Literature Review of Chapter I, the effects of geometric variables such as length and position of heater have been extensively studied. Oscillations have been observed in pipes having diameters from approximately 1.3 to 5 inches and lengths from 18 inches to 10 feet. Table 1 summarizes the pertinent dimensions from previous investigations.

Table 1 . Rijke Configuration Dimensions from Previous Investigations

Investigator	L (Inches)	D (Inches)	x_h (Inches)	L/D	x_h/L
Rayleigh (10)	60.0	4.75	*	12.6	*
Rijke (3)	31.5	1.29	7.88	24.4	0.25
Lehmann (27)	45.0	2.64	11.25	17.1	0.25
Kerwin (13)	18.0-72.0	2.00	*	9.0-32.0	0.1-0.85
Friedlander (21)	68.0 ⁺	3.00	54.4 [‡]	22.7	0.8 [‡]
Malling (20)	32.0	3.25	8.0	9.9	0.25

* Heater position variable.

+ Variable length apparatus (60.0 to 90.0 inches) but 68.0 inches was used for the majority of the testing.

‡ Variable heater position. For closed-closed end conditions, heater must be positioned in downstream location which corresponds to $x_h/L = 0.2$ for open-open end conditions.

It was decided that the Rijke apparatus would be built to Malling's dimensions, and that the heater would be of a thin, wound ribbon type similar to those used by Malling, Friedlander, and Kerwin. The following basic dimensions were selected for the Rijke apparatus of this investigation.

$$L = 31.736 \text{ inches, } D = 3.303 \text{ inches, } x_h = 7.699 \text{ inches}$$

giving,

$$x_h/L = 0.243, \quad L/D = 9.60$$

An assembly drawing of the Rijke apparatus is shown in figure 4. The assembly drawing includes a parts list and important nominal dimensions. The upstream duct was made from 3 1/2 inch diameter AISI 304 stainless steel tubing having a wall thickness of 0.100 inch. The outer diameter was machined to remove some surface imperfections until the wall thickness was 0.073 inch. The upstream duct was made from 0.049 inch thick 304 stainless steel sheet stock which was rolled and seam-welded to match the downstream duct inner diameter. Flanges were welded to the tubing and the two nearest the heater had O-ring grooves machined in them. The cold (upstream) flanges were sealed using Teflon gaskets and a commercial silicone sealant. The 1/2 inch aluminum spacer is typical of a number of them made for length adjustments as required during the test program. As shown, a circular hole matching the duct inner diameter was cut into the 3/4 inch plywood mounting board and became part of the total length.

Figure 5 is an assembly drawing of the heater. The heater ribbon was made from Inconel 600 flat stock and was 0.008 inch thick by 0.250 inch wide by 8.0 feet long. The Inconel 600 ribbon was wound

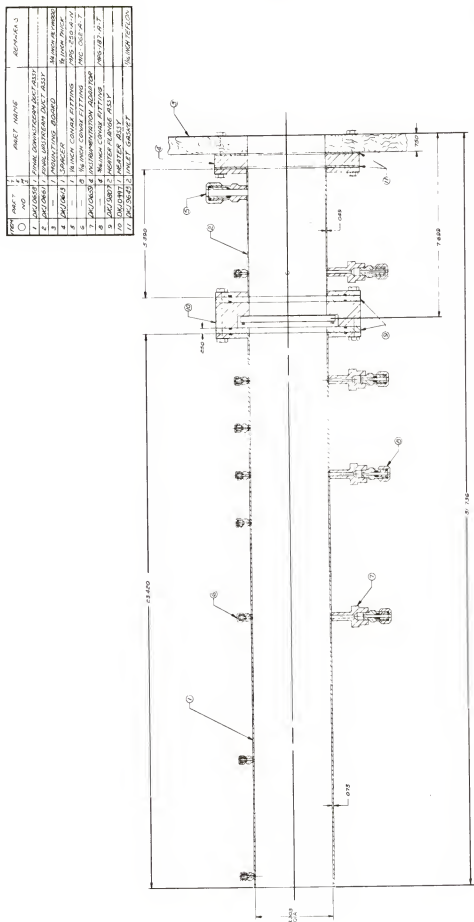


Figure 4. Rijke thermoacoustic instability rig assembly drawing.

BIOLIKE THERMODYNAMIC
INSTABILITY RING
ASSY OF

10/10/2010
 10/10/2010
 10/10/2010

5650 NMD

ITEM	PART NO	QTY	PART NAME	REMARKS
1	DACT 9162	1	HEATER SUPPORT RING TRANSISTE MAT'L	
2	DACT 9166	1	INSUL. HEATER RING INCLD 600	
3	---	24	SELF TAPPING SCREWS #6 PANHEAD, SETT	
4	DACT 9162	2	ROD-ELECTRICAL CONNECTION BERYLCO - Z5	
5	DACT 9118	2	CONAK FITTINGS	MPB-187-A-T
6	---	2	TERMINUS DEVICE ASY	

HEATER ASSEMBLY	PART NO.
ENGINEER:	W.R. KAMUSU
	DCJ-0997

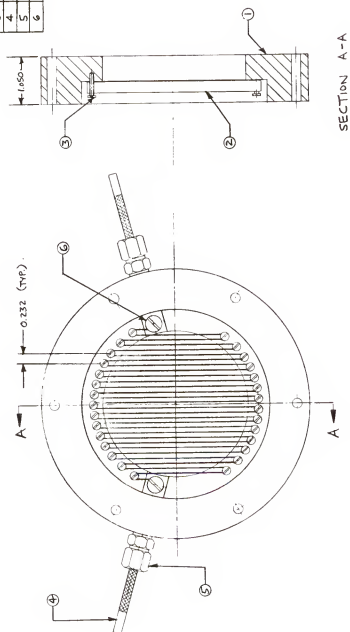


Figure 5. Heater assembly drawing.

around sheet metal screws which served as pegs and were located near the circumference of the transite ring. As shown in the assembly drawing, the heater ribbon gave the appearance of many plates arranged parallel to the flow. Electrical current was conducted to the heater ribbon through 2 Berylco-25 rods. The rods entered the transite ring through Conax 0.187 pressure gland fittings utilizing teflon packing glands. The rods were electrically insulated by coating them with a 0.004 inch thick layer of Allen P-1 cement that possessed excellent dielectric properties.

Two sets of heater hardware were fabricated; however three different ribbon materials of varying thickness were tried before the best combination was found. Keeping in mind that the electrical energy was supplied by current limited devices, the following criteria were used in selecting a heater ribbon material: (1) high electrical resistivity, (2) low thermal expansion coefficient, and (3) high temperature strength. The materials and thicknesses investigated were 0.004 inch thick Nichrome V, 0.004, 0.008, and 0.015 inch thick Inconel 600, and 0.008 and 0.015 inch thick Inconel 718. Nichrome V possessed the best electrical properties but had the highest thermal expansion coefficient as compared to the Inconels. Inconel 718 possessed the best strength and thermal expansion properties but was found to become brittle after wrapping around the pegs. Inconel 600 was finally chosen because it provided the best compromise in properties. The measured average electrical resistance for the heaters used was 2.3 ohms.

A number of fittings were provided along the length of the apparatus in order to allow the insertion of the pressure, temperature, and velocity instrumentation. The small fittings on the right-hand side were stainless steel Conax 0.062 pressure gland fittings with teflon

glands. These fittings were welded directly to the tubing and were used for insertion of the gas temperature and microphone probes. The large 0.25 inch Conax fitting near the mounting board was used for installation of a reference microphone which remained in this fixed position for most of the tests. Four adaptors were welded on the left-hand side of the apparatus which served as a base for a hot wire positioning device. The probes were inserted into the interior of the ducts through 0.187 Conax fittings which were threaded into the adaptors.

Sondhauss Configuration

The proportions for the Sondhauss configuration were those recommended by Feldman (24). For oscillations to occur, he found that L/D can vary from 8 to 50 with an optimum value of 12, while the heater should be positioned at a location one-third of the distance from the closed end ($x_h/L = 1/3$). Feldman also stated that a significant increase in the sound output of the device occurred when the tube downstream of the heater was cooled while the upstream tube was insulated. This was the reason for using the cooled hardware as previously described. Water was used as the coolant in the downstream duct while the upstream duct was vented to the atmosphere and the air layer between the tubes provided insulation to that section.

The following dimensions were used for the Sondhauss hardware of this program.

$$\begin{aligned} L &= 41.43 \text{ inches, } D = 3.303 \text{ inches, } x_h = 12.26 \text{ inches} \\ &\text{giving,} \\ L/D &= 12.5, \text{ and } x_h/L = 0.296. \end{aligned}$$

Figure 6 is an assembly drawing of the Sondhauss apparatus. The device consisted of the double walled upstream and downstream ducts, heater

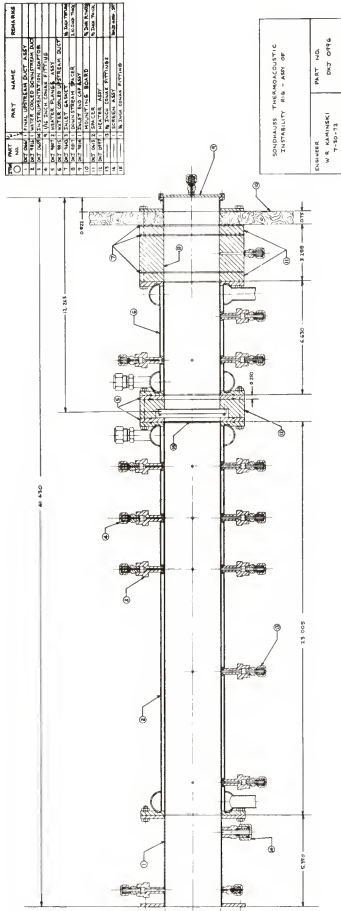


Figure 6. Sondhauss thermoacoustic instability rig assembly drawing.

assembly (same as used for the Rijke configuration), a screen, a series of spacers, the upstream duct from the Rijke configuration mounted at the top of the double walled duct, hardware for varying the inlet end condition (shown blanked off), and a plywood mounting board.

The double walled ducts, having an annular gap of 0.153 inch, were fabricated from 300 series stainless steel tubing. The inner tube was 3.375 inches in diameter by 0.035 inch thick while the outer tube was 3.750 inches in diameter by 0.035 inch thick. The ducts had instrumentation adaptors and manifolds welded on as shown in the assembly drawing. The heater assembly was the same as described for the Rijke configuration with the exception that a screen was placed 0.100 inch downstream of the heater ribbon to give the heater section a higher impedance. The screen was of a square weave, 20 x 20 mesh and made from 0.012 inch stainless steel wires.

A flanged end piece was added to the inlet of the Sondhauss device for purposes of changing the inlet area. Discs with holes of varying diameter were fastened to the end piece to allow a study of the effect of changing the inlet impedance from that corresponding to an open end (Rijke) to that of a closed end (Sondhauss) system. The assembly drawing shows a closed end disc with a 0.062 Conax fitting welded on for installation of either pressure or temperature instrumentation. Again, as for the Rijke configuration, the mounting board was a part of the total length of the device.

Instrumentation Systems

Electrical

Heating within the test apparatus was accomplished by inducing an alternating electrical current to flow through the heater strip, thereby

generating internal energy within the material by the Joulean effect. Alternating current was supplied to the heater by two General Radio Company, Type W20TM3 Variacs, connected in parallel. The Variacs were in turn connected to a well regulated; 120 volt AC, instrument electrical supply system having a power factor near unity. The desire to have 2000 watts of electrical power available to the test apparatus required that two Variacs be used. This was because the available Variacs were rated for a maximum current of 20 amps which gave 1000 watts when supplied to a 2.5 ohm resistive load. A schematic diagram of the electrical system is shown in figure 7 .

The electrical power dissipated by the heater element was measured directly using a Weston Instruments Wattmeter, Model 310 having a range of 0 to 5000 watts. The voltage across the heater was monitored by a Weston Instruments, Model 903, AC Voltmeter having a range of 0-150 volts. Voltmeter readings were primarily used for reference purposes; however they did offer a means of determining power indirectly if the wattmeter malfunctioned during a prolonged test. In that case power could be determined from measured values of voltage, room temperature resistance of the heater strip ¹, and a curve of specific resistivity versus temperature for the given material.

The operation of two Variacs in parallel required that a balanced current output be maintained between the units. Simpson AC Ammeters, 0-50 amps range, were used to monitor the current output from each Variac in order to maintain balanced operation. This was the only function of the ammeters.

¹Each heater assembly was resistance checked at room temperature using a Rubicon Instruments Wheatstone Bridge, Model 1052, having an uncertainty of measurement less than 0.116% of reading.

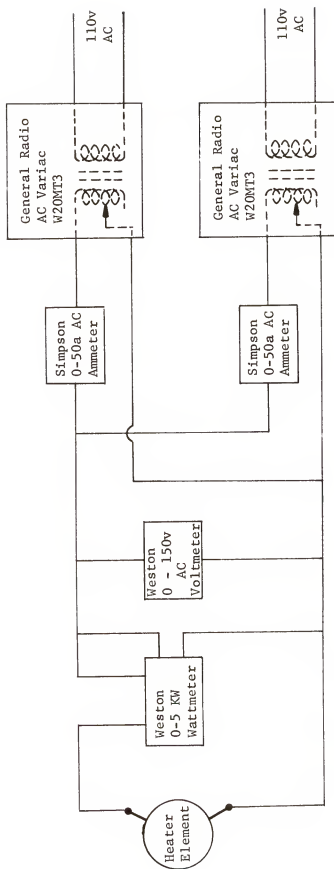


Figure 7. Schematic diagram of electrical system.

Acoustic

This research program involving acoustic phenomena required that certain acoustic parameters be measured accurately. Basically, sound pressure and frequency were measured at various locations throughout the test apparatus. Additionally, it was necessary to have equipment available to measure the frequency spectrum of the sound signal and to obtain some information on phase angle between either two sound pressure signals or between a sound pressure and particle velocity (hot-wire measurement) signal. The instrumentation used to satisfy the above requirements will be discussed in the paragraphs which follow.

Brüel and Kjaer condenser microphones were used to simultaneously measure the sound pressure and frequency. The B&K microphones were selected because of their relatively small dimensions, flat frequency response, distortion free measurement of signals in the 70 to 174 db range, excellent long term stability characteristics and insensitivity to ambient temperature variations up to 300°F. A standard sized 1/4 inch microphone was used in this study.² With reference to figure 8, the 1/4 inch microphone consists of a Type 4135 Cartridge, UA0035 1/4 to 1/2 inch adaptor and a Type 2615 Cathode Follower.

A high impedance probe tube was used with the 1/4 inch B&K microphone to allow probing of the sound field in those regions of the test apparatus having a severe thermal environment. A B&K, 1 mm probe tube DB0214 was modified to accept a 1/16 inch OD tube as shown in figure 20. The small dimensions of the tube minimized flow blockage and acoustic steaming patterns while the probe was inserted into the interior regions

² The 1/8-inch microphone was tried early in the test program but due to its fragility was subsequently abandoned in favor of the 1/4 inch microphone.



Figure 8. Brüel and Kjaer 1/4 and 1/8 inch condenser microphone assemblies.

of the apparatus. It was necessary to insert tufts of steel wool into the probe tube to obtain the best possible frequency response. Calibration and damping of the probe tube will be discussed in the next chapter.

Figure 9 shows a schematic representation of the sound measuring system. Three basic signal paths are apparent. The first originates at probe microphone 1 which was used to probe the sound field at various locations within the test apparatus. The microphone supplies an electrical signal which is proportional to the sound pressure level. A B&K Microphone Power Supply, Type 2801 provides the polarization voltage to the microphone and contains an attenuator for standardization and an emitter follower for isolation. The General Radio Wave Analyzer, Type 1900A was used to measure the output of microphone 1.

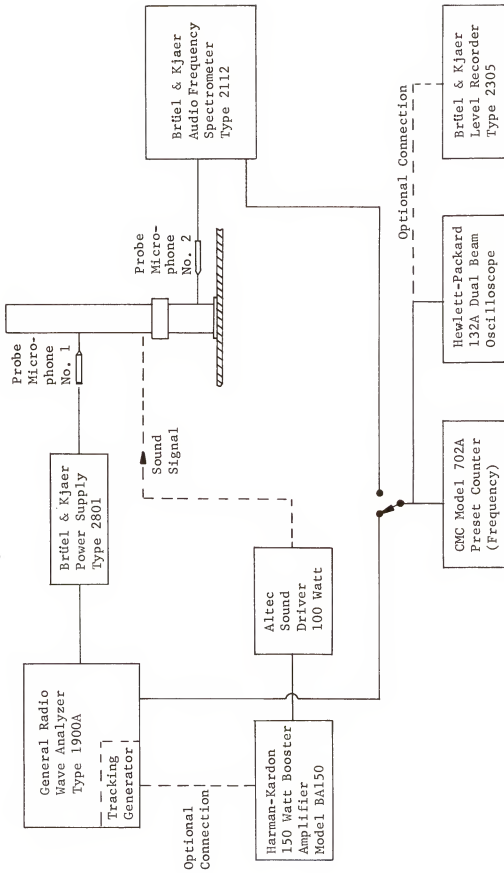


Figure 9. Schematic drawing of sound measuring system.

This analyzer was particularly well suited to the analysis of complex sound signals in the 20 to 54,000 Hz range. The sound signal, after being electronically processed in the analyzer, passes through a highly selective quartz crystal filter whose bandwidth could be set to either 3, 10, or 50 Hz for accurate frequency analysis.

The second signal path originates at probe microphone 2 which was fixed at a single location and used for reference purposes.³ Microphone 2 was connected to a B&K Audio Frequency Spectrometer Type 2112 for analysis of the sound signal. This analyzer contains an internal microphone power supply and is capable of frequency analysis. However, because it has broader band filters (1/3 or 1/1 octave) than the GR1900A, it was not as well suited for the intended work.

The signals from either the GR1900A or the B&K 2112 were fed through a selector switch to a parallel arrangement of a frequency counter, oscilloscope and optionally through a level recorder. A CMC Model 702A Preset Counter was used to measure the frequency of the sound signal. The Hewlett-Packard 132A Dual Beam Oscilloscope was used to monitor the microphone outputs for approximate level, phase angle, and distortion. The B&K Level Recorder Type 2305 was used to continuously record the wave analyzer output signals and had an especially useful feature of having paper speeds as low as 0.1 mm/sec. This feature was important for long duration tests. The level recorder can accurately record signals in the 10 to 200,000 Hz range by internal circuitry which converts fluctuating voltages to equivalent DC voltage levels.

³ During initial testing, the output of microphone 2 was recorded on the B&K level recorder and continuous monitoring of test conditions was accomplished via this parameter.

During certain portions of the test program, it was necessary to supply the test apparatus with a pure sound signal of known frequency and power level. The sound signal was generated by an Altec Sound Driver which is shown in the schematic as an optional connection and forms the third signal path. The Altec Sound Driver is capable of generating 150 db at its outlet connection but because of the piping arrangement used, the signal at the test rig was attenuated to 135 db. The Altec Sound Driver was driven by the tracking generator portion of the GR1900A Wave Analyzer which provided a pure 1 volt, sine wave signal whose frequency was continuously adjustable from 0 to 54,000 Hz. A Harman-Kardon Model BA150 amplifier boosted the voltage signal before being fed into the Altec Sound Driver which converted the electrical signal into a pressure or sound signal. Although not shown in the schematic, the frequency output from the tracking generator was monitored on the CMC Preset Counter.

Temperature

Two types of temperature measurements were made during the experiments. Gas stream temperatures were measured using miniature thermocouple probes while the heater surface temperature was measured using an infrared radiation thermometer. Figure 10 shows a schematic representation of the temperature measuring systems.

Figure 11 is an assembly drawing of a shielded gas temperature probe. There were two reasons for using the small tube diameters shown. The first being to minimize interference with the acoustic field in the apparatus and the second to allow entry of the probe through the heater flanges thereby permitting gas temperature measurements to be made within 0.6 inch to either side of the heater. A bare chromel-

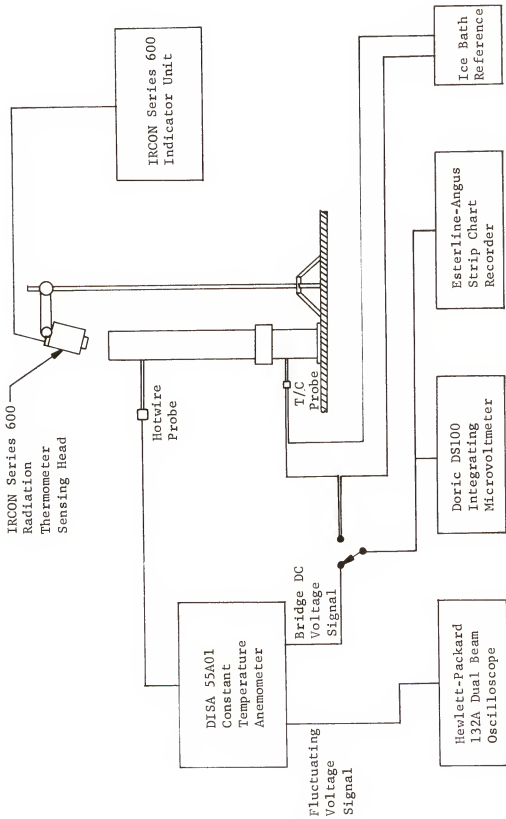
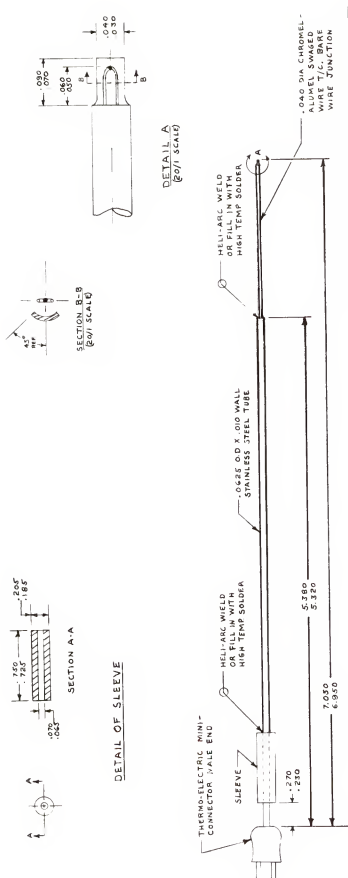


Figure 10. Schematic diagram of temperature and velocity measuring systems.



SHIELDED GAS TEMPERATURE PROBE ASSEMBLY	
ENGINEER: W. R. KAMINSKI 7/20/72	PART NO. DKJ-9806

Figure 11. Shielded gas temperature probe assembly drawing.

alumel thermocouple junction was formed from 0.002 inch wires encased in a 0.040 inch diameter swaged rod having ceramic insulation and a stainless steel sheath. Radiation shielding of the thermocouple junction from the heater surface was provided by extending one-half of the stainless steel sheath over the junction. The probe was always oriented so that the shield was facing the heater thereby eliminating an erroneous heat input to the junction.⁴ The thermocouple probes were positioned manually in the gas stream using an accurate scale (smallest division 1/64 inch) and a knife edge which was clamped to the sleeve of the probe.

The remainder of the thermocouple circuit included an ice bath reference junction and readout devices. Two types of readout devices were used, a Doric DS100 Integrating Microvoltmeter and an Esterline-Angus Strip Chart Recorder. The Doric microvoltmeter had a 1 microvolt resolution while the strip chart recorder had a 10 microvolt resolution. It was necessary to have at least 10 microvolt resolution in order to sense small temperature changes at temperature levels from ambient (70°F) upward.

Before an infrared radiation thermometer was used to measure heater surface temperatures, thermocouples were used, but proved to be unsatisfactory due to the numerous problems that were encountered. The major reasons for rejecting thermocouples for this measurement were: (1) difficulty in attaching the small thermocouple wires (.002 inch diameter wires in a .020 inch diameter insulated sheath) to the thin heater strip (.004 to .008 inches thick), (2) failure of junctions resulting from successive thermal expansions, (3) shorting out of the thermo-

⁴ Testing has shown that in certain locations within the apparatus, errors as large as 60°F could be incurred if the radiation shield did not block the view of the heater from the junction.

couple wires against the heater strips, (4) high cost and most importantly (5) an adequate description of the heater temperature distribution was never possible with only 4 or 5 thermocouples. Because an infrared radiation thermometer can be remotely located, as long as it has the heater surface in its "line of sight," the solution to the above problems is obvious. However, one must pay a price for solving these problems so readily, that being in terms of a rather difficult calibration procedure. Fortunately, it only had to be made once.

The IRCON Infrared Radiation Thermometer, Series 600, Model 647 consists of a Sensing Head and Indicator Unit which are interconnected by a special cable. In the Sensing Head radiation emitted by the object being viewed is focused by a lens, through a filter and modulator, onto a lead sulfide detector where it is converted into an electrical signal at the modulation frequency. The optics are so arranged that the visible image on a circular reticle (defines target area) is in focus to the eye when the infrared image is in focus on the infrared detector. The signal from the detector is amplified by a solid state preamplifier in the Sensing Head providing a high level signal from a low impedance source. The signal is further amplified in the Indicator Unit and synchronously demodulated. The output of the demodulator is fed through a filter and precision voltage divider to a panel meter. The panel meter is arranged into three range scales: 800 to 1400°F, 1000 to 2000°F and 1400 to 3000°F.

Velocity

The study of thermoacoustic instability would not be complete without a knowledge of the time mean and fluctuating velocities within the apparatus. Hot-wire anemometry was used to measure these velocity

fields. The principles of hot-wire anemometry will not be discussed here because it has become a well-established practice during the past few years and a wealth of information is available in the open literature.⁵

The elements of the hot-wire anemometry system are shown schematically in figure 10. Two types of DISA Electronics hot-wire probes were used in the experimental program, a 55F33 Miniature Probe and a 55A75 High-Temperature Probe. Figure 12 shows both probes for comparison. The 55F33 probe has its sensor parallel to the probe axis which makes the probe well suited to pipe flow applications since the sensor is aligned at a right angle to the flow. The sensors of these miniature hot-wire probes are made from platinum plated, tungsten wires, 1.25 millimeters long by 5.0 microns in diameter. These probes were found to be satisfactory but were limited to 300°F environmental temperatures. Since gas stream temperatures of 1000°F were anticipated in the vicinity of the heater, the 55A75 probe was selected because of its high temperature capability of 1400°F. The sensor of this probe is a 2.2 millimeter long by 10 microns in diameter, platinum-rhodium wire.

The voltage signal from the hot-wire probe was fed into a DISA 55A01 Constant Temperature Anemometer. Basically, the CTA performs two main functions; the first is to minimize the effect of the thermal lag of the sensor which increases the upper limiting frequency by approximately one hundred and the second is to keep the probe resistance very nearly constant. Fundamentally, the CTA measured the amount of

⁵ DISA Electronics, Franklin Lakes, New Jersey publishes a number of excellent manuals and information booklets on the subject of hot-wire and hot-film anemometry.

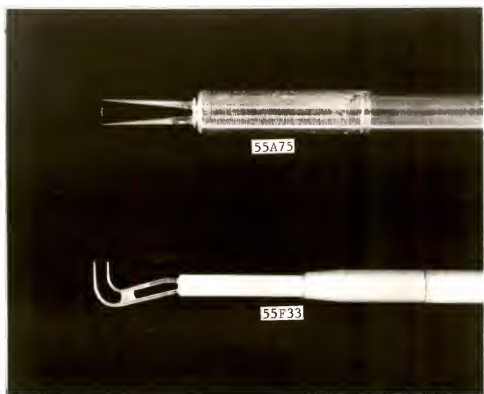


Figure 12. Hot-wire probes used in experimental program.

power required to keep the sensor temperature constant. Two panel meters are provided, one displays the bridge AC voltage (RMS) while the other bridge DC voltage. The readouts correspond to the fluctuating and time mean velocities respectively.

The fluctuating velocity signal can be read with sufficient accuracy on the panel meter but good practice dictates that the time mean signal be read on a precision voltmeter. As shown in figure 10, the bridge DC voltage was fed through a selector switch to the Doric DS100 Integrating Microvoltmeter and/or Esterline-Angus Strip Chart Recorder. The fluctuating signal was displayed on a Hewlett-Packard Dual Beam Oscilloscope for visual study and photographic recording.

Figure 13 shows the hot-wire probe positioning device that was used. The probe shaft was inserted through a 1/8-inch Conax fitting

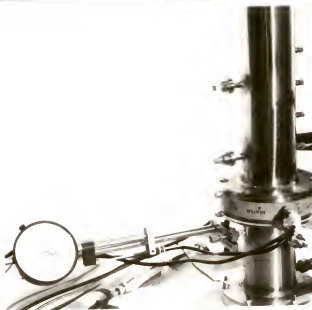


Figure 13. Hot-wire probe positioning device employing a dial indicator to measure probe position.

containing a Teflon packing gland. The fitting was threaded into an adaptor which also served as a base for mounting the positioning device. The probe was manually set to a desired immersion depth and locked in place while the probe sensor position was read on a Starret 5 inch stroke, dial indicator. The smallest division on the dial indicator was 0.0001 inch and a calibration showed that the probe sensor could be positioned to within ± 0.001 inch.

CHAPTER III
THE EXPERIMENT
Introduction

This chapter describes the experimental aspects of a research program devoted to a study of thermoacoustic instability. It was felt that by studying the simplest of thermoacoustically unstable systems, the Rijke and Sondhauss devices using air as the fluid and an electrical heater as the thermal energy source, a basic understanding could be achieved and perhaps applied to more complex systems. In order to perform the necessary experiments, a versatile apparatus was constructed which allowed both Rijke and Sondhauss instability to be investigated using the same basic hardware. Figures 14 and 15 show the Rijke and Sondhauss test apparatus and associated instrumentation in position for testing.

Testing was conducted in the control room of the B-21 test stand at Pratt and Whitney's Florida Research and Development Center. The site was ideally suited for the test work because the room was clean, air conditioned, had a well regulated electrical power supply and most importantly possessed constant acoustical background conditions.

Experiments were focused on making both time mean and fluctuating measurements of temperature, pressure and velocity throughout the Rijke apparatus and especially in the "near field" of the heat source where both theory and data were lacking. The effects of parameters such as heater power level, inlet area and inlet velocity were explored. Another

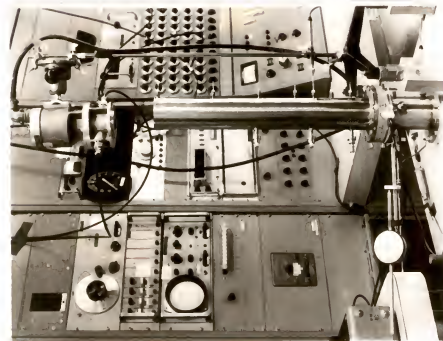


Figure 14. Rijke configuration test apparatus and associated instrumentation in position for testing.

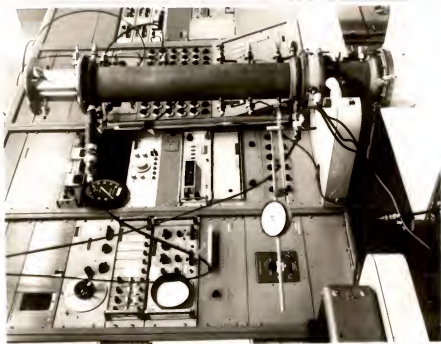


Figure 15. Sondhauss configuration test apparatus in position for testing.

goal was to experimentally investigate the relationships existing between Rijke and Sondhauss modes of instability.

All of the measurements that were originally contemplated were successfully executed with the exception of measuring fluctuating temperatures. Preliminary investigation of practical methods which could be used for this measurement were narrowed down to the use of a subminiature hot-wire probe operated in a constant current mode or a high response thermocouple system. The subminiature hot-wire probe could not be used because a constant current anemometer was not available to the program. The high response thermocouple system requires the use of a probe with a junction made from 0.0005 inch diameter wires and special electronic equipment to amplify, filter and reduce the thermal lag of the thermocouple signal. Consultation with a person (28) well versed in these measurements indicated that the electronic noise would be greater than the fluctuating temperature signals and would require a major development program to perfect. For these reasons, the measurement of fluctuating temperature was abandoned.

Experimental Program

Test Summary

The experimental program consisted of a series of 23 tests, 19 devoted to the Rijke configuration and 4 to the Sondhauss configuration. Table 2 presents a test summary for the Rijke configuration. Four categories are shown to differentiate the Rijke tests. Each test has been assigned a test number, although not in chronological order, which will be used for identification purposes in this report. This table summarizes the input electrical power range, types of measurements made and a brief statement of the purpose of each test. Under the measure-

Table 2. Rijke Configuration Test Summary

Test Type	Test Number	Heater Electrical Power (Watts)	Measurements			Purpose
			Acoustic	Gas Stream Temperature	Heater Surface Temperature	
A. Basic Test Series	1	1000	Complete	Complete	Complete	Describe acoustic and temperature fields within device with emphasis on "near field" of heat source. Measure velocity profile upstream of heater.
	2	1200	Complete	Complete	Complete	
	3	1400	Complete	Complete	Complete	
	4	1600	Complete	Complete	Complete	
B. Velocity Study	5	1200	Maximum			Describe steady and fluctuating velocity fields within device.
C. Controlled Inlet Flow Tests	6	1000	Maximum			Determine the flow conditions which maximize the sound pressure level.
	7	1200	Maximum	Maximum		Checkout performance of heaters.
	8	1400	Maximum	Maximum		
D. Miscellaneous Tests	9	100-1600				Room sound survey.
	10	1000-1200	Partial			Determine limits of instability.
	11	0-1600	Maximum			Complement acoustic data taken in Basic Test Series.
	12	900	Complete			Repeatability of measurements.
	13	1000	Partial			Repeatability of measurements.
	14	1200	Complete	Partial	Partial	Repeatability of measurements.
	15	1600	Complete	Partial		Repeatability of measurements.
	16	800-1400	Maximum			Determine effects of cooling on sound pressure level.
	17	1200	Maximum			Frequency spectrum of sound signal.
	18	0	Maximum			Frequency response testing to determine fundamental and harmonic frequencies and effective length of system.
	19	1100	Maximum			No heating. Sound driver used.

Attempt to drive system to oscillate at other than fundamental frequency using Altec sound driver.

ments column, the term "complete" means that the given parameter was measured at all possible locations, "partial" means that only some locations were sampled while "maximum" refers to sampling at a given location which yields a maximum value of that parameter.

Table 3 presents a similar test summary for the Sondhauss configuration.

Table 3. Sondhauss Configuration Test Summary

Test Type	Test Number	Heater Electrical Power (Watts)	Measurements			Velocity	Purpose
			Acoustic	Gas Stream Temperature	Heater Surface Temperature		
A. Basic Test Series	20	700	Complete	Complete	Partial		Describe acoustic and temperature fields within device with emphasis on "near field" of heat source.
B. Velocity Study	21	700	Maximum			Complete	Describe steady and fluctuating velocity fields within device.
C. Miscellaneous Tests	22	0-1000	Maximum		Maximum		Determine limits of instability with and without a screen 0.100 inches downstream of heater.
	23	900	Maximum		Maximum		Vary inlet area (continuously) from closed (Sondhauss) to fully open (Rijke) to determine if mode of oscillation is continuous or not.

Description of Tests

Before discussing the details of the test program, a synopsis is in order. The majority of the tests were conducted using the Rijke test apparatus of fixed length and diameter. The main independent variables were heater electrical power, inlet area and inlet velocity resulting from the addition of an externally supplied flow. Initial testing defined the range of heater electrical power over which the Rijke device was unstable. Next, a range of heater power was selected (1000, 1200, 1400, and 1600 watts) over which basic measurements could be made. Additional tests were then conducted in order to examine other interesting properties of the Rijke mode of instability.

In order to facilitate the discussion which follows, sketches of

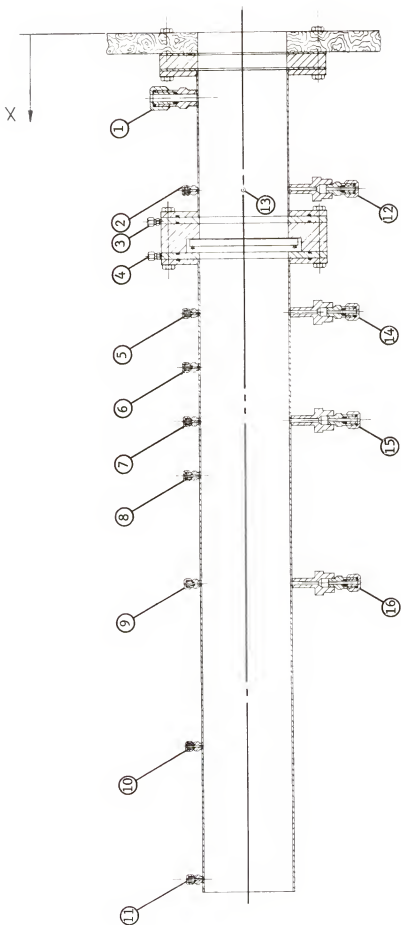
both test configurations are presented in order to identify instrumentation fittings and locations relative to the inlet plane. Figures 15 and 17 give these fittings or hole locations for the Rijke and Sondhauss configurations, respectively.

Rijke tests

The objective of the Basic Test Series was to obtain a sufficient amount of data to describe the temperature and acoustic fields within the test apparatus with emphasis on the "near field" of the heater. The apparatus was set up as shown in Figure 14 and tests were performed at 1000, 1200, 1400 and 1600 watts of input electrical power. A microphone probe was used to measure the average sound pressure across the duct at various positions along the device. Time mean gas stream temperatures were measured at 11 points in the diametral plane of the duct for various lengthwise positions. Fittings 1 through 11¹ were used for both the microphone and thermocouple probes. Heater surface temperatures were measured at 41 points using an infrared radiation thermometer. Velocity measurements, using a DISA 55F33 hot-wire probe, were made at 18 locations in two mutually perpendicular planes just upstream of the heater. Fittings 12 and 13 were used for this purpose. The resulting steady velocity and gas stream temperature profiles were used to compute the mass flow rate of air flowing through the device.

The purpose of the Velocity Study was to describe the time mean and fluctuating velocity fields within the device. During test 5, velocity measurements were made by probing through fittings 14, 15, 16 and just above the exit plane of the device using a DISA 55A75 hot-wire probe.

¹ Gas stream temperature measurements were also made by probing through fitting 13 to complement velocity measurements taken at this location.



Fitting Number	X (Inches)	Fitting Number	X (Inches)	Fitting Number	X (Inches)
1	2.312	7	14.316	13	5.452
2	5.452	8	16.316	14	10.316
3	6.889	9	20.316	15	14.316
4	8.316	10	25.316	16	20.265
5	10.316	11	31.236		
6	12.316	12	5.452		

Figure 16. Location of probe fittings on Rijke test apparatus.

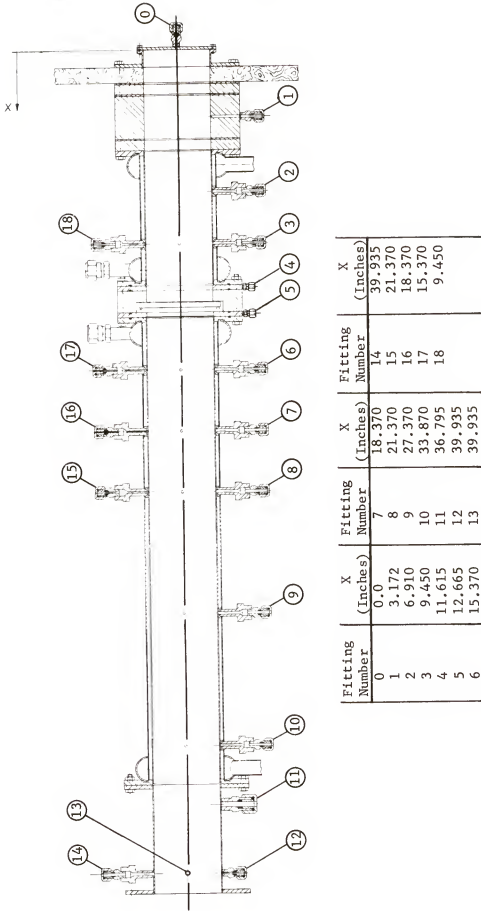


Figure 17. Location of probe fittings on Sondhauss test apparatus.

A DISA 55F33 hot-wire probe was used to measure the velocity in the plane of fitting 12. A microphone probe was positioned at approximately mid-length (fitting 7) to continuously monitor the maximum sound pressure and frequency. This insures that data from test 5 could be used in conjunction with the data from test 2 of the Basic Test Series. More will be said about insuring constant test conditions later in the chapter.

The effect of varying the mass flow rate through the Rijke device was investigated in the Controlled Inlet Flow Test Series. The objective of this test series was to determine the inlet flow conditions which maximize the sound pressure level in the device. Two means were used to vary the flow rate through the device. The first method consisted of using a fan to supply additional flow to the system, thereby augmenting the flow resulting from the natural convective currents. The second method consisted of restricting the flow induced by the natural convective currents without changing the inlet acoustic characteristics.

As shown in figure 18, an inlet plenum chamber was constructed from thin plastic sheet material which was loosely hung below the mounting table. The plenum chamber was effectively a large plastic bag having a volume of 26 cu. ft. and free to expand and contract in such a manner that the acoustic coupling between the Rijke device and the surroundings did not change appreciably.² Air flow was supplied by 2 Kintel, 100 CFM instrument cooling fans. Flow control was achieved by controlling the fan motor speed and/or throttling the fan inlet. Maximum sound pressure (fitting 7) and inlet centerline velocity (fitting 12) were continuously monitored for tests 6, 7 and 8. The maximum heater

²Tests have been conducted which confirm this statement and are discussed in the next chapter.

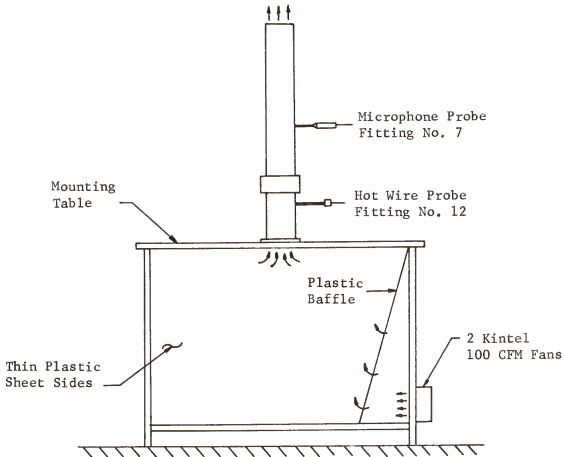


Figure 18. Test setup for controlled inlet flow tests.

surface temperature was measured for tests 7 and 8.

The Miscellaneous Tests category contains 11 tests which were performed to either support the other test categories or to investigate certain interesting aspects of the Rijke mode of thermoacoustic instability. A general description of the tests can be obtained from the brief statements appearing under the heading "Purpose" in Table 2. Most of the descriptions are self-explanatory. However, the following remarks provide additional clarification.

In test 10, room sound measurements were made in order to determine the type of ear protection required. Maximum A-weighted sound pressure level readings were measured to be 100 db at ear level in the vicinity of the hot-wire anemometer. Ear defenders were found to give adequate

protection against the sound pressure levels encountered.

A complete set of acoustic measurements were taken for 900 watts of heater power as indicated for test 12. A single measurement of inlet centerline velocity (fitting 12) was also made for reference purposes. The objective of this test was to obtain acoustic data for a power level near the lower limit of instability. The 900 watt heater power level was the lowest power level at which the Rijke device would remain in an oscillatory condition for an extended period of time.

Test 16 was conducted to determine the effect of cooling on the sound pressure level. This test was the only occasion that the water cooled hardware was used in the Rijke test series. In the first part of the test, just the downstream duct was replaced by the cooled duct while in the second part of the test just the upstream duct was replaced. The maximum sound pressure level was measured for a heater power range of 800 to 1400 watts. The test was then repeated using water cooling.

During test 17, the GR 1900A Wave Analyzer was used to measure the frequency spectrum of the sound signal produced while the test apparatus was operating with 1200 watts of heater power. The wave analyzer was set up for a 3 Hz frequency band as the tracking generator was swept from 0 to 1000 Hz. The resulting sound pressure level at location 7 was recorded. During tests 18 and 19, an external sound signal was supplied to the test apparatus using an Altec sound driver. In test 18 a sound signal of varying frequency was used to determine the fundamental and harmonic frequencies and the effective length of the Rijke device. Heating was not applied. During test 19, with the heater power set at 1100 watts, an attempt was made to drive the system to oscillate at frequencies other than the fundamental frequency. The Altec sound driver provided a signal of varying intensity and frequency. A micro-

phone probe was installed at fitting 7 to monitor the sound pressure level.

Sondhauss tests

The objectives of the Basic Test Series and the Velocity Study were identical to those of the complementary Rijke tests, that is, to describe the acoustic, temperature and velocity fields within the Sondhauss device. However, the tests were less extensive since only one heater power level (700 watts) was investigated. Figure 15 shows the Sondhauss apparatus in position for testing. In test 20, a maximum number of acoustic and gas temperature measurements were made (fittings 0 through 12). Velocity measurements were made in test 21 by probing through fittings 13, 14 and 15 using the DISA 55F33 hot-wire probe while the DISA 55A75 probe was used at fitting 17.

In the Miscellaneous Test category, two interesting tests were performed. The limits of instability were determined in test 22. A microphone probe was located at the closed end which gave the maximum sound pressure in the device and the infrared radiation thermometer was focused on a hot spot region of the heater while the power was varied. Tests were performed with and without a 20 x 20 mesh screen located 0.100 in. downstream of the heater.

In test 23, the inlet area was varied from fully closed, corresponding to the Sondhauss configuration, to completely open, corresponding to the Rijke configuration. This was done in an attempt to determine if the mode of oscillation was continuous or not. This experiment was conducted at a heater power of 900 watts which allowed both Sondhauss and Rijke modes of instability to be observed in the same apparatus. Maximum sound pressure and heater surface temperature measurements were made.

Measurements

In Chapter II the various components comprising the electrical, acoustic, temperature and velocity instrumentation systems were described. This section focuses upon the measurements themselves. Each of the measurements is discussed in terms of application, theory where necessary, calibration and accuracy.

Electrical

The electrical measurements that were made were straightforward and only involved the use of a wattmeter and a voltmeter. Both the wattmeter and a voltmeter were calibrated in the P&WA instrumentation laboratory to establish calibration practice for all instruments. All instruments are calibrated at specified intervals, normally every 3 months, to insure that they conform to P&WA specifications. All calibrations are traceable to the NBS. Instruments that fail to conform to established standards are rejected and repaired if possible. Thus, accuracies for each instrument can be quoted as those of the manufacturer or P&WA standards.

The estimated uncertainty in measuring the electrical power and voltage can be obtained from bias and precision errors assigned to each instrument. From data given in Table B-1 and use of equation [A-3] of the Appendix, the estimated uncertainty in the wattmeter reading is ± 17.5 watts while that for the voltmeter is ± 1.65 volts, where the uncertainties apply over the entire scale of both instruments.

Acoustic

Of all the acoustic equipment used, only the wave analyzers and microphone probes required special calibration. All of the other equipment was routinely checked and calibrated as mentioned above. Both the GR 1900A and B&K 2112 Wave Analyzers required a daily pre-run calibration or adjustment to insure that they would perform to the manufacturers'

specifications. The procedures are well documented in the instrument instruction manuals and will not be repeated here.

The condenser microphone cartridge is the key element in the microphone probe. It consists of a thin metallic diaphragm mounted in close proximity of a rigid back plate. Diaphragm and back plate are electrically insulated from each other and constitute the electrodes of a capacitor as shown in figure 19. The housing and insulator form with the diaphragm a closed chamber, which is only in communication with a slowly varying ambient pressure. When the microphone is exposed to a sound pressure, the diaphragm is submitted to an alternating force proportional to the pressure and the diaphragm area. The consequent movement of the diaphragm varies the capacity, and these variations are transduced into an AC voltage component if a constant charge is present between the electrodes. The charge is obtained by means of a stabilized DC polarization voltage, and it remains constant as long as the charging time constant of the circuit is much longer than the period of the sound pressure variations. By careful design, it is possible to maintain the proportionality of the AC output voltage to the sound pressure within a wide frequency range.

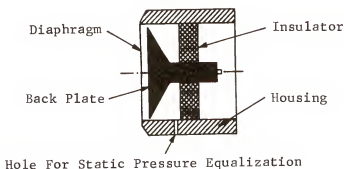


Figure 19. Schematic construction of a condenser microphone cartridge.

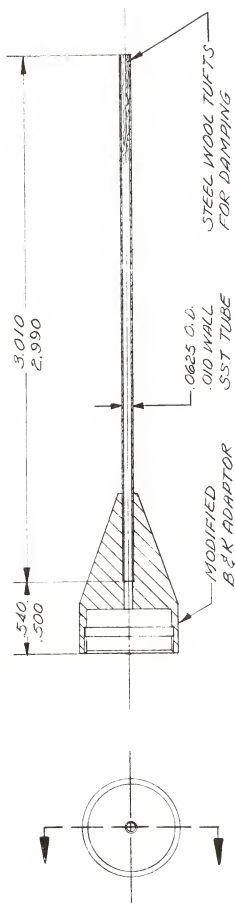
The 1/4-inch B&K microphone cartridge has a sensitivity of $0.2 \text{ mV}/\mu\text{bar}$ and has a free-field frequency characteristic which is flat up to 100 k Hz and a dynamic range going up to 174 db. Microphone cartridges are sensitive to temperature, humidity, mechanical vibration, ambient pressure changes and magnetic fields. By carefully selecting the test site, problems involving magnetic fields and humidity were eliminated. Problems associated with mechanical vibration and temperature were eliminated by design. Ambient pressure changes were recorded for each run and corrections to the microphone calibrations were made.

In order to probe those regions of the test apparatus having a severe thermal environment, a high impedance tube was used with the 1/4-inch B&K microphone. A B&K 1 mm probe tube DB 0241 was modified to accept a 1/16-inch tube as shown in figure 20. Steel wool tufts were inserted into the end of the tube for damping purposes in order to obtain a flat frequency response over the frequency range of interest.

Calibration

Two types of calibration were necessary; the first involved using a standard sound source to measure the microphone sensitivity and the other to measure the change in sensitivity with frequency due to the presence of the high impedance probe tube.

The use of a standard sound source allowed the entire microphone system to be calibrated at once, thus minimizing the uncertainty of the measurement. A B&K Pistonphone, Type 4220 was used as the sound source, having a sound pressure level of 124.1 db at 242 Hz with a known error of less than ± 0.2 db. Using the GR-1900A Wave Analyzer and pistonphone, probe microphone number 1 had a sensitivity of -27.9 db while number 2 had a sensitivity of -28.0 db re 1 volt/ μbar . Sensitivity calibrations were made daily during testing to insure that the measurements were of



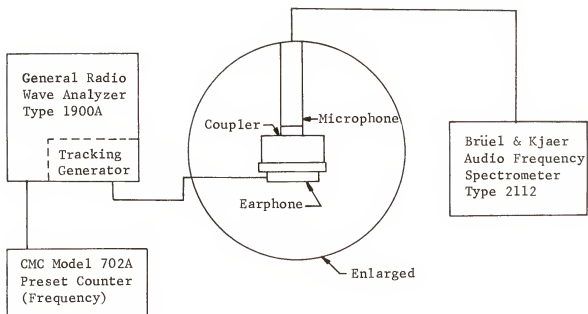
MICROPHONE PROBE EXTENSION TUBE ASSEMBLY	
ENGINEER: W. R. KAMINSKI 7/20/72	PART NO. GKJ 1152

Figure 20. Microphone probe extension tube assembly.

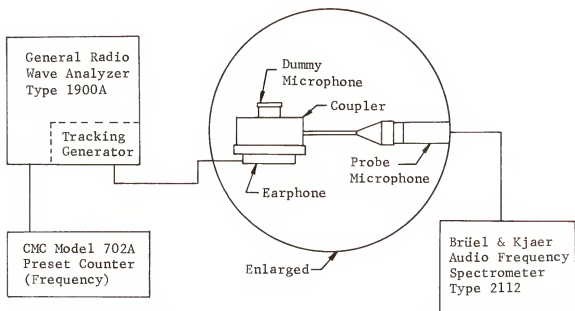
the highest quality possible.

Calibration of the probe tube consisted of the determination, at all frequencies of interest, of the change in microphone sensitivity due to the introduction of the probe tube, that is to say the frequency response of the probe tube. Accurate determination of this frequency response was obtained using the closed coupler technique. Initially, a microphone without a probe tube was inserted into a B&K 2 cc coupler, with an earphone serving as the sound source. See figure 21a. The earphone was driven by the GR-1900A tracking generator with a 1 volt signal over a frequency range from 70 to 1000 Hz. The microphone output was read directly in db from the panel meter of the B&K Audio-Frequency Spectrometer.³ Next a dummy microphone was inserted into the coupler along with an undamped probe microphone as shown in figure 21b. The earphone was driven over exactly the same frequency range as before, but now the probe microphone values include the influence of the probe tube. Taking the difference between the probe microphone and the reference microphone gives the change in sensitivity due to the presence of the probe tube. Initially the response curve was shown to undulate over a very wide frequency range. Damping the probe tube by means of fine steel wool tufts inserted at the open end of the tube allowed the tube to be "tuned" over a desired frequency range. The process was one of trial-and-error, and required four attempts before the desired frequency response was obtained as shown in figure 22. The probe microphone was damped to give an approximately zero change in sensitivity from 200 to 250 Hz.

³The B&K Audio-Frequency Spectrometer, Type 2112 has provisions for adjusting to a given microphone sensitivity.



a. Measuring response of microphone using earphone and coupler.



b. Measuring response of probe tube plus microphone using earphone and coupler.

Figure 21. Arrangement for the calibration of a probe tube.

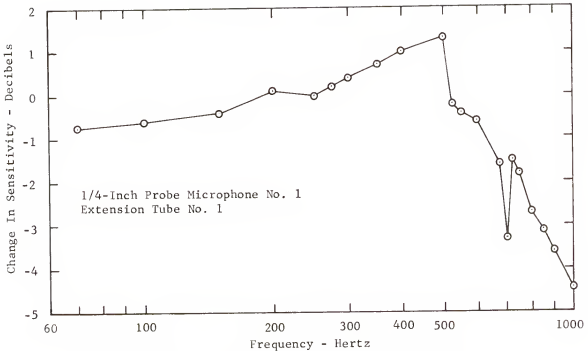


Figure 22. Microphone sensitivity change due to damping of probe extension tube.

Ambient pressure corrections for the microphone probe were obtained using a special B&K barometer, calibrated in decibels, with readings taken at the beginning and end of a given test day. The GR-1900A Wave Analyzer was used in the measurement of all sound pressures during the test program. The sound pressure signals were read in millivolts on the wave analyzer meter and the corresponding, corrected sound pressure level values given in db, were calculated using equation [9].

$$SPL = 124.1 - S_m + 20 \log_{10} SPV + \Delta_f + \Delta_{amb} \quad [9]$$

In equation [9], SPL is the sound pressure level in db re 0.0002μ bars, SPV is the sound pressure signal in volts, S_m is the sensitivity in db re 1 volt/ μ bar, Δ_{amb} is the ambient pressure correction and Δ_f is the change in microphone sensitivity due to the response of the probe tube as given in figure 22.

Measurement uncertainty

An estimate of the uncertainty in measuring sound pressure and frequency is presented in this section. Using equations [B-1], [B-2] and [B-3] as developed in Appendix B, the uncertainty in measuring sound pressure at 900, 1200 and 1600 watts for the Rijke configuration and 200, 500 and 900 watts for the Sondhauss configuration is summarized in Tables 4 and 5 below. The nominal values used were those corresponding to the maximum sound pressure measurements made at fitting 7 for the Rijke configuration and fitting 0 for the Sondhauss configuration.

Table 4. Summary of Measurement Uncertainty Calculations for Rijke Configuration Tests

Parameter and Units	900 Watts			1200 Watts			1600 Watts		
	Nominal	Bias Error B	Precision Error σ	Nominal	Bias Error B	Precision Error σ	Nominal	Bias Error B	Precision Error σ
FREQ, Hz	218.2	0	± 0.033	222.1	0	± 0.033	229.8	0	± 0.033
S_m , db	-27.9	± 0.1	± 0.05	-27.9	± 0.1	± 0.05	-27.9	± 0.1	± 0.05
SPV, volts	0.560	± 0.011	± 0.01	0.83	± 0.017	± 0.01	0.890	± 0.018	± 0.01
Δ_f , db	0.06	0	± 0.103	0.05	0	± 0.103	0.03	0	± 0.103
Δ_{amb} , db	0.0	0	± 0.025	0.7	0	± 0.025	0.0	0	± 0.025
SPL, db	147.12	± 0.200	± 0.194	151.23	± 0.200	± 0.157	151.12	± 0.200	± 0.152
Uncertainty		± 0.589 db			± 0.515 db			± 0.505 db	

Table 5. Summary of Measurement Uncertainty Calculations for Sondhauss Configuration Tests

Parameter and Units	200 Watts			500 Watts			900 Watts		
	Nominal	Bias Error B	Precision Error σ	Nominal	Bias Error B	Precision Error σ	Nominal	Bias Error B	Precision Error σ
FREQ, Hz	79.6	0	± 0.033	80.4	0	± 0.033	81.3	0	± 0.033
S_m , db	-27.9	± 0.1	± 0.05	-27.9	± 0.1	± 0.05	-27.9	± 0.1	± 0.05
SPV, volts	0.095	± 0.0019	± 0.003	0.155	± 0.0031	± 0.003	0.210	± 0.0042	± 0.003
Δ_f , db	-0.68	0	± 0.103	-0.67	0	± 0.103	-0.66	0	± 0.103
Δ_{amb} , db	0.0	0	± 0.025	0.0	0	± 0.025	0.0	0	± 0.025
SPL, db	130.98	± 0.200	± 0.298	135.23	± 0.200	± 0.205	137.86	± 0.200	± 0.171
Uncertainty		± 0.796 db			± 0.610 db			± 0.542 db	

Gas Temperature

The principles of thermocouple thermometry are well understood. This section discusses the errors involved in making gas temperature measurements. Estimates of gas temperature measurement uncertainty for the test program are stated.

Principle sources of error in gas stream measurements are non-homogeneity of the wires, conduction and radiation heat transfer to or from the junction, velocity recovery error, time lag, connectors, extension wires, reference junction errors and readout device. With reference to figure 10, the analysis which follows considers only the Doric Integrating Microvoltmeter as the readout device since the Esterline-Angus strip chart recorder was only used for diagnostic purposes. Since time mean gas stream temperature measurements were sought, time lag of the thermocouple junction need not be considered. Due to the extremely low velocities (less than 12 ft/sec) associated with the modes of thermoacoustic instability investigated, velocity recovery errors were considered negligible. By design and previous experience, junction conduction losses were also considered negligible. This statement can be somewhat substantiated by considering the miniature size of the junction region; .002 inch thermocouple wires exposed for a length of .060 inch. As far as radiation errors are concerned, a shield was designed to block the flux of radiant energy from the heater region thus minimizing that error source. Radiation exchange between the junction and the walls of the apparatus was analytically investigated for some typical cases as observed from the data and found to be small but not negligible. For the 1600 watt Rijke test, temperature profile data taken through fitting 4 indicated that if the walls of the duct were at an average temperature

of 725°F and the junction at 534°F, an error in the gas temperature measurement of approximately -8.8°F would result. Radiation exchange to the duct walls was only significant near the heater for the 1600 watt Rijke test and the 900 watt Sondhauss test.

Thermocouple wires used were purchased to ISA "special limits of error" specifications. For the case of the chromel-alumel thermocouples, this means that the wire must match the National Bureau of Standards EMF-temperature curves within $\pm 2^\circ\text{F}$ from 0° to 530°F , and $\pm 3/8\%$ from 530° to 2300°F . The extension wires had an error $\pm 3.4\%$ from 0° to 530°F and $\pm 4^\circ\text{F}$ from 530° to 2300°F . Since all connectors were located in regions of uniform ambient temperature, they had no impressed temperature gradients, hence errors from this source were negligible. Reference junction errors were also negligible because the junctions were immersed in a well-stirred, de-ionized, demineralized ice bath. Bias and precision errors for the Doric microvoltmeter are given in Table B-1 of Appendix B.

Using methods outlined in Appendix A, gas stream temperature measurement uncertainties have been calculated for 70° and 1150°F and are shown in Table 6. The selected gas temperatures represent the extremes of measured values during the test program.

Heater Surface Temperature

Radiation thermometry

Radiation thermometers measure the temperature of an object without requiring physical contact. The ability to accomplish this is based on the fact that every object emits radiant energy and the intensity of this radiation is a function of its temperature. Thus, if radiation is thought of as a stream of photons and the flux of photons are focused on

Table 6. Summary of Gas Stream Temperature Measurement Uncertainty

Error Source	<u>70°F</u>	Precision Error σ (°F)	<u>1150°F</u>	Precision Error σ (°F)
	Bias Error B (°F)		Bias Error B (°F)	
Radiation	negligible	negligible	± 20	± 2
T/C Wire	± 2	± 0.2	± 4.3	± 0.4
Extension Wire	± 0.53	± 0.05	± 4.0	± 0.4
Readout (Doric)	± 0.11	± 0.05	± 4.7	± 0.46
Totals	± 2.07	± 0.29	± 20.8	± 2.1
Uncertainty	$\pm 2.65^\circ\text{F}$		$\pm 25^\circ\text{F}$	

a suitable detector, the temperature of the emitter can be determined. The IRCON Infrared Radiation Thermometer utilizes a lead sulfide crystal as a detector and has a spectral response up to about 2.4 microns. Three scales are provided on the IRCON Indicator Unit covering the range from 800° to 3000°F .

An optical system is provided that allows the user to view the target in the same manner as the detector. This is accomplished by a beam splitter. Dependent upon focusing distance, a target area is defined by a circular reticle which can be seen in the eyepiece located on the sensing head. Thus the visible image on the reticle is in focus to the eye when the infrared image is in focus on the infrared detector.

The IRCON sensing head was positioned above the exit plane of the test apparatus by mounting it on a swivel base and attaching it to a ring stand as can be seen in figure 14. A water cooled flange was attached to the sensing head to control the ambient temperature in the region where the detector was located. The lower end of the flange was approximately 4.5 inches above the exit plane of the test apparatus.

Tests were performed to determine whether the IRCON unit disturbed the acoustic field within the apparatus but proved to be negative. For a focal distance of 30.625 inches (front lens to heater), the reticle diameter was 0.204 inch. Use of a swivel base allowed the entire heater to be viewed without changing the focal distance hence keeping the reticle size constant.

Calibration

Two conditions must be met before the indicated reading represents the true temperature of the hot object being viewed. First, the emissivity of the surface must be known and second the reticle must be filled by the target. An emissivity control knob is provided which adjusts the voltage signal to the proper level. If the reticle is not filled because the target area is too small, the signal voltage level is reduced, and a special calibration is necessary to interpret the resulting voltage. In applying the infrared radiation thermometer to measure the heater surface temperature, neither the emissivity was known nor was the reticle filled by the target. The latter situation is depicted in figure 23.⁴ A special calibration which simultaneously resolves both problems is discussed in this subsection.

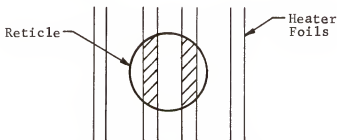


Figure 23. Heater foils partially fill reticle.

⁴When the reticle contains 2 foils, the measured temperature must be interpreted as the average temperature of both foils.

The calibration technique was based upon making comparative measurements at a given point, using a laboratory standard Leeds & Northrup Type 8622 Optical Pyrometer⁵ as the reference. With the IRCON sensing head positioned as mentioned previously, the downstream duct was removed and measurements were made by using both the IRCON and the optical pyrometer. Having the downstream duct removed allowed the optical pyrometer to be positioned close to the point in question and magnification of the target allowed a very accurate temperature measurement to be made. However, an optical pyrometer indicates the temperature of a blackbody radiator having the same spectral radiance as the object being viewed. For this reason, the indicated optical pyrometer readings had to be corrected for non-blackbody conditions.

Emissivity data for stably oxidized Inconel appearing in Table 41 of Reference (29) was used to correct the optical pyrometer readings using equation[10]. Several color photographs were taken of the hot heater using the same focal distance as that of the IRCON Sensing Head

$$T_{\text{Opt}} = T_{\text{bb}} / \epsilon_w^{1/4} \quad [10]$$

so that selected target areas could be well defined. The photographs⁶ were enlarged and the metal surface area contained within the reticle was calculated from measurements made by using a National Tools Inc. Mirroroptic Comparator.

⁵This instrument employs the "disappearing filament" method. While sighting through the telescope, the operator adjusts the current to an electrically heated, glowing filament in the telescope until its image merges with that of the object being measured and "disappears."

⁶Figure 41 in Chapter IV shows a color photograph of a hot heater for the 1600 watt power level. This photograph with circular targets superimposed was similar to those used during calibration.

These same preselected targets were then located on the heater by placing wires beneath the plane of the heater and making them intersect the foils at the points of measurement. It was estimated that a target site could be located to within a circle of radius of 0.05 inch of true position.

A large number of calibration points were obtained in this manner. Figure 24 shows the final form of the heater surface temperature calibration curve, where the ΔT represents the difference between the corrected optical pyrometer indicated temperature (T_{Opt}) and the IRCON indicated temperature. The various calibration points represent 3 heater configurations tested over 4 different days and encompass a number of different power levels (surface temperatures).

Equation[11] was used to correct temperatures read from the IRCON Indicator Unit,

$$T_h = T_h' + \Delta T \quad [11]$$

where T_h is the corrected heater surface temperature, T_h' the indicated heater surface temperature and ΔT is the heater surface temperature correction which is a function of the percent of reticle filled by target as given in figure 24.

Measurement uncertainty

Although at first glance, the method of measuring heater surface temperature might seem somewhat indirect, the fact is that it is better than any thermocouple technique that could have been used. In addition to the reasons given in Chapter II, the subject technique has the added advantage that it does not interfere with the acoustic field within the device.

It is obvious that the measurement uncertainty increases as lower values of α (percent reticle filled) are approached. An appraisal of

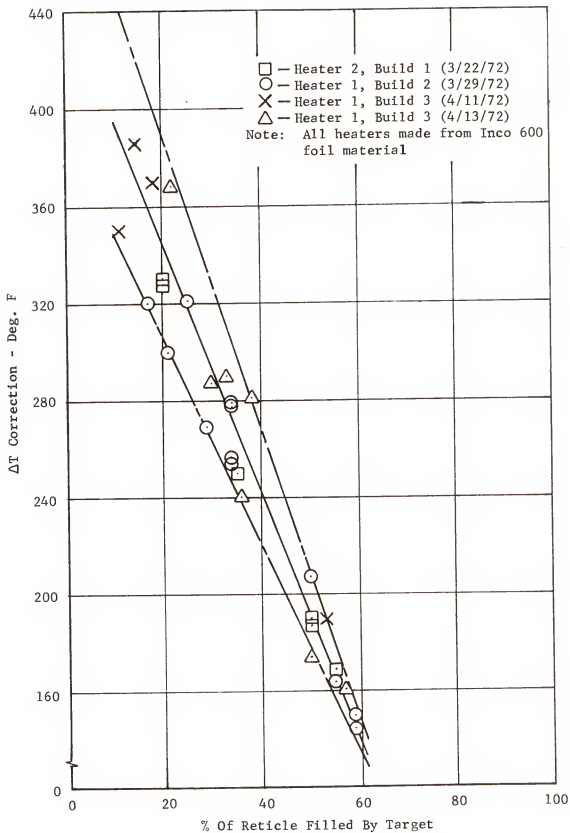


Figure 24. Heater surface temperature calibration.

the uncertainty for the entire set of heater surface temperature measurements was made by calculating the uncertainties for various values of α for the Basic Rijke Test Series. This test series consisted of 164 measurements of heater surface temperature. The frequency of selected values of α that were associated with the measurement is summarized in Table 7 along with the associated uncertainty. Range switch position 1 (800-1400°F) was assumed for the calculations because the greatest number of measurements were made using this range.

Table 7. Summary of Measurement Uncertainty Analysis for the Basic Rijke Test Series

α	15	20	25	30	35	40	45	50
Number of values above α	127	105	87	55	40	25	17	16
Percent of total above α	77.5	64.1	53.1	33.6	24.4	15.26	10.38	9.76
$\pm B_{T_h}$, °F	6.7	6.7	6.7	6.7	6.7	6.7	6.7	6.7
$\pm \sigma_{T_h}$, °F	15.6	14.1	13.1	11.4	9.8	8.7	7.1	6.0
Uncertainty, $\pm \Omega$, °F	37.9	35.0	32.3	29.5	26.3	24.1	21.0	18.7

Velocity

Hot-wire anemometry

Hot-wire probes have been successfully applied to the measurement of very low velocities such as those associated with free convective currents and to the measurement of particle velocities in acoustics research. Because of these applications, the hot-wire probe was chosen as a practical means of measuring velocities within the thermoacoustic instability apparatus. Calibration of the hot-wire probe is one of the most important aspects to be considered in hot-wire anemometry. In order to calibrate and use the hot-wire effectively, it is desirable that one

understand the heat transfer aspects of the hot-wire as well as have an appreciation of the physical situation occurring within the flow field to be probed.

The physical situation existing within the thermoacoustic instability apparatus is quite complicated. For instance, at any given location, the wire is subjected to velocities generated by the presence of the heater and also from the hot-wire itself. A steady free convective velocity field forms in the vicinity of the hot-wire. The heater generates both steady and fluctuating velocity fields; the steady velocity is due to buoyancy effects and acoustic streaming patterns whereas the fluctuating velocity field is associated with the standing wave pattern in the apparatus. Fluid temperatures vary both radially and longitudinally, especially in the near field of the heater. In addition, at the higher heater power levels, the heater foils radiate thermal energy in all directions. Before assessing the effects of the aforementioned thermal and flow conditions on the hot-wire measurements, it will be worthwhile to first discuss the operating principles of the hot-wire probe.

Hot-wire anemometry is based on the measurement of the convective heat loss from a heated sensing element. The heat loss depends upon the temperature, the geometrical shape, the dimensions of the sensor and on the fluid's velocity, temperature, pressure, density and thermal properties. If only one of the parameters varies, then the heat loss can be interpreted as a direct measure of the quantity in question, for example the velocity of a fluid of constant composition, temperature and pressure.

For purposes of discussion, we adopt a simplified heat transfer model for the actual hot-wire probe. The detecting element of a hot-wire

anemometer consists of a very fine short metal wire, which is heated by an electric current. The wire is cooled by the flowing fluid (taken here as air), causing the temperature to drop, and, consequently, the electrical resistance of the wire to diminish. In general, the wire is cooled by the simultaneous effects of heat conduction to the metal supports, free and forced convection, and thermal radiation. However, the effect of conduction, radiation and free convection is negligible when compared to forced convection heat transfer. Following the derivation presented in Hinze (30), for thermal equilibrium conditions, the heat loss per unit time must be equal to the heat generated per unit time ($I^2 R_w$) and is given by equation [12] .

$$I^2 R_w = C \pi k_f l_w (T_w - T_g) \left[0.42 (Pr)_f^{0.20} + 0.57 (Pr)_f^{0.33} (Re)_f^{0.50} \right] \quad [12]$$

In equation [12], I is the electric current, R_w is the total electrical resistance of a wire of length l_w and C is a unit conversion constant. The fluid properties such as the thermal conductivity k_f , the Prandtl Number $(Pr)_f$ and the density and viscosity appearing in the Reynolds Number $(Re)_f$, based on wire diameter, are all evaluated at the film temperature. The film temperature is taken as the average between the wire temperature T_w and the fluid temperature T_g .

The electrical resistance of the wire can be approximated by a linear relationship as in [13], where C_w is the first temperature coefficient of resistivity and R_r is the reference resistance at some reference temperature T_r .

$$R_w = R_r \left[1 + C_w (T_w - T_r) \right] \quad [13]$$

The temperature difference $(T_w - T_g)$ appearing in [12] can easily be expressed in terms of $(R_w - R_g)$, where R_g denotes the wire resistance

at the gas temperature T_g . After eliminating the temperature difference, equation [12] can be written in a more compact form as given by equation [14] .

$$\frac{I^2 R_w}{R_w - R_g} = A_w + B_w \sqrt{U_o} \quad [14]$$

where,

$$A_w = (0.42) \frac{C \pi k_f l_w}{C_w R_r} (Pr)_f^{0.20} \quad [15]$$

$$B_w = (0.57) \frac{C \pi k_f l_w}{C_w R_r} (Pr)_f^{0.33} \left(\frac{\rho_f d_w}{\mu_f} \right)^{0.5} \quad [16]$$

At this point it should be mentioned that a hot-wire can be either operated in a constant current mode or constant temperature mode. Since a constant temperature anemometer was used in this investigation, only those consequences pertaining to the constant temperature mode will be discussed. The temperature of the wire and consequently its resistance are kept as constant as possible by the electronic circuitry of the constant temperature anemometer. The anemometer has provisions for operating the wire at a constant overheat ratio which means that the difference in temperature ($T_w - T_g$) is fixed. So, if the fluid temperature is known, and the overheat ratio⁷ is held constant using the constant temperature anemometer, A_w and B_w are constant in equation [14]. In the practice of hot-wire anemometry, A_w and B_w are never calculated using [15] and [16] for instance, but are determined experimentally. If the voltage V across the wire is substituted for IR_w in equation [14] , a suitable equation for calibration purposes follows.

$$V^2 = A_w + B_w (U_o)^n \quad [17]$$

⁷The overheat ratio is defined as, $H = (R_w - R_g)/R_g$.

The constants A_w and B_w and the exponent n (usually near 0.5) are then fitted to the experimental calibration data.

Two types of calibrations need be considered. The first is a static calibration where the probe is exposed to a steady, low turbulence flow so that a relationship between DC bridge voltage and steady velocity can be determined. The second is a dynamic calibration where the probe is exposed to a fluctuating flow in order to obtain the response characteristics of the probe. This type of calibration is very difficult to accomplish and most users apply indirect methods. In the static calibration, a flow field is set up where the velocity can be readily determined by other means. For velocities above 40 to 50 ft/sec, a pitot tube is immersed in the flow near the hot-wire probe and simultaneous measurements of velocity and DC bridge voltage are made. At low velocities, below 15 ft/sec, a laminar flow is established in a tube and the center-line velocity is calculated from the measured flow-rate using Poiseuille flow relationships. The hot-wire sensor is positioned at the tube center-line and the corresponding voltages are recorded. The calibration in the velocity range from 15 to 40 ft/sec is determined by connecting both sets of data using equation [17]. Very often an electronic linearizer circuit is employed which yields a proportional relationship between the velocity and the DC bridge voltage. Since a linearizer was not used in this research program, it will be omitted from further discussion. Figure 25 shows the format for a typical static hot-wire calibration curve, where DC bridge voltage is plotted against velocity. At a velocity designated as U^* in figure 25, the curve deviates from theory and displays a unique trend. This region is influenced by free convection flow patterns from the hot wire and the curve blends into the zero velocity voltage,

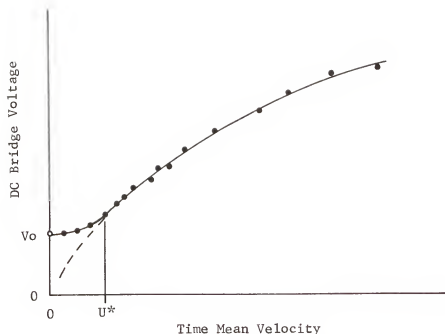


Figure 25. Typical hot-wire anemometer calibration curve.

designated V_0 . The hot-wire probe is highly sensitive to orientation in this region. Any hot-wire calibration at velocities below U^* must be made with the probe and flow oriented in the same direction relative to the gravitational field as in the actual application.

If the velocity fluctuations to be determined are relatively small compared to the mean or steady velocity, the static curve can be used to evaluate those velocity fluctuations. By taking the first derivative of the calibration curve, a hot-wire sensitivity curve can be obtained as shown in figure 26. Sensitivity has dimensions of millivolts per feet per second, and the fluctuating velocity is calculated by dividing the RMS fluctuating voltage by the sensitivity at the mean velocity in question.

Direct dynamic calibration may be performed in a flow in which sinusoidal velocity variations of known amplitude are superimposed on a constant mean velocity. As previously mentioned, the dynamic calibration is difficult to achieve and indirect methods are often used. In those

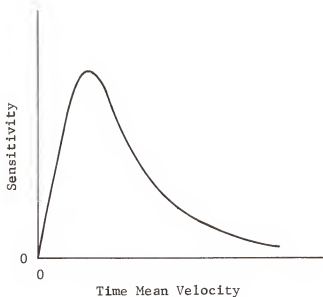


Figure 26. Typical hot-wire anemometer sensitivity curve.

cases the dynamic characteristics are measured by varying the electric current through the sensor, or by means of a microwave simulator. Fortunately, for the sake of this research program, a direct dynamic calibration was performed by Rasmussen (31) on a DISA miniature hot-wire probe having a sensor identical to the 55F33 probe. The fluctuating velocities were generated by applying an acoustic field using a sound driver. The ranges of velocity, amplitude of sound pressure and pressure and frequency are applicable to this study.

A number of very important findings appearing in Rasmussen's work will be discussed here because they were used in formulating the calibration procedure for the hot-wire probes used in this research. Figure 27 shows Rasmussen's measurements of hot-wire peak-to-peak voltage as a function of time mean flow velocity for different frequencies. At velocities below $U^* = 25$ cm/sec; that is, in the velocity range where natural convection becomes significant in static measurements, the data points are arranged about straight lines. The sensitivity is shown to

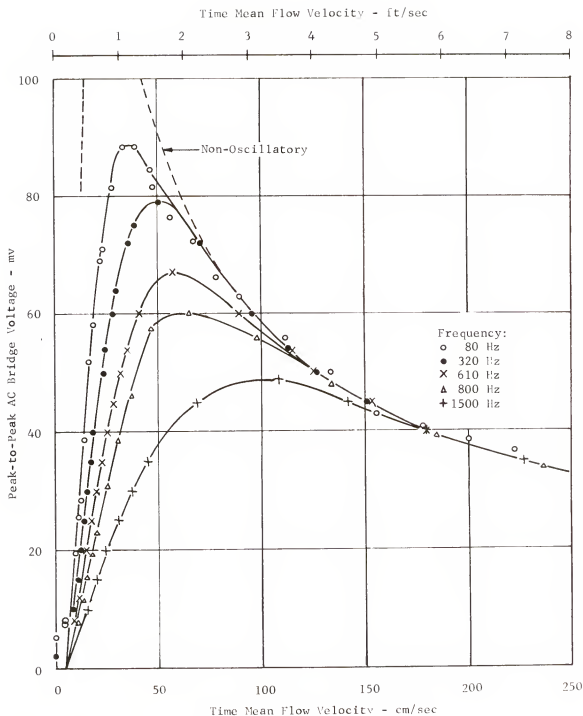


Figure 27. Hot-wire probe fluctuating voltage output as a function of time mean velocity and frequency after Rasmussen (31).

decrease with frequency at low velocities, and the point of maximum sensitivity moves towards higher mean flow velocities. For decreasing frequency, the shape of the constant frequency curves approaches that of

the first derivative of the static calibration curve which is shown by a dashed line. Rasmussen was able to show that for his probe, operating at an overheat ratio of 0.9, the velocity of the natural convection currents was approximately 10 cm/sec (0.328 ft/sec).

It was also shown that the fluctuating voltage signal was distorted when the steady flow velocity of the air was less than the fluctuating velocity amplitude (peak-to-peak value). It is obvious that in the absence of a steady flow velocity, the hot-wire will respond to a sound wave with a voltage whose frequency is twice that of the sound wave. Oscilloscope traces show that when the hot-wire is placed in a horizontal acoustic field with no steady flow velocity, only slight distortion exists in the voltage signal and is due to acoustic streaming effects. When the acoustic and flow fields are oriented vertically, the fluctuating voltage signal is greatly effected when the steady flow velocity is less than the fluctuating velocity amplitude. To understand this effect, note that the hot-wire is very sensitive to both velocity and temperature fluctuations. Rasmussen's work shows that at very low velocities, the temperature sensitivity becomes significant in proportion to velocity sensitivity. This is so because the flow will reverse twice during a period and every time it reverses it will carry back with it the heated wake of the hot-wire. That is the temperature of the thermal boundary layer around the wire undergoes two sudden increases during one period, and each temperature increase results in a commensurate decrease of the heat flux and the output voltage from the hot-wire.

The final point to be discussed in this subsection is the situation of measuring velocities in a flow field where the temperature is either temporally or spatially non-uniform. If high frequency temperature fluctuations were present, it would be virtually impossible to make

accurate velocity measurements. However, if the fluctuations were of a very low frequency, a temperature compensated probe could be used to make accurate velocity measurements. For the case of measuring velocities in a fluid having a spatially non-uniform temperature or having a uniform but different temperature from the probe calibration temperature, several techniques are available to insure accurate measurements. The most accurate method of compensation consists in calibrating over the temperature range in question, measuring temperature along with velocity. A second method, which may be used in gases with some accuracy, consists in keeping the overheating and hence temperature difference constant automatically, using a compensation coil placed at the sensor and connected to the anemometer. The third method, which is very accurate if performed with care, involves measuring the operating resistance at the point and temperature in question and then resetting a new probe resistance which is the original one times one plus the overheat ratio. This technique then allows the ambient temperature calibration curve to be used with accuracies associated in generating it. The first technique is impractical when the fluid temperature range is great and the velocities are very low. The second technique requires equipment which may or may not be available. The last technique offers the best compromise because no additional equipment is required and the accuracies are high; however this method takes a great deal of time and patience.

Calibration

In the previous subsection, the flow situation within the test apparatus was qualitatively discussed along with hot-wire anemometry theory, especially with regard to calibration. It remains to be shown that the method of hot-wire calibration used was adequate for the con-

ditions existing in the test apparatus.

For the Rijke tests, the greatest majority of velocity measurements ranged from approximately 2 to 12 ft/sec, frequencies of oscillation were from 170 to 230 Hz and gas temperatures were from 80 to 700°F. During the Sondhauss tests, velocities ranged from approximately 0.5 to 1.5 ft/sec, frequencies of oscillation were from 79 to 81 Hz and gas temperatures were from 70 to 1200°F. From the above synopsis and an examination of Rasmussen's data it appears that a static calibration is adequate for the determination of both the time mean and fluctuating velocities for the Rijke test series. Since the mean velocities are above U^* , orientation of the flow field with respect to the sensor is immaterial in the calibration fixture. However, because of the lower mean velocities existing in the Sondhauss apparatus, some of the velocity data, below 0.8 ft/sec, are subject to decreased accuracy and the sensitivity and hence the fluctuating velocity is also affected. For the small percentage of mean velocities below U^* , the static calibration curves are in error in this range because the calibration points were obtained with the flow field not oriented in the same direction as in the test apparatus. Using Rasmussen's data (31) it has been estimated that relative errors of 33, 25 and 11% exist for mean velocities of 0.5, 0.6 and 0.7 ft/sec, respectively.

Because of the low velocities encountered in the test apparatus, less than 15 ft/sec, velocity measurements made in a laminar flow field offered the simplest means of calibrating the hot-wire probes. Figure 28 shows the hot-wire calibration fixture used. The fixture consisted of a laminar flow tube, alignment block, probe adaptor and the hot-wire probe to be calibrated. Two sizes of tubes were used in order to broaden the range of laminar flow velocities. The tube dimensions,

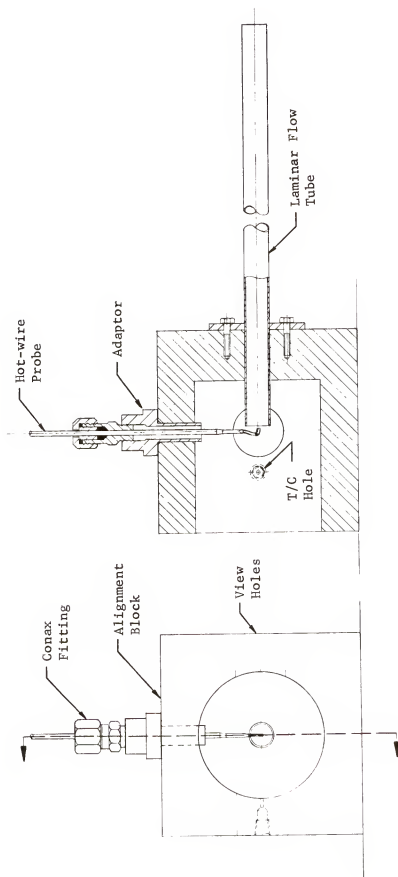


Figure 28. Hot-wire calibration fixture.

maximum centerline velocity and maximum tube Reynolds Number are given in Table 8 below.

Table 8. Laminar Flow Calibration Tube Data

Outer Diameter (inches)	Inner Diameter (inches)	Length (inches)	Maximum Centerline Velocity (ft/sec)	Maximum Reynolds Number
0.500	0.4305	36.0	10.0	1140.
0.375	0.309	24.0	18.8	1560.

The alignment block was a stainless steel cube which was carefully machined to accept the laminar flow tube and to allow the positioning of the hot wire sensor to within 0.06 inch from the end of the tube. A 2.50 inch diameter hole was machined into the block and provided a cavity which shielded the probe from stray air currents. The block was heavy enough to rest motionlessly during the calibration tests. A pair of 1.00 inch holes were provided to allow visual observation during the probe alignment procedure. After an approximate visual alignment was made, the probe was carefully moved, using the positioning device described in Chapter II to obtain the maximum voltage reading for a given calibration flow. The observation holes were taped shut after probe alignment to prevent stray air currents from entering the cavity. A small 0.04 inch chromel-alumel thermocouple probe was inserted through a fitting which was screwed into the block and positioned as close to the tube exit as possible without interfering with the flow field surrounding the hot-wire sensor.

Figure 29 shows a flow schematic of the hot-wire probe calibration system. High pressure breathing quality air was stored in a

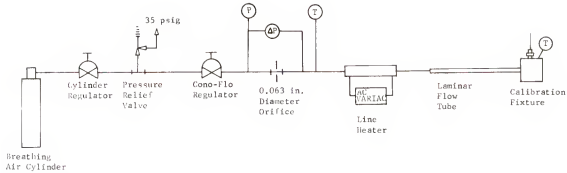


Figure 29. Flow schematic diagram of hot-wire probe calibration system.

pressure cylinder which was pumped up to approximately 2000 psig. The air was regulated to a pressure of 20 psig before being piped into a dome loaded Cono-Flow regulator which served as the flow controlling valve. The flow was measured by a specially calibrated 0.063 inch orifice. The orifice pressure differential was measured on a 0-15 inches of water Meriam Instruments Company U-tube manometer, upstream pressure on a specially calibrated 0-100 inches of water Barton Instruments Corporation pressure gage and the downstream temperature was measured using a chromel-alumel, 0.040 inch swaged wire thermocouple probe. A line heater was provided to maintain the calibration air temperature at the block.

The hot-wire calibration fixture was set up to provide a horizontally oriented flow field. Although the air flows vertically upward in the thermoacoustic instability rig, preliminary checkout runs were made with the both vertical upward and horizontal flows at the lowest attainable velocity⁸ of 1.7 ft/sec and no significant difference was noted. Subsequently, all calibration data was taken with horizontal flow. The 55A75 high-temperature probe had its sensor horizontally oriented while

⁸The lower velocity limit was set by the resolution or readability of the metering orifice U-tube manometer and upstream pressure gage.

the 55F33 miniature probe had its sensor vertically oriented in the alignment block.

Air velocity at the hot-wire sensor was calibrated on the basis of the velocity profile in the tube; see figure 30. Using Hagen-Poiseuille flow equations with a parabolic velocity profile, the maximum velocity at the centerline is twice the mean flow velocity. Since the wire was located symmetrically in the flow, the mean velocity across the wire will be some value less than the mean velocity in the tube.

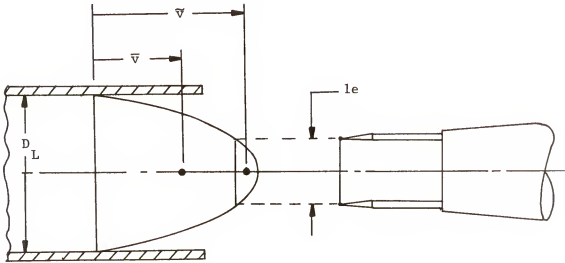


Figure 30. Hot-wire sensor located at centerline of laminar flow tube.

For the geometrical proportions of the tube and sensor as defined in figure 30, equation [18] gives the ratio of mean velocity at the sensor to the mean velocity in the tube.

$$\tilde{V}/\bar{V} = \frac{2}{3} \left[3 - 2 \left(\frac{l_e}{D_L} \right)^2 \right] \quad [18]$$

Table 9 presents a summary of the ratio \tilde{V}/\bar{V} for the various combinations of laminar flow tube and hot-wire probes used.

The mean velocity measured by the hot-wire can then be calculated from Hagen-Poiseuille flow relationships, equation [19], where the perfect

Table 9. Summary of Velocity Ratio \tilde{v}/\bar{v} for Tubes and Probes Used

Tube (in)	D_L (in)	Hot-Wire Probe	l_e (in)	\tilde{v}/\bar{v}
1/2	0.4305	55A75	0.0866	1.947
1/2	0.4305	55F33	0.0492	1.981
3/8	0.309	55A75	0.0866	1.895
3/8	0.309	55F33	0.0492	1.968

gas law was used to express the density in terms of pressure and temperature.

$$U_{cal} = \tilde{v} = \left(\frac{\tilde{v}}{\bar{v}} \right) \left(\frac{8R}{\pi D_L^2} \right) \frac{\dot{m}_L T_{blk}}{P_{amb}} \quad [19]$$

Due to the fragile nature of the hot-wire probes, a number of them broke during the test program. Each probe was assigned a serial number for identification purposes as given in Table 10.

Table 10. Hot-Wire Probe Preliminary Calibration Data Using a DISA 55A01 Constant Temperature Anemometer and a 20 Meter Long Cable

Probe Serial Number	DISA Probe Type	Ambient Air Temperature (°F)	Probe Cold Resistance (ohms)	Zero Velocity Voltage (volts)	Overheat Ratio	Probe Operating Resistance (ohms)	Frequency Response Frequency (kHz)	Air Velocity (ft/sec)	Tests Used	Comments
1 H ^a	55A75	74 77	6.41 6.86	8.45 8.16	0.6 0.6	9.17 9.92			Failed in Calibration	DISA Calibration POMA Calibration
2 H	55A75	68	6.90	8.19	0.6	9.97	2.24	10.0	5, 23	
1 "	55F33	74 74	3.85 3.86	5.35 5.362	0.8 0.8	6.93 6.93	21.3	2.6	1, 2, 3, 6	DISA Calibration POMA Calibration
5	55F33	70	4.05	5.283	0.8	7.29	114.	10.0	4, 7, 8, 9, 13, 14, 17, 23	
6	55F33	70	3.90	5.423	0.8	7.02	113.	15.0	5	

^aThese probes were originally calibrated at DISA and recalibrated at POMA using calibration fixture.

The first step in the calibration procedure was to measure the ambient temperature (T_g) and cold resistance (R_g). The hot resistance was then calculated from the overheat ratio and cold resistance and set

on the decade switches of the DISA 55A01 CTA. Measurement of a voltage, corresponding to the zero flow velocity (V_0), was made with the hot-wire sensor protected from stray air currents. The next step in the calibration was to measure the frequency response of the sensor plus anemometer due to a step change in probe voltage. A square wave generator was provided on the anemometer for this purpose. Table 10 presents a summary of all preliminary calibration data and lists the tests in which the given probes were used.

The final step in the calibration procedure was to set a given air-flow through the fixture and measure the orifice differential pressure, upstream pressure and downstream temperature, airstream temperature at the block and hot-wire DC and AC RMS bridge voltages. The flowrate was systematically varied until the entire calibration range was covered. An IBM 1130 computer program was used to convert all measurements to standard engineering units and to calculate the mean flow velocity, U_0 , and parameters $V^2 - V_0^2$ and $\sqrt{U_0}$ for equation [17] for all calibration test points. Additionally, the program had the capability of curve fitting the subsequent static sensitivity curve for incorporation into a hot-wire probe data reduction program. The computer programs are described in Appendix D. The AC RMS voltage signal was not used in developing the static calibration, but was merely used to insure that the flow was truly laminar.

Static calibration curves for probes 1, 5 and 6 are shown plotted in figure 31. Both DISA and P&WA calibrations are shown for probe 1.

The P&WA calibration data is seen to match the DISA calibration almost exactly over the full range of the curve. Figure 32 shows the static calibration curves for probes 1H and 2H (55A75). Only DISA calibration data is plotted in figure 32 for 1H because the probe failed

during calibration at P&WA. The DISA data allow the calibration curves to be extrapolated to a velocity of 1.0 ft/sec with confidence. This was done by reducing both sets of data to a dimensionless form of equation [17] which collapsed all of the data to essentially a single line.

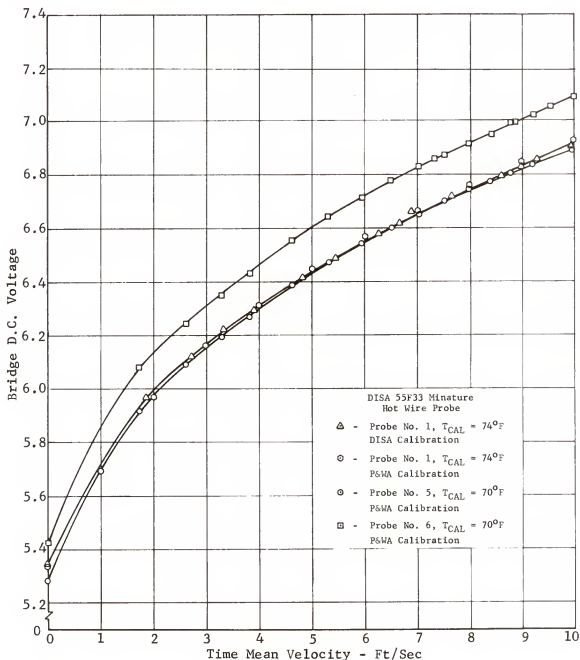


Figure 31. Static calibration curves for hot-wire probes 1, 5 and 6.

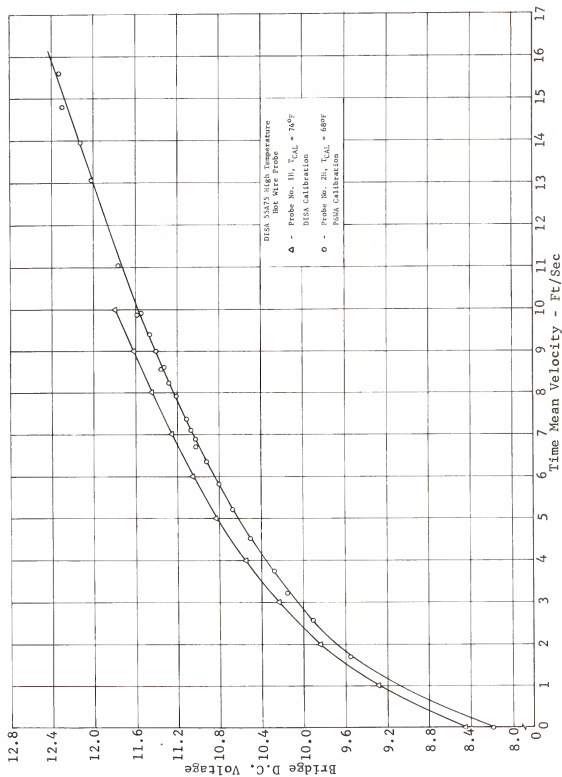


Figure 32. Static calibration curves for hot-wire probes 1H and 2H.

Measurement uncertainty

An analysis of the uncertainty involved in measuring the time mean and fluctuating velocity components using hot-wire probes is contained in Appendix B. The analysis considers two main sources of error in measuring the time mean velocity. The first source was due to combined errors in obtaining the static calibration curve while the second was due to the operational techniques involved in maintaining the overheat ratio constant. The uncertainty in measuring the fluctuating velocity was due to errors inherent in developing the sensitivity curve plus errors in reading the RMS AC bridge voltage on the DISA CTA.

Using the relationships developed in Appendix B, measurement uncertainty in time mean and fluctuating velocity components was estimated for both the miniature and high temperature probes. Typical operating conditions for each probe are summarized below.

Case 1

Operating conditions:

Test Number 2, Probe 6, 55F33

Hole 13, $r = 0$ (centerline)

$R_g = 4.10$ ohms, $R_w = 7.38$ ohms

$V = 6.48$ volts, $V_o = 5.423$ volts

$V_{AC} = 0.323$ volts, $U_o = 4.11$ ft/sec

Calibration conditions giving $U_o = 4.11$ ft/sec.:

$\bar{v}/\bar{v} = 1.981$, $D_L = 0.4305$ in., $C_c = 1450$

$P_{amb} = 14.72$ psia, $T = 70^\circ\text{F}$, $\dot{m} = 0.0001541$ lb/sec

Case 2

Operating conditions:

Test Number 5, Probe 2H, 55A75

Hole 14, $r = 0$ (centerline) $R_g = 8.13$ ohms, $R_w = 11.93$ ohms $V = 11.030$ volts, $V_o = 8.19$ volts $V_{AC} = 0.530$ volts, $U_o = 6.89$ ft/secCalibration conditions giving $U_o = 6.89$ ft/sec.: $\tilde{V}/\bar{V} = 1.947$, $D_L = 0.4305$ in, $C_c = 1422$ $p_{amb} = 14.757$ psia, $T = 68^\circ\text{F}$, $\dot{m} = 0.000271$ lb/sec.

Measurement uncertainty calculations for the hot-wire probes are summarized in Table 11 for the operating conditions given above.

Table 11. Estimated Hot-Wire Probe Measurement Uncertainties

Probe	55F33	55A75
B_{U1} , ft/sec	± 0.0864	± 0.1481
σ_{U1} , ft/sec	± 0.0405	± 0.0694
B_{U2} , ft/sec	± 0.00119	± 0.00149
σ_{U2} , ft/sec	± 0.00105	± 0.00114
B_{U3} , ft/sec	± 0.0801	± 0.2052
σ_{U3} , ft/sec	± 0.0845	± 0.1882
$B_{\bar{u}}$, ft/sec	± 0.0837	± 0.1124
$\sigma_{\bar{u}}$, ft/sec	± 0.0631	± 0.0864
Ω_U , ft/sec	± 0.3061	± 0.6542
$\Omega_{\bar{u}}$, ft/sec	± 0.2099	± 0.2853

Experimental Procedure

This section contains a brief discussion of the experimental procedure that were routinely used to insure that high quality data resulted from the experiments.

Prior to testing, all instruments were electrically energized and allowed to warm-up. Pre-run calibrations were performed on the B&K and GR 1900A wave analyzers and the DISA Constant Temperature Anemometer to insure stable operation and accuracy. All readout equipment was checked for zero while stripchart records were calibrated for both zero and full-scale span. Barometric pressure and room temperature were recorded both before and after testing.

After all instruments were properly preconditioned, heater electrical power was supplied by setting the Variacs to give a desired wattmeter reading. The test apparatus was given time to reach thermal equilibrium which was evidenced by monitoring a gas temperature probe inserted into the center portion of the downstream flange through fitting 4. Thermal equilibrium was usually achieved after 25 minutes from a cold startup. Another check on thermal equilibrium was to monitor the sound frequency at the center of the apparatus (fitting 7) and observe that a maximum and steady reading resulted. In fact, the most effective method for insuring repeatability of tests was by matching the sound frequency to within ± 0.2 Hz. This technique was extensively used for those tests that took more than one day to complete.

An unusual situation was observed to occur during testing. Acoustic standing wave patterns were found to be set up in the room as a result of coupling with the apparatus. The presence of a person in certain locations of the room caused an interference with the standing wave

pattern and a damping of the sound signal resulted. For very low heater power levels, less than 900 watts, the sound produced by the apparatus could be completely damped. Partial (slight) damping occurred in the 1000 to 1200 watt range and complete insensitivity to body damping was noticed above 1200 watts. Several favorable locations were found in the room where the presence of a person did not cause interference with the sound wave pattern and fortunately were located near the apparatus and instruments. To insure that a new variable was not introduced into the test program as a result of body damping, strip chart recordings were made of sound pressure at the center of the test apparatus with the person in the room and then removed from the room. While in the room, the person occupied the favorable position near the apparatus. Tests at 1000 watts showed no difference in sound pressure level for both cases.

Sound pressure, gas stream temperature and velocity measurements were made by probing through one fitting at a time while remaining fittings were plugged with stainless steel rods. This insured a minimum interference with the acoustic field within the apparatus. All data were hand recorded and later keypunched for processing through a series of simple IBM 1130 computer data reduction programs. Separate programs were written to reduce the microphone and hot-wire probe data. Gas and heater surface temperatures were reduced by hand. Data reduction is the subject of Appendix D.

CHAPTER IV

RESULTS AND CONCLUSIONS

Two goals were established at the outset of this dissertation. The primary goal was to experimentally investigate the thermoacoustic transduction process by measuring pertinent time mean and fluctuating parameters, especially in the near field of the heat source. A secondary goal was to experimentally investigate the relationships existing between the Rijke and Sondhauss modes of instability. Chapter III contains a description of the various tests designed to obtain the necessary data in support of these goals. This chapter is devoted to the study and correlation of those test data.

Results of Rijke Experiments

Acoustic Measurements

The first test that was performed using the Rijke configuration was a study of the limits of instability of the apparatus. See test number 11, Table 2. Maximum sound pressure (spatial) and frequency were measured over a range of heater power from 0 to 1600 watts. As shown in figure 33, the lower limit of instability was found to be 780 watts. For values slightly below 780 watts, sound oscillations would start but would damp out rapidly. The upper limit of 1600 watts was arbitrarily established and based upon not allowing the heater to exceed a maximum temperature of 1750°F.

Figure 33 shows that the system saturates above 1400 watts. A further increase in heater power above 1600 watts would probably cause

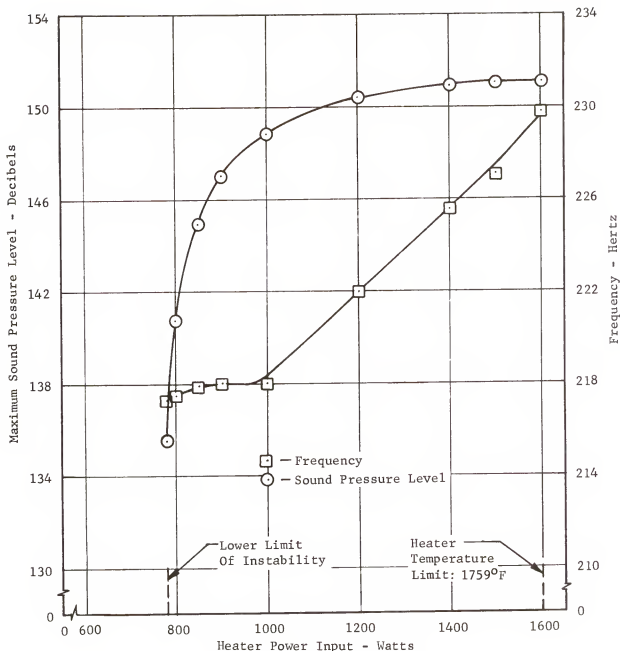


Figure 33. Variation of maximum sound pressure level and frequency with heater power input for the Rijke configuration.

the sound output to either remain constant or diminish. The frequency curve is shown to be approximately constant up to 1000 watts and increases with heater power above 1000 watts.

The non-linear character of the sound pressure level in figure 33 is of particular interest since linearized theory predicts a continuous

increase with heater power. See Kerwin's (13) analysis for instance. This non-linear behavior will be discussed later.

A complete set of microphone probe measurements were taken during the Basic Rijke Test Series, tests 1 through 4, for 1000, 1200, 1400 and 1600 watts of heater power. Test 12 at 900 watts of power is also included in this discussion. Tables C-1 through C-5, found in Appendix C, list all reduced microphone probe data. These tables include position, frequency, sound pressure level in decibels and sound pressure in psia.

Figure 34 shows the variation of RMS sound pressure with position and heater power as measured in the Rijke apparatus. With the exception of that portion of the curve in the vicinity of the heater plane, the general trend is as expected for a plane, standing wave pattern in an open-open pipe. At the lower power levels (900 and 1000 watts) the curve closely resembles one-half of a sine wave. As the power level increases, the distortion extends over a wider region and increases in amplitude. This distortion is due to the interaction of the sound waves with the solid heater surfaces. Non-linear behavior in the production of sound is again evident here by observing the spacing and crossing over of the constant heater power level lines above the 1200 watt level.

To determine whether the sound waves possess plane wave characteristics, a microphone probe was used to traverse the apparatus in the planes of holes 7 and 11 for 1000 and 1200 watts. Table 12 list the results. For a heater power level of 1000 watts, the radial sound pressure profiles are relatively flat at both locations, while for 1200 watts, only the profile at hole 11 appears flat enough to describe a plane wave. It appears that the influence of the heater is felt as far as the plane of hole 7.

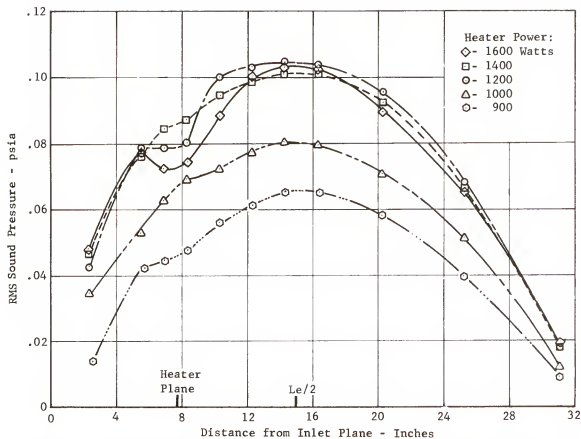


Figure 34. Axial variation of sound pressure in the Rijke apparatus for several values of heater power.

Table 12. Radial Measurements of Sound Pressure

Radius	Sound Pressure (psia)			
	1000 watts		1200 watts	
	Hole 7	Hole 11	Hole 7	Hole 11
0.0	.0688	.0111	.0896	.0158
0.25	.0688	.0111	.0890	.0158
0.50	.0688	.0111	.0873	.0160
0.75	.0688	.0111	.0850	.0158
1.00	.0700	.0111	.0792	.0161
1.25	.0711	.0111	.0792	.0160
1.50	.0723	.0112	.0850	.0161
1.65	.0734	.0112	.0850	.0161

Plotted in figure 35 is the spectral distribution of the RMS sound pressure measured at fitting 7 in the Rijke apparatus for 1200 watts of heater power. Reduced data for test 17 are listed in Table C-6. The fundamental and first harmonic frequencies were measured to be 222.2 and 444.1 Hz, respectively. The second harmonic was found to be extremely weak and therefore was not recorded. As evidenced by the sharp peak in the curve about the fundamental frequency and the greatly diminished amplitude of the first harmonic, the sound signal was dominated by the fundamental frequency and approached a pure tone. Similar data were measured at fittings 2, 9 and 11. Table 13 lists the measured fundamental and first harmonic frequencies and corresponding RMS sound pressures

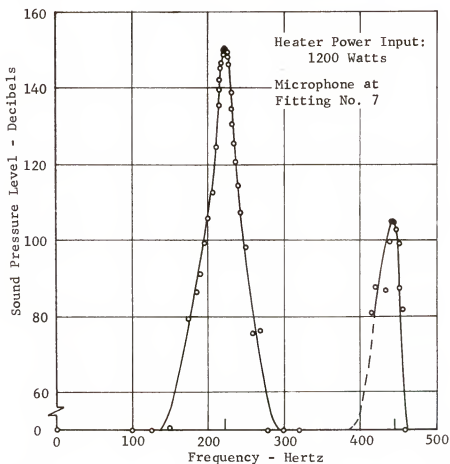


Figure 35. Spectral distribution of sound pressure level showing the fundamental and first harmonic frequencies in the Rijke apparatus.

and pressure amplitude ratios. The data show that certain portions of the tube are more respondent to the first harmonic than others. In the region of the maximum sound pressure (fitting 7) the amplitude of the first harmonic was weaker by one order of magnitude over other regions. Reference to this data will be made later in this chapter.

Table 13. Summary of Fundamental and First Harmonic Sound Pressure Data for 1200 Watts of Heater Power

Fitting Number	f_0 (Hz)	SPL_0 (db)	P_0 (psia)	f_1 (Hz)	SPL_1 (db)	P_1 (psia)	P_0/P_1
2	222.2	147.39	0.0640	444.4	119.19	0.00260	0.0406
7	222.2	150.57	0.0970	444.1	105.68	0.00055	0.00569
9	222.2	149.49	0.0656	444.1	121.79	0.00345	0.0526
11	222.2	139.89	0.0282	444.4	116.89	0.00202	0.0716

During test 18, an Altec sound driver was used to supply an acoustic signal of known frequency and amplitude to measure the effective length of the Rijke apparatus and to determine whether the natural frequency of the system was effected by the presence of the heater. These tests were performed with a cold heater. The reduced test data appear in Table C-7.

For an open-open pipe, the sound pressure nodes are located outside of the pipe. This is known as an end mass effect because some of the gas beyond the ends moves as a unit with the gas in the pipe. An effective length, greater than physical length of the pipe must then be considered in an acoustical description of the pipe.

From Chapter 8 of Kinsler and Frey (32), the effective length of a pipe with a flanged inlet and unflanged outlet can be calculated from equation [20]. For the dimensions of the Rijke apparatus, equation [20] gives $L_e = 34.086$ inches. From Table C-7 the natural frequency is 197.5 Hz

at an air temperature of 70°F. This gives an experimentally determined

$$L_e = L + 0.82 (D/2) + 0.6 (D/2) \quad [20]$$

effective length of 34.32 inches which is in close agreement with the calculated value.

To determine the effect of the presence of the heater on the natural frequency, the heater was removed and a new effective length was determined both analytically and experimentally. Without the heater, the length of the Rijke apparatus was 30.686 inches, giving a calculated effective length of 33.036 inches and an experimentally determined effective length of 33.10 inches. It can be concluded that since a relatively small change existed between the analytically and experimentally determined effective lengths for the two cases considered, the presence of the heater does not influence the natural frequency of the system.

The effective length of the Rijke apparatus was found to increase when the system was hot. Tables G-8 and G-9 contain reduced sound pressure data measured below the inlet plane and above the exit plane respectively for test 17 at 1200 watts of heater power. These data are plotted in figure 55 and show the nodal positions and true center for the acoustical system. The hot effective length is 36.9 inches as compared with 34.32 inches when cold.

An attempt was made to excite the system to oscillate at frequencies other than the fundamental by introducing an external sound signal in test 19. An Altec sound driver was used for this purpose. During this test, the heater was operative at 1100 watts of power. In general, regardless of the disturbing frequency, the Rijke apparatus responded to the sound input as it would for any random noise that was normally used

to initiate oscillations. However, as the driving frequency approached the fundamental or first harmonic frequency, a sound was generated that contained a beat frequency with an increase in amplitude.

The effect of cooling on the generation of sound from the Rijke apparatus was evaluated during test 18 and the data are listed in Tables C-10 and C-11. This was accomplished by substituting the water-cooled downstream duct for the original single walled duct. Initially, sound pressure measurements were taken over a range of heater power values for approximately adiabatic conditions which was obtained by venting the cooling jacket to the ambient surroundings. A second set of sound pressure measurements were made while water was circulated slowly through the cooling jacket. Figure 36 shows a significant increase in the sound pressure level for cooled walls when compared to the approximately adiabatic case. Data from figure 33, for the basic Rijke configuration, are also plotted in figure 36. Comparing data from the approximately adiabatic case with those from the basic Rijke configuration, indicates that very little heat is lost through the walls of the downstream duct for the latter case. The fact that the basic Rijke data fall slightly below the adiabatic data can be explained by hypothesizing that sound transmission losses are less through the double wall duct than through the single walled duct.

The use of a water cooled upstream duct in conjunction with the original single walled downstream duct was found to cause a negligible change in the sound pressure level over the basic Rijke configuration.

Velocity Measurements

Hot-wire velocity measurements were made upstream of the heater, in the plane of fittings 12 and 13, for tests 1 through 4 of the Basic Rijke

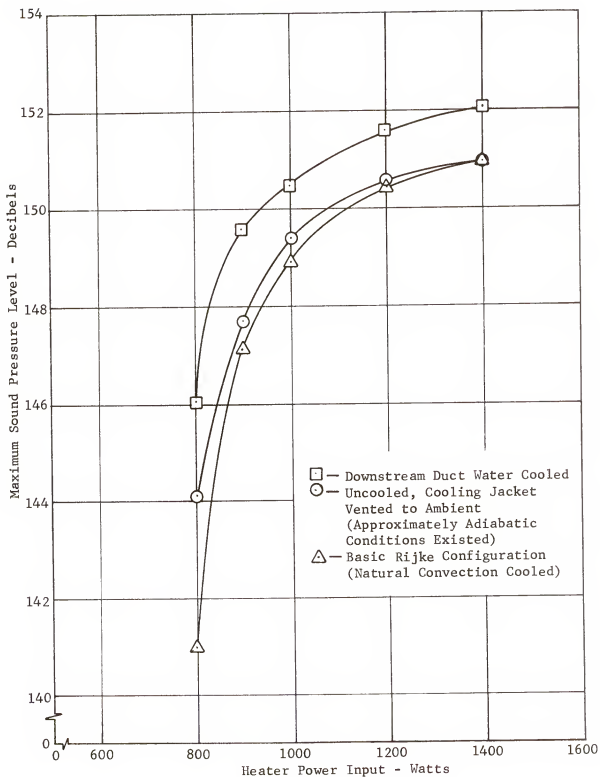


Figure 36. The effects of cooling on the generation of sound in the Rijke apparatus.

Test Series. These data points are tabulated in Appendix C as Tables C-12 through C-19, respectively. An examination of the tabulated data reveals that the fluctuating and time mean velocities are relatively uniform across the duct. The time mean velocity data were used in conjunction with the gas stream temperature data to calculate the mass flow rate for each heater power level and will be presented later.

Figure 37 gives an indication of how the time mean and fluctuating velocities vary with heater power in the region upstream of the heater. These data points were taken during test 11 with the hot-wire probe located at the centerline. The time mean velocity is shown to increase rather uniformly with heater power up to 1200 watts, and thereafter, decrease to a lower level and stay constant with further increases in power. The rising portion of the curve indicates that as heat is added to the system, a greater amount of air is induced to flow through the pipe due to increased buoyancy forces on the column of air. As additional energy is added to the system, viscous forces at the walls of the duct and at the heater surfaces become equal in magnitude to the buoyancy forces and limit additional increases in air flow. Figure 59, which shows calculated flow rate through the Rijke device as a function of heater power, illustrates this trend very clearly. The situation is further aggravated because at these higher power levels, the heater surface temperature is elevated to the point where thermal radiation and conduction heat transfer losses become appreciable. Losses induced by the fluctuating velocity field also contribute to the decrease in the pumping action of the system. The fluctuating velocity is shown to decrease with heater power up to approximately 1200 watts and remain constant thereafter. The effects just described are related to the non-linear behavior mentioned in connection with figure 33.

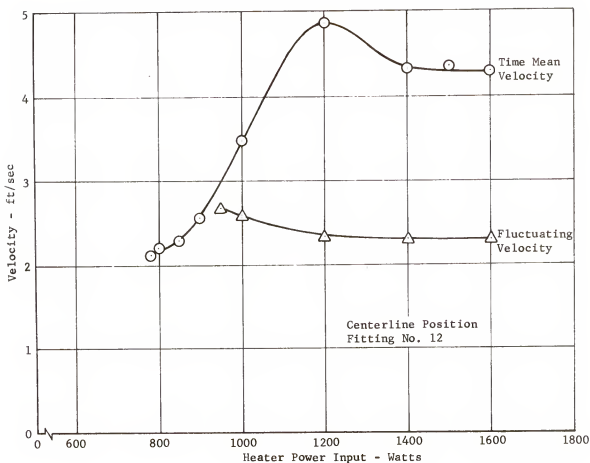


Figure 37. Variation of centerline time mean and fluctuating velocity with heater power for the Rijke configuration.

The development of the time mean and fluctuating velocity profiles, as the air flows upward through the Rijke apparatus, is shown in figure 38. These data were taken during the Velocity Study (test 5) for a heater power input of 1200 watts. Tables C-20 through C-23 contain the reduced data points from the Velocity Study. The fluctuating velocity profile is relatively uniform at the first three stations (fittings 12, 14 and 15) but becomes somewhat distorted at the last two stations (fittings 16 and above the exit plane). It is rather remarkable that the fluctuating velocity profile suffers as little distortion as it does upon passing through the heater. The time mean velocity profile suffers a large scale distortion upon passing through the heater and its shape

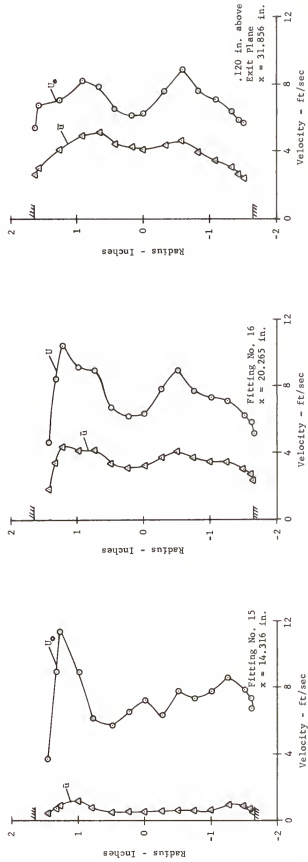
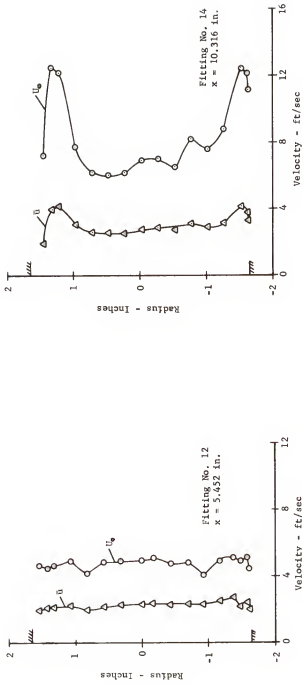


Figure 38. Time mean and fluctuating velocity profiles for the Rijke device for 1200 watts of heater power.

is directly related to the gas stream temperature profiles (see figure 44).

Particularly interesting results from the Velocity Study were obtained when the sound pressure and fluctuating velocity signals were simultaneously displayed on the dual beam oscilloscope for a given axial position. Figure 39 contains a set of oscilloscope photographs for the axial positions indicated. The photographs are arranged in the direction of flow for comparative purposes. The upper wave forms correspond to sound pressures measured at the wall while the lower wave forms correspond to the centerline fluctuating velocities. The sound pressure signals have been filtered in the wave analyzer to pass only the fundamental frequency, thus explaining why those signal appear to be pure sine waves when in reality they are not. The hot-wire, on the other hand, responds to all frequencies.

The most important feature to be noticed in the photographs is the phase relationship between the fluctuating velocity and sound pressure. The velocity wave leads the pressure wave at all stations except those in the immediate vicinity of the heater. There, at $x = 5.452$ in. and $x = 10.316$ in., the velocity lags the sound pressure. This feature is crucial in the transduction of thermal energy to acoustic energy to produce oscillations, and will be fully discussed later.

An examination of the velocity wave form shows that the fundamental frequency is exactly the same as for the pressure wave. The distortion in the wave form between the maximum amplitude peaks is not a first harmonic but is due to an effect discussed in Chapter III on page 77 .¹

¹Rasmussen (31) presents velocity wave forms which look distorted like the ones of this study while subjected to similar conditions.

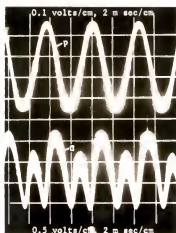
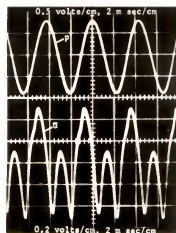
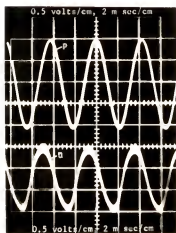
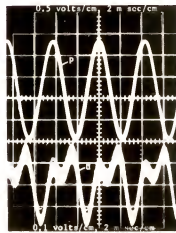
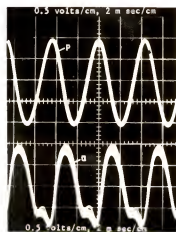
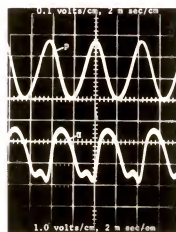
a. Inlet Plane ($x=0$)b. $x = 5.452$ in.c. $x = 10.316$ in.d. $x = 14.316$ in.e. $x = 20.265$ in.f. Exit Plane ($x=31.836$ in.)

Figure 39. Oscilloscope photographs of sound pressure and fluctuating velocity for various positions along the Rijke apparatus at 1200 watts of heater power.

Rasmussen (31) shows that when the acoustic and flow fields are vertically oriented, the fluctuating voltage signal is greatly effected when the fluctuating velocity amplitude ($2\sqrt{2}\bar{u}$) is equal to or greater than the through flow velocity.² To understand this effect, note that the hot-wire is very sensitive to both velocity and temperature fluctuations. Rasmussen's work shows that at very low velocities, the temperature sensitivity becomes significant in proportion to velocity sensitivity. This is so because the flow will reverse twice during a period and every time it reverses it will carry back with it the heated wake of the hot-wire. That is the temperature of the thermal boundary layer around the wire undergoes two sudden increases during one period, and each temperature increase results in a commensurate decrease of the heat flux and the output voltage from the hot-wire. These observations are substantiated by the data contained in Table 14. We can see that there

Table 14. Correlation of $2\sqrt{2}\bar{u}/U_o$ and V_b/V_a

X (Inches)	$\frac{2\sqrt{2}\bar{u}}{U_o}$	$\frac{V_b}{V_a}$
0.0	1.51	0.628
5.452	1.31	0.596
10.316	1.13	0.0
14.316	0.197	0.265
20.265	1.42	0.211
31.836	1.91	0.240

²For the vertical orientation of the wire and tube, the through flow velocity is the sum of the time mean velocity (U_o) and the free convection induced velocity from the hot-wire (u).

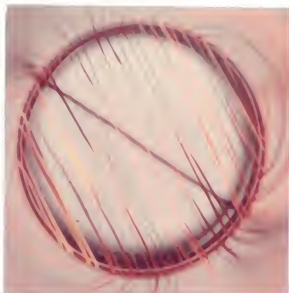
is a correlation between the ratio $2\sqrt{2} \bar{u}/U_0$ and V_b/V_a , where V_a and V_b are the peak-to-peak voltages of the larger and smaller pulses respectively. The free convective velocity emanating from the hot-wire (u) was not included in the ratio of peak-to-peak through flow velocities given in Table 14 because its magnitude was unknown, although small.

For instance, if a comparison is made between the velocity wave forms at $x = 0$ and $x = 5.452$ in. in figure 39, Table 14 shows that $2\sqrt{2} \bar{u}/U_0$ is greater for the velocity wave at $x = 0$ than at $x = 5.452$ in. and so is the ratio V_b/V_a . A physical explanation of this effect can be made on the basis that as the fluctuating velocity increases relative to the through flow velocity, fluid particles heated by the hot-wire traverse a greater distance during one period and cool by mixing with cooler surrounding fluid. During the flow reversal, cooler average fluid particles impinge on the hot-wire thus increasing the wire heat flux which gives rise to an increased voltage signal.³ The velocity wave form at $x = 10.316$ in. shows no distortion because the ratio $2\sqrt{2} \bar{u}/U_0$ is approximately 1.0. Actually if u had a value of 0.89 ft/sec or greater and were included in the ratio, the ratio would be 1.0 or less and would satisfy the physics of the problem. All of the velocity wave distortions are explained by the data in Table 14 except for the case at $x = 14.316$ in. (figure 39d). No explanation can be given to this discrepancy.

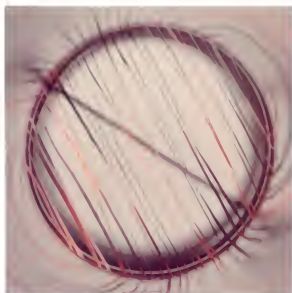
Heater Surface Temperature Measurements

Photographs and surface temperature measurements were taken of the heater during the Basic Test Series, tests 1 through 4. Figure 40

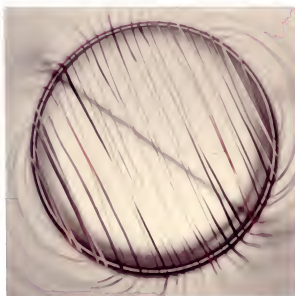
³As the through flow velocity approaches zero, the hot-wire voltage signal approaches a wave form with two equal peaks, having a frequency of twice the sound pressure wave.



a. 1600 watts



b. 1400 watts



c. 1200 watts



d. 1000 watts

Figure 40. Photographs of heater taken from above exit plane of Rijke apparatus.

shows photographs⁴ of the heater for the 4 heater power levels. The photographs were taken by mounting a camera at the same focal distance above the heater as for the IRCON Infrared Radiation Thermometer.

When cold, the heater ribbon had the appearance of a set of parallel foils. As the electrical power was progressively applied, the foils stretched and distorted as shown in the photographs. The configuration shown in the photographs were visually observed to be repeatable for any given power setting. When the electrical power was turned off, the foils returned to their original parallel shape.

The color photographs clearly show the hot spots, especially where two foils touch and electrically short out. As a word of caution, the color photographs are somewhat misleading in that they indicate much more temperature non-uniformity than was actually present. This discrepancy was noticed while viewing the foils from below the inlet plane, where due to the shorter length from the opening to the heater, a much more oblique view of the foils was possible and showed a more uniform temperature distribution. IRCON measurements should be used to compare the temperature of the various regions.

Figure 41 shows the location of the targets and reference planes used to identify the IRCON measurements. The targets are shown for the 1600 watt heater power level but are typical of those for other power levels. The reference planes are spaced at 30 degrees to each other. Plane A coincides with the plane of gas temperature and velocity measurements, while plane B is at 90 degrees to plane A. Heater surface

⁴Original copies of this dissertation contain color photographs of the heater in figures 40 and 41.

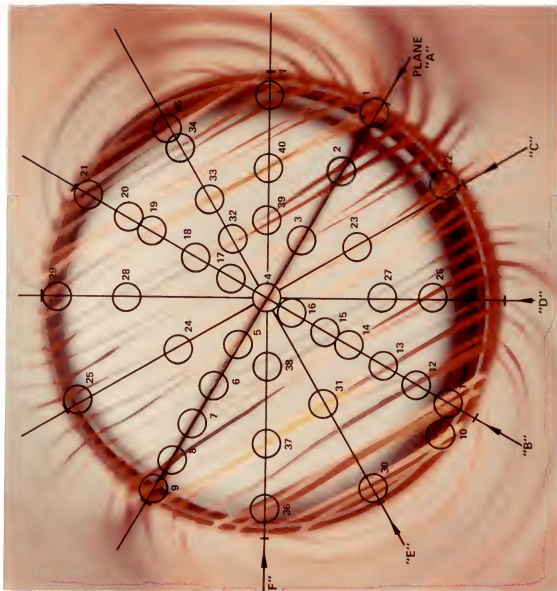


Figure 41. Location of targets on heater photograph for 1600 watts.

temperature measurements are listed in Appendix C as Tables C-24 through C-27. It should be noted that when two foils are contained within the reticle or circular target, the IRCON measurements must be interpreted as the average temperature of the two foils.

In order to obtain a clearer understanding of the heater surface temperature distribution, appropriate averaging of the data was performed. The heater was divided into 5 equal areas and the temperatures of points lying within each area were averaged to give one value typical of that area. The equi-area averaged heater surface temperatures were plotted at the mid-point radius of each equal area and are shown in figure 42. On an averaged basis, the temperatures are relatively uniform for each power level and show a trend that temperatures are hotter at the transite ring than at the center. The reason for this trend is due to the insulative effect of the transite material.

Gas Stream Temperature Measurements

Gas stream temperature data was taken at every heater power level during the Basic Rijke Test Series, tests 1 through 4. The thermocouple probe was traversed in one radial plane for every axial position available to obtain an adequate description of the thermal field within the device.

Figure 43 shows the distribution of the centerline gas stream temperature for the Basic Rijke Test Series. The curves very clearly display the steep gas temperature gradient in the vicinity of the heater which is a necessary pre-requisite for thermoacoustic transduction. A comparison of figures 42 and 43 shows that the heater to gas temperature difference is quite high, from 875 to 964 degrees F.

Radial gas temperature profiles for the 1200 watt heater power condition are shown in figure 44, and are arranged so as to show the develop-

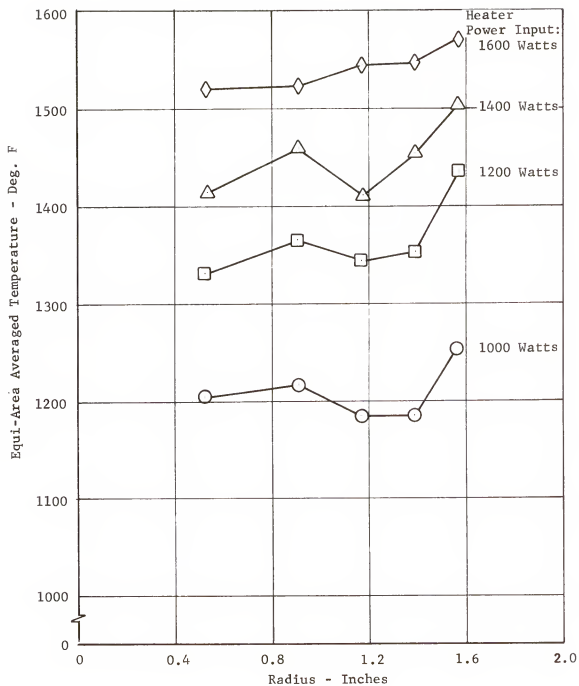


Figure 42. Equi-area averaged heater surface temperature distribution for Basic Rijke Test Series.

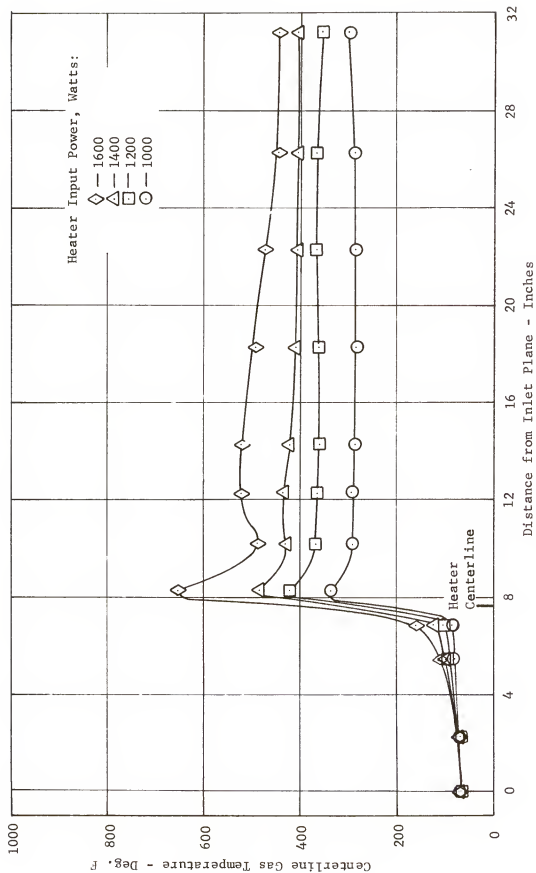


Figure 43. Centerline gas stream temperature distribution for the Basic Rijke Test Series.

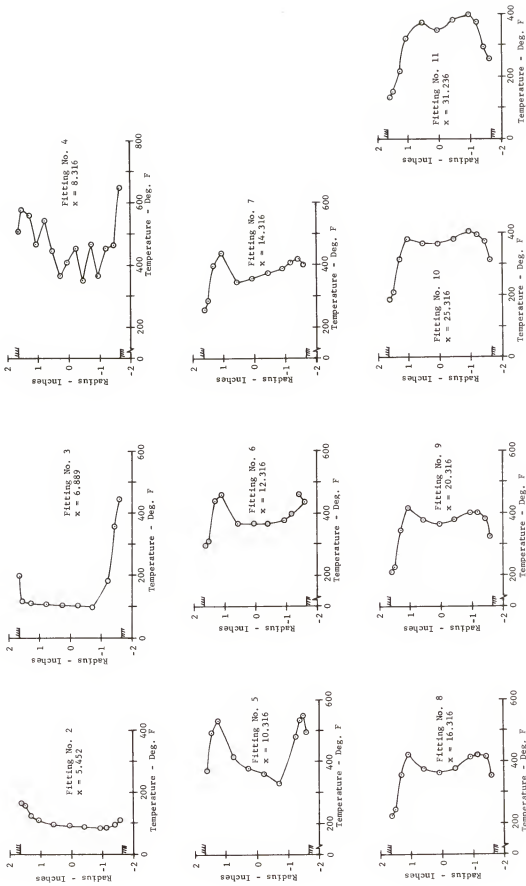


Figure 44. Time mean gas stream temperature profiles for the Rijke device for 1200 watts of heater power.

ment of the profiles in the flow direction. Starting with a uniform temperature profile at fitting 2, we see that at fitting 3 which is 0.6 inch from the rear edge of the heater foils, that the core region of the gas is still relatively cool but the wall layers are hot. At fitting 4, which is 0.6 inch from the trailing edge of the heater, the gas profile is very jagged. The peaks correspond to wakes from the heater foils while the depressed regions correspond to gas particles which passed between the foils. This situation is depicted in figure 45.

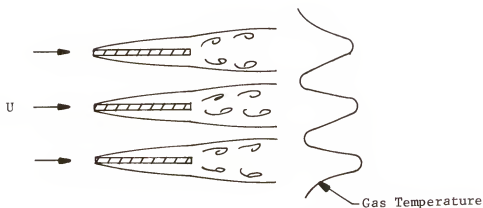


Figure 45. Gas temperature profile in wake region of heater foils.

The hot wake regions are mixed with the cooler gases by the time the gas flows past fitting 5 which is approximately 2.5 inches downstream from the heater. As the gas flows downstream, the profiles become similar, having a hot central core and cool regions near the wall.

Controlled Inlet Flow Tests

The effect of varying the inlet mass flow rate through the Rijke test apparatus was investigated in the Controlled Inlet Flow Test Series, tests 6, 7 and 8. The objective of these tests was to determine those inlet conditions which maximize the sound pressure in the device. Results of tests conducted at heater power levels of 1000, 1200 and 1400 watts are presented in figure 46.

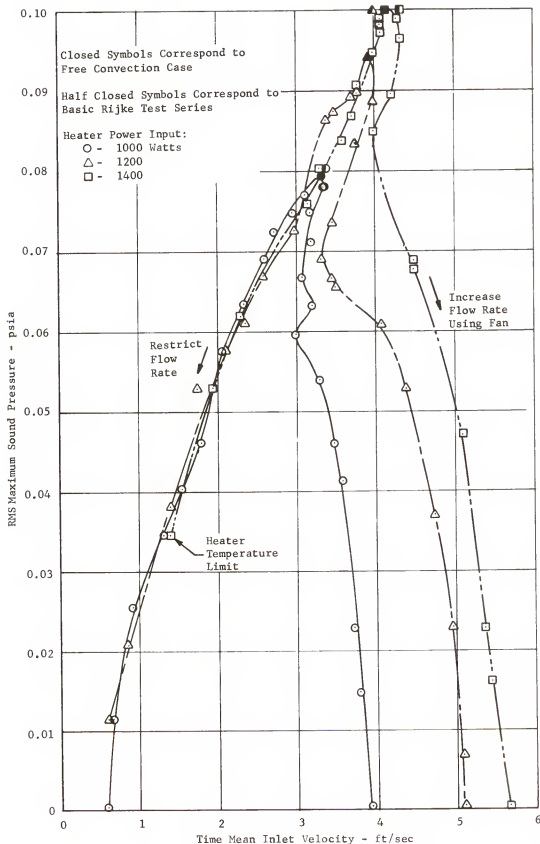


Figure 46. Results of controlled inlet flow tests on Rijke configuration.

The major result of this test series is that the non-augmented or free convective Rijke configuration produced the maximum sound output at all three power levels investigated. The closed symbols represent the free convection case during each test, using the test setup shown in figure 18. As additional flow was supplied by the fans, the velocity in general increased while the sound output progressively decreased. This effect is shown by the right leg of each curve. In a similar fashion, as the flow rate was decreased by restricting the inlet, the velocity likewise decreased and was accompanied by a reduction in sound output. This effect is shown by the left leg of each curve. For comparison, results from the Basic Rijke Test Series are plotted as half closed symbols on the curves. Good agreement exists between the Basic Rijke Tests and the free convection case of this test series.

Figure 46 also shows the result that sound is produced over a rather narrow range of inlet velocities. The lower velocity limits appear to converge upon values between 0.5 and 0.75 ft/sec. for all power levels, whereas, the upper limits progressively increase with heater power. The upper velocity limits are 3.93, 5.12 and 5.67 ft/sec. respectively for 1000, 1200 and 1400 watts of heater power. No explanation can be offered for the undulating behavior of the curves in the region where small amounts of flow have been added. However, as a speculation, this effect may be the result of unsteadiness in the flow caused by movements in the plastic side walls of the inlet plenum during testing.

Results of Sondhauss Experiments

Acoustic Measurements

Preliminary tests were performed with and without the 20 x 20 mesh screen located 0.100 inch downstream of the heater. It was found that

the Sondhauss system would not oscillate without the presence of the screen, although the system was on the verge of instability. For this reason, all subsequent tests were performed with the screen in place.

The first test performed using the Sondhauss configuration was a study of the limits of instability of the apparatus. As shown in Table 3, test 22 was conducted over a heater power range from 0 to 1000 watts to find those limits. The reduced test data is listed in Table C-28 of Appendix C. Figure 47 shows the lower limit of instability to be 90 watts. The upper limit of 900 watts was arbitrarily established when the heater surface temperature reached 1880°F, and not wishing to damage the heater, the test was terminated.

Figure 47 shows that the sound pressure level of the system increases sharply up to 200 watts, then increases at a lesser rate and finally approaches saturation above 800 watts in the same manner as the Rijke configuration did. However, in contrast to the Rijke configuration, the frequency curve is essentially constant over the range of power from 90 to 900 watts.

A complete set of microphone probe measurements were taken at 700 watts of heater power during test 20 and are listed in Table C-29. Figure 48 shows the axial variation of RMS sound pressure for this test. The curve shows the sound pressure distribution to be typical for that of a quarter wave tube, closed at one end and open at the other. The maximum sound pressure is shown to occur at the closed end.

The result of test 26 was most important to this program because it was demonstrated that both Rijke and Sondhauss modes of thermoacoustic instability can be made to occur within the same device and at the same heater power level just by changing inlet end conditions. Initially the heater power level was set at 900 watts while the inlet end was closed.

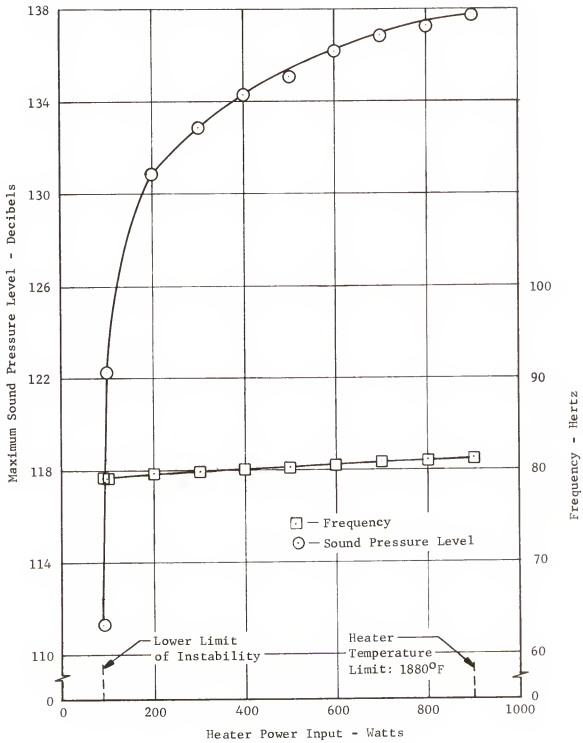


Figure 47. Variation of maximum sound pressure level and frequency with input electrical power for Sondauss configuration.

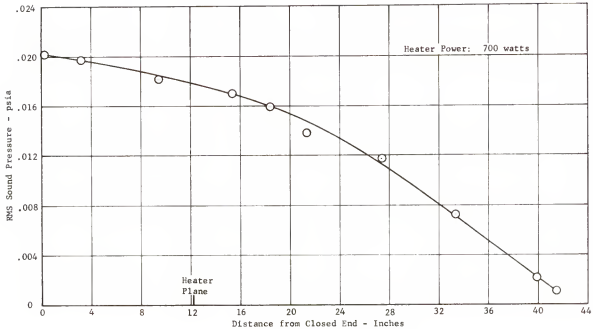


Figure 48. Axial variation of sound pressure in the Sondhauss apparatus.

As shown in figure 49, the device responded to the Sondhauss mode of instability where the maximum sound pressure level was 137.9 db and the frequency was 81.3 Hz. Next an inlet end disc with a very small hole corresponding 0.5% open area was installed. No oscillations were observed to occur. End discs with 3.25 and 14% open area were successively used but with the result that no oscillations occurred. Finally, when the inlet end area was 40% of the open area, Rijke mode instability was observed. The corresponding maximum sound pressure level was 124.9 db and the frequency was 167.4 Hz. By successively increasing the inlet area, the maximum sound pressure level was found to increase progressively whereas the frequency remained essentially constant as shown in figure 49.

The variation in sound pressure level with percent open area is the same effect as observed in the Rijke Controlled Inlet Flow Tests. Comparison of the maximum sound pressure levels associated with the Rijke

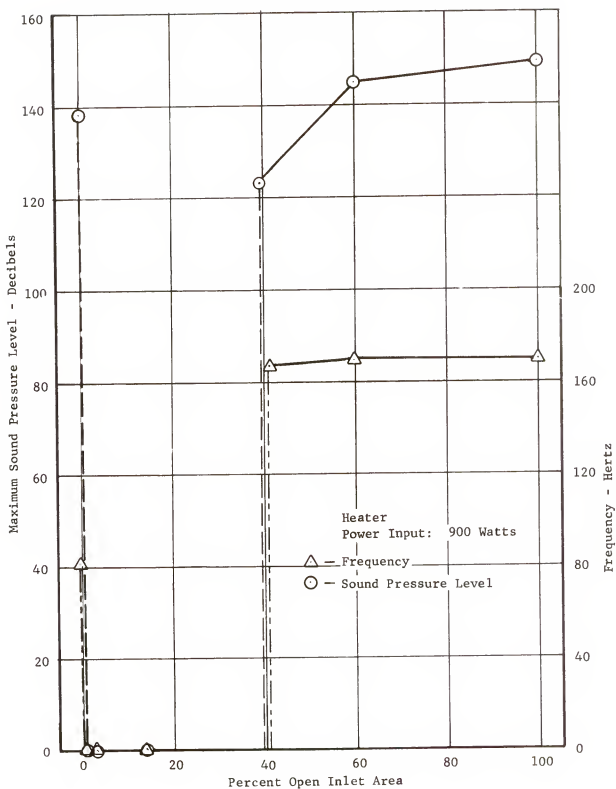


Figure 49. Transition from Sondhauss mode to Rijke mode instability in same apparatus by gradually varying inlet area.

and Sondhauss modes, indicates that the thermoacoustic efficiency must be higher for the Rijke configuration. This conclusion is based on the fact that the maximum sound pressure level is greater for the Rijke configuration when compared at the same power level, tube length and diameter. The relative location of the heater from the inlet end was closer to optimum for the Sondhauss configuration than for the Rijke configuration and therefore was not a compensating factor.

Velocity Measurements

Hot-wire velocity measurements were made by probing through fittings 13, 14, 15 and 17 during test 21 of the Sondhauss series. Although not as extensive as for the Rijke test series, velocity measurements were made to obtain some idea of the velocity field within the Sondhauss device. Velocity measurements were taken at the exit plane (fittings 13 and 14) to determine the magnitude and the direction of the flow so as to determine whether a toroidal flow pattern existed as reported by Feldman (24)⁵. The velocity was also measured at 2 other locations in the tube to check the extent of the inward air penetration and magnitude of velocity at those locations.

As a rough check on the direction of the flow, the 55F33 probe was first traversed across the duct with the sensor pointing toward the heater and then pointing away. The idea was that when the sensor pointed away from the direction of the flow, the sensor support prongs would form a wake region and reduce the velocity across the wire. When the sensor

⁵Feldman discovered a toroidal flow pattern existing at the exit of his pyrex glass Sondhauss apparatus, where air flowed constantly inward around the periphery of the tube and outwardly along the central core. He also discovered, using smoke, that the inward flow penetrated only 1 or 2 inches into the device. Further penetration of the smoke was by diffusion.

points toward the flow, the velocity will be higher than for the previous case. The latter situation is illustrated in figure 50.

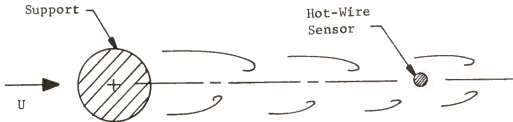


Figure 50. Cross-sectional view through 55F33 hot-wire probe at sensor showing wake region formed by support prong when sensor points away from the direction of the flow.

Since an outward flow was observed⁶ to exist in the central core region at the exit of the tube, velocity measurements taken with the sensor pointing toward the heater should indicate higher readings than when the sensor points away from the heater. Conversely, if a toroidal inflow exists at the tube periphery, the inwardly pointing sensor should detect a lower velocity than when the sensor points away from the heater. This situation was indeed found to exist in the plane of fittings 13 and 14. Figure 51 illustrates this situation schematically.

Figure 52 shows the time mean and fluctuating velocity profiles taken in the plane of fittings 13, 14, 15 and 17. The steady profiles at fittings 13 and 14 are composites of the velocity profiles for the sensor pointing toward and away from the heater. The connecting line between the inward flow (negative velocity) and outward flow (positive velocity) is speculative but should be representative. It is clear from the data that a toroidal flow pattern existed at the exit plane, but was non-symmetrical.

⁶The outward flow direction in the central core at the exit was observed by smoke patterns.

An inward flow was not sensed when the probe was traverse across the duct at fittings 15 and 17. However, an upward velocity was measured at these locations as shown in figure 52. Both time mean and fluctuating velocities are shown to be relatively constant along the device. The data indicate that some type of recirculating flow pattern existed. This will become more evident when the gas temperature data is discussed.

Tables C- 30 through C-35 of Appendix C contain the reduced velocity test data.

Gas Stream Temperature Measurements

Gas stream temperature profiles were measured at 10 axial stations along the Sondhauss device during test 20. The resulting gas temperature data is listed in Table C-40.

Figure 53 shows gas stream temperature profiles which are arranged so as to show their development in the flow direction. The temperature profiles are all relatively smooth when compared to similar Rijke gas temperature profiles (see figure 44) which appear jagged and heavily influenced by the convective flow patterns. The smooth temperature profiles indicate that thermal diffusion was the predominant mode of heat transfer in the device.

Gas temperature profiles at fittings 3, 4, 5 and 6, located in the immediate vicinity of the heater, show considerable asymmetry. Although temperature measurements were only made in one plane, and the results are not entirely conclusive, the data does suggest that perhaps a free convection cell existed. It is theorized that gases below the heater, near the wall tend to get hot due to the insulating effect of the lower or downstream duct which was vented to the atmosphere. Conversely, above the heater, gases near the wall are relatively cold due to water

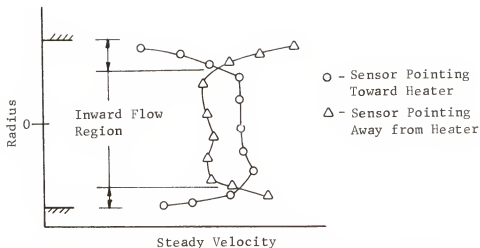


Figure 51. Illustration of velocity profiles at tube exit for the case of hot-wire sensor pointing toward and away from heater.

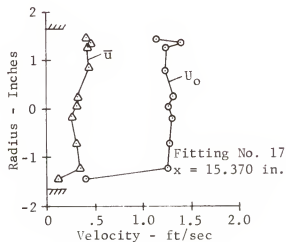
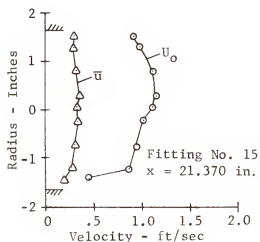
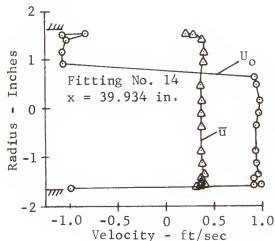
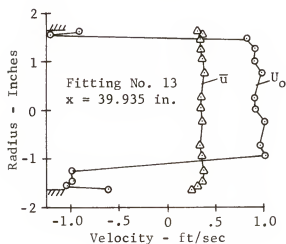


Figure 52. Time mean and fluctuating velocity profiles for Sondhauss configuration for 700 watts of heater power.

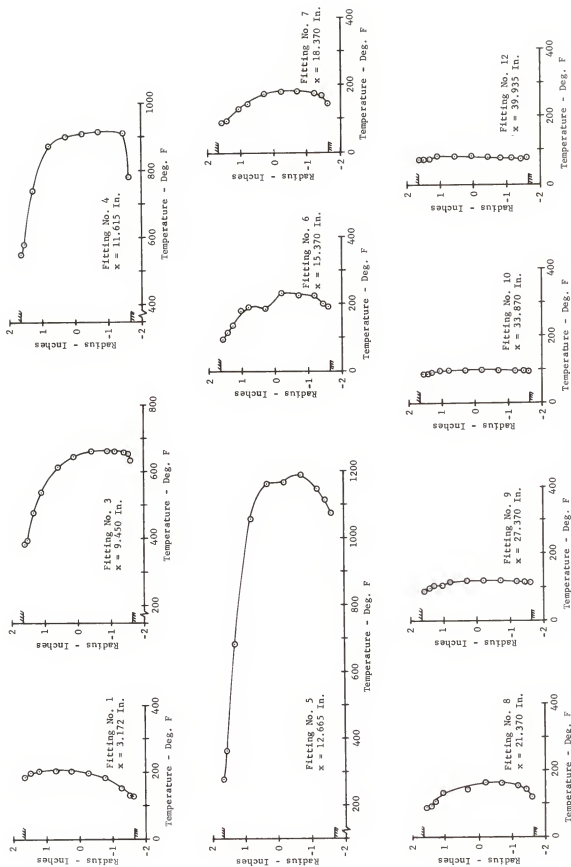


Figure 53. Time mean gas stream temperature profiles for the Sondhauss device at 700 watts of heater power.

cooling. As a result of buoyant forces, the cold gas flows downward along a portion of the wall while the hot gas flows upward along the opposite side of the wall.

Figure 54 shows the distribution of the centerline gas temperature for the Sondhauss test. The curve clearly displays the steep gas temperature gradient in the vicinity of the heater in a manner similar to that observed during Rijke tests (see figure 43). Unlike the Rijke temperature profile, the gas below the heater is at a higher temperature than above the heater.

IRCON heater surface temperature measurements were attempted, but due to the presence of the screen above the heater, targets could not be located with any accuracy. For this reason the surface of the heater was just scanned for temperature level and indicated that the heater was much more uniform in temperature than for the Rijke test. The average heater surface was measured to be 1606°F with a variation of approximately $\pm 175^{\circ}\text{F}$.

Discussion

The general concepts of thermoacoustic instability have been presented in Chapter I. The purpose of this section is to discuss results from the test program which support these concepts.

A gas phase, tubular system which contains a heat source can display pressure instability and produce sound which is maintained by the heat source. For this to occur, it is necessary that conditions be established to promote the transduction of thermal to acoustic energy. The transfer of energy takes place in the region of a steep temperature gradient, fixed in space, as the acoustic waves amplify in passing through this high gradient region. Another condition must be met if the oscillations

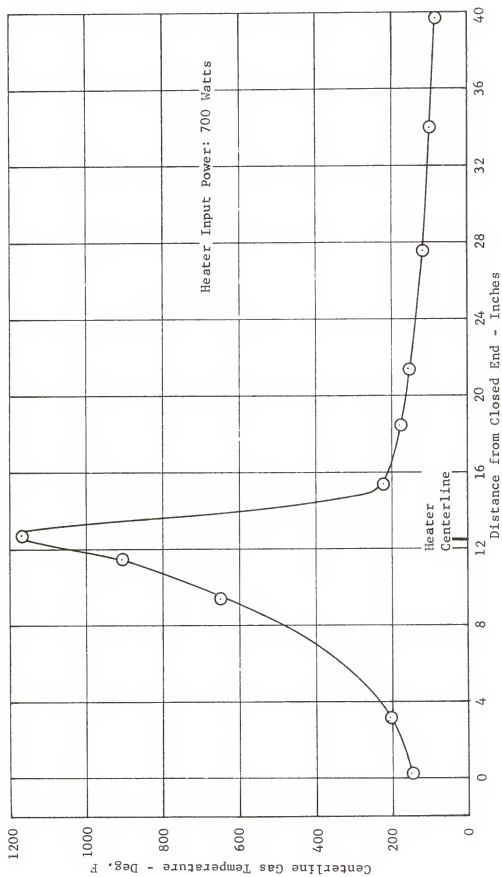


Figure 54. Centerline gas temperature profile through Sondhauss apparatus.

are to be maintained for any length of time. The heat source must be located in a region within the device such that the resulting fluctuating heat transfer and fluctuating pressure are positively correlated over a cycle of oscillation. In other words, the heater must be located in such a position that acoustic waves reflected from the ends can be energetically reinforced upon passing through the heater zone and overcome losses. If this be the case, a standing wave pattern is established and sound, which is predominantly at the fundamental frequency of the system, is produced.

Measurements have been made during the test program which support the concepts just stated. The existence of a steep temperature gradient within the Rijke device is shown in figure 43, where gradients from 182 deg F/in. to 354 deg F/in. were measured for 1000 and 1600 watts of power. An even greater temperature gradient of 360 deg F/in. was measured during the Sondhauss test series for only 700 watts of heater power as shown in figure 54. One fundamental difference existed in the manner in which these high temperature gradients were developed. In the Rijke device, heat was transferred by convection due to both time mean and fluctuating velocity components and also by thermal diffusion. The gradient region appears as a forward facing step to the flow. The temperature field in the wake of the heater was primarily set by the induced free convective flow pattern in the device. In the case of the Sondhauss device, the temperature gradient was established primarily by thermal diffusion and was very strongly influenced by the wall temperature. The temperature gradient region appears peaked with the gas temperature diminishing rapidly beyond the peak to a relatively uniform, low temperature level.

Figure 55 is a composite curve showing the axial variation of radially averaged values of sound pressure, phase angle and time mean and fluctuating velocity for the 1200 watt Rijke test. Before discussing the data

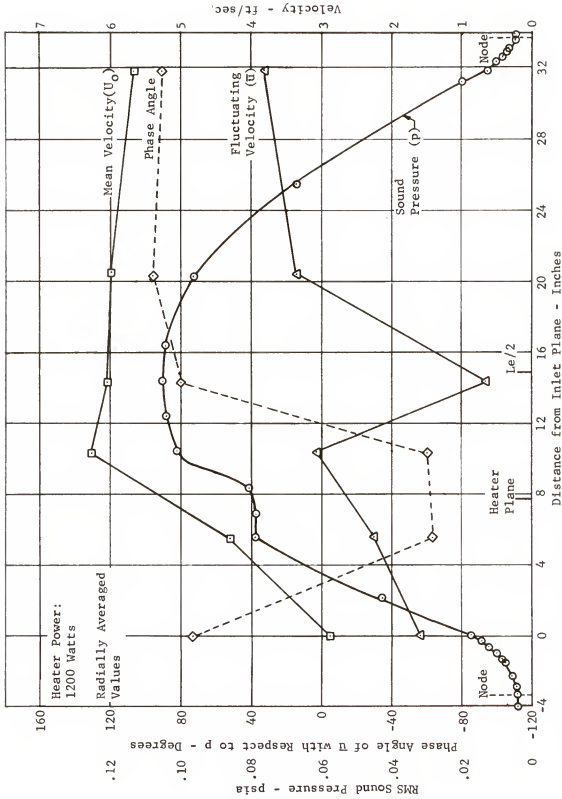


Figure 55. Axial variation of averaged values of sound pressure, phase angle and time mean and fluctuating velocity for the Rijke configuration.

contained within the composite curve, it will be helpful to first consider the behavior of these parameters under more ideal conditions.

For a standing acoustic wave pattern in a lossless, sourceless open-open tube, the sound pressure and fluctuating velocity are expressed by equations [21] and [22] for the fundamental mode.

$$p = A_1 \sin \frac{\pi x}{L} \sin \frac{\pi a_0 t}{L} \quad [21]$$

$$\frac{\bar{u}}{a_0} = A_1 \cos \frac{\pi x}{L} \cos \frac{\pi a_0 t}{L} \quad [22]$$

Figures 56 a and b show the sound pressure and fluctuating velocities schematically for the regions; $0 \leq x \leq L/2$ and $L/2 \leq x \leq L$, respectively.

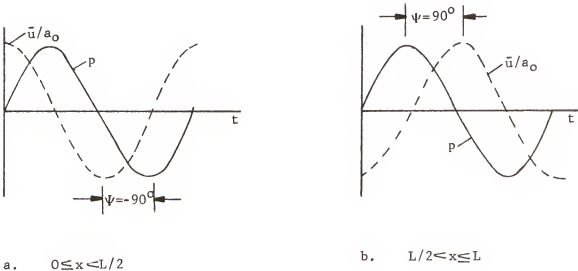


Figure 56. Relationship between sound pressure and velocity waves in an open-open tube.

Figure 57a illustrates the relationship of ψ , the phase angle between the velocity and pressure waves, while figure 57b shows the spatial variation of the fluctuating pressure and velocity.

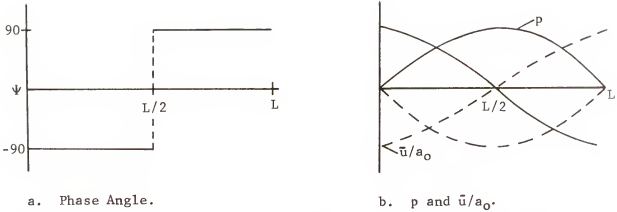


Figure 57. Spatial distribution of phase angle, sound pressure and fluctuating velocity for an open-open tube.

By comparing figures 55 and 57 we can see that, in general, there is agreement in the behavior of the parameters between the open-open tube and the Rijke device with the exception of the region near the heat source.

The sound pressure curve in figure 56 has a sinusoidal shape with a distorted region in the vicinity of the heater. As mentioned previously, the distortion in pressure amplitude was due to an interaction of the sound waves with the solid heater surfaces. The fluctuating velocity curve for the Rijke device agrees with the ideal open-open velocity curve in the downstream region of the heat source only. The velocity is a maximum at the end of the tube and approaches zero at the center of the Rijke device where a pressure maximum exists. However, in the region from the inlet plane to just downstream of the heater, the velocity curve deviates from the ideal which is a direct result of the thermoacoustic transduction process.

The phase angle curve also shows good agreement with the ideal case in the downstream half of the device but deviates significantly in the upstream half of the device, especially near the heater. We can see that the pressure leads the velocity wave by only 65° instead of 90° as for the simple open-open tube. This feature is crucial to the thermoacoustic

transduction process as will be demonstrated below.

If we draw a vector diagram for the acoustic parameters, and designate the region just downstream of the heater by subscript 1 (plane of fittings 2 and 12) and downstream by subscript 2 (plane of fittings 5 and 14) we get the results shown in figure 58. The phase angle between p_2 and p_1 (ψ_{p2}) was unfortunately not measured in this program but it is known to be small. For instance Kerwin (13) measured $\psi_{p2} = 15.5^\circ$ for his experiments. Assuming that the fluctuating heat transfer q is in phase with \bar{u}_1 ,⁷ we see that q lags the average sound pressure in the heater region, p_{av} , by phase angle ψ_r . For the test data considered, ψ_r is estimated to be between -50° and -55° lagging behind p_{av} . Therefore, it is evident that q has a component q' which is in phase with the average acoustic pressure in the heater zone. Thus the fluctuating heat transfer and sound

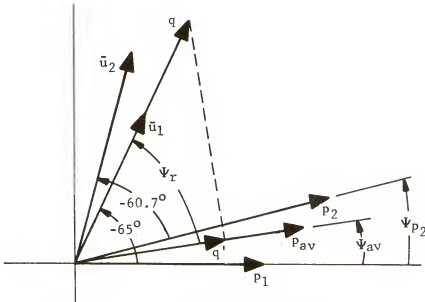


Figure 58. Vector diagram for acoustic parameters.

⁷Kerwin (13) and Malling (20) have both found that the phase lag between q and \bar{u}_1 is small. Calculations presented later in this chapter also confirm this assumption.

pressure will be positively correlated over a cycle of oscillation and by Rayleigh's Criterion (presented in Chapter I) the oscillations will be maintained. Actually, the oscillations will be maintained even if q lags \bar{u} significantly as in those cases where the frequency is relatively high, just so long as $\Psi_r \geq \pi/2$, lagging.

The detailed acoustic measurements made for the 1200 watt Rijke test point, allowed a number of interesting calculations to be made. First, the mass flow rate of air flowing through the Rijke device was calculated using equation [D-8] of Appendix D and the measured gas temperature and velocity profiles taken upstream of the heater through fittings 12 and 13. The results of the mass flow calculation are plotted in figure 59. For 1200 watts, $\dot{m} = 0.01732$ lb/sec. The next step was to calculate the bulk temperature and radially averaged time mean velocity, U_{av} , for 1200 watts at every station where velocity data was taken. Equation [D-12] and [D-16] of Appendix D were used for this purpose.

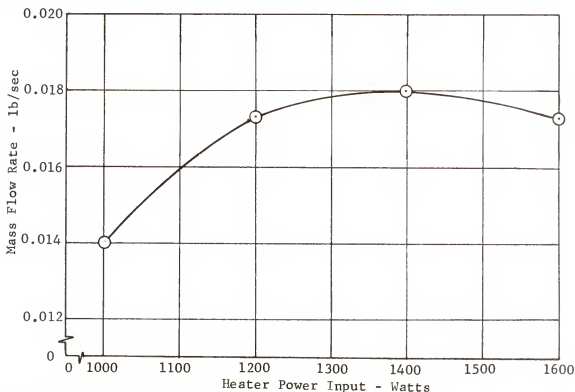


Figure 59. Calculated air flow rate through apparatus for the Basic Rijke Test Series.

The fluctuating velocity was averaged across the stream and was designated \bar{u}_{av} . Measured sound pressure is, of course, understood to be a radially averaged value. To complete the preliminary calculations, an acoustic intensity was calculated at each velocity measurement station using equation [23] (see Ingard and Morse (33)). The calculated values

$$I = p \bar{u} \quad [23]$$

just discussed are summarized in Table 15. Subscripts av will be dropped from U , \bar{u} , T and ρ in the remainder of this chapter for simplicity of notation.

Table 15. Summary of Calculated Parameters for 1200 Watts

Fitting (no.)	x (in.)	p (psia)	\bar{u}_{av} (ft/sec)	U_{av} (ft/sec)	T_{av} (°F)	ρ_{av} (lbm/ft ³)	I (watts/in ²)
Inlet	0.0	.0175	1.590	2.850	70	0.0698	0.0377
2, 12	5.452	.0788	2.252	4.280	125	0.0680	0.241
5, 14	10.316	.1008	3.073	6.257	394	0.0465	0.419
7, 15	14.316	.1046	0.666	6.010	360	0.0485	0.093
9, 16	20.256	.0958	3.358	5.970	355	0.0488	0.436
Exit	31.856	.0180	3.791	5.650	310	0.0514	0.0925

The total heat input to the fluid (time mean plus fluctuating) was calculated for various sections using equation [24], where a and b refer to fitting locations and the enthalpy (h) is evaluated at the average

$${}_aQ_b = \dot{m} (h_b - h_a) 1055 \quad [24]$$

temperature as given in Table 15.

$${}_2Q_5 = 1187 \text{ watts}$$

$${}_2Q_e = 830 \text{ watts}$$

$${}_1Q_e = 1005 \text{ watts}$$

For 1200 watts of heater input power, 1005 watts were transferred to the fluid between the inlet and exit planes of the Rijke device. This means that 195 watts are lost to the surroundings or 16.25% of the heater input power is lost.

Calculations were performed to estimate the magnitude and phase angle of the fluctuating heat transfer. An analysis due to Carrier (14)⁸ was used for this purpose. The fluctuating heat transfer, q , will be calculated in two different ways. First, a simple heat, mass and momentum balance for the fluctuating quantities is written across the heater. The subscript 1 will designate a section upstream of the heater (plane of fittings 2 and 12) while 2 designates a section downstream of the heater (plane of fittings 5 and 14). The equations can be manipulated to yield equation [25], given by Carrier.⁹ We can see from [25] that the acoustic wave is amplified in passing through the heater region. Solving [25] for

$$\frac{\bar{u}_2}{\bar{u}_1} = 1 + \left(\frac{\gamma - 1}{\gamma P_{atm}} \right) \frac{Jq}{\bar{u}_1 \pi D^2 / 4} \quad [25]$$

q allows an estimate of q to be made which is based upon experimental data. However, the accuracy of the subsequent answer is dependent upon the validity of the assumption of small perturbations in the vicinity of the heater. The second method of calculating q uses the results of Carrier's boundary layer analysis given by equation [26]. The term ν is defined by equation [27]. In these equations, ω is the circular frequency of the oscillation, l_h is the length of the heater strip in the direction of

⁸Carrier's analysis is presently the only analysis that is available for calculating the fluctuating heat transfer from a heated strip immersed in a pulsating flow.

⁹A typographical error was found in Carrier's paper which omitted \bar{u} , from the denominator of equation [25].

the flow and ρ , C_p and k are the fluid's density, specific heat and thermal conductivity. The velocities \bar{U} and U_o are taken as mean values across the heater zone.

$$\frac{q}{Q} = \left[-\frac{i}{2} \frac{U_o}{\omega l_h} \left\{ (\pi \nu l_h)^{\frac{1}{2}} \operatorname{erf}(\nu l_h)^{\frac{1}{2}} - \exp(-\nu l_h) + 1 \right\} \right] \frac{\bar{U}}{U_o} \quad [26]$$

$$\nu = \frac{1}{2} \left[\left(1 + \frac{4i k \omega}{C_p U_o} \right)^{\frac{1}{2}} - 1 \right] \frac{\rho C_p U_o}{k} \quad [27]$$

The argument of the error function is in general complex, but for $4k\omega/\rho C_p U_o^2 \ll 1$, U_o is almost imaginary, and Merk (15) has pointed out that equation [26] can be expressed in terms of Fresnel integrals. Equation [26] can be written as equation [28], where E_m and F_m are the real and imaginary parts of the term within the square brackets. The terms E_m and F_m have been evaluated by Merk (15) and are plotted in figure 60.

$$\frac{q}{Q} = T_m \frac{\bar{U}}{U_o} = (E_m + F_m) \frac{\bar{U}}{U_o} \quad [28]$$

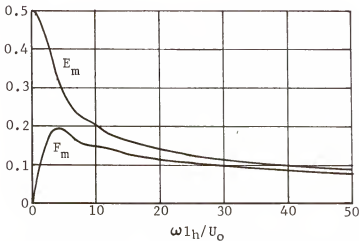


Figure 60. Real and imaginary parts of the function T_m for a flat ribbon heater, after Merk (15).

The fluctuating heat transfer, using equation [25], was calculated to be 485 watts. For a value of $\omega l_h/U_o = 5.56$, figure 60 gives $E_m = 0.275$ and $F_m = 0.18$. The amplitude of the function T_m is $|T_m| = 0.329$. Using equation [28] with $Q = 5Q_8 = 1187$ watts gives a calculated value of 197 watts for the fluctuating heat transfer. The phase lag between q and \bar{u}_1 was calculated to be -33° .

Comparing the two values of q , we see that they differ by 59 percent. Furthermore, a phase angle of -33° gives a small component of q in the direction of p_{av} (see the vector diagram, figure 58). However, testing has shown that the system was driven strongly. Thus, we can conclude that Carrier's equation underestimates the fluctuating heat transfer for the conditions of the 1200 watt Rijke test point. The most probable reason for underestimating q is that small perturbation theory simply does not hold at this power level.

If we accept $q = 485$ watts as a good estimate of the fluctuating heat transfer, a value of $|T_m| = 0.41$ would be required to produce the same value using [28]. This implies that Ψ_q is smaller than -33° . It is interesting to note that if $\omega l_h/U_o$ were reduced by 25%, resulting values of E_m and F_m would give $|T_m| = 0.41$ and the phase angle would be reduced to approximately -26° . This exercise indicates that the assumption of a small lag between q and \bar{u} , made earlier, is reasonable.

The efficiency of the thermoacoustic transduction process can be estimated from data contained in this section. If this efficiency is defined as the ratio of the acoustic power to the fluctuating heat transfer, then it can be calculated using equation [29]. The acoustic power

$$\eta_{t.a.} = \frac{q_a}{q} = \frac{(I_{s2} + I_{s5}) \pi D^2/4}{q} \quad [29]$$

contained in the fluid between planes of fittings 2 and 5 is given as the sum of intensities for those stations multiplied by the flow cross sectional area. Using data from Table 15 and $q = 485$ watts, $\eta_{t.a.} = 1.68\%$ Kerwin (13) estimated an order of magnitude value for $\eta_{t.a.} = 1\%$ using Lahmann's data (27).

Another result of the test program requiring further discussion is the relationship between the Rijke and Sondhauss types of instability. Historically, investigators have been treating Rijke and Sondhauss thermoacoustic instabilities separately. However, in this investigation, test 26 demonstrated that both Rijke and Sondhauss modes of thermoacoustic instability can be made to occur within the same device and at the same heater power level just by changing inlet end conditions. A comparison of both types of instability shows that a steep temperature gradient existed in the vicinity of the heater and that the location of the heater was important to the maintenance of oscillations for both cases. As in the Rijke device the acoustic variables respond as they would in a lossless, sourceless closed-open pipe with modification occurring in the vicinity of the heater. The response of the Sondhauss device to input power also parallels the Rijke device. Considering all of the evidence it can be concluded that both types of thermoacoustic instability are really one and the same phenomenon.

The differences between Rijke and Sondhauss instability are due to geometrical differences, that is, the Sondhauss device has its upstream end blocked. This causes the temperature gradient in the Sondhauss device to be set up in a different manner as discussed previously. The frequency of the resulting sound output corresponds to the fundamental mode for an open-open pipe in the case of the Rijke device and a closed-open pipe in the case of the Sondhauss device.

Conclusions

1. A gaseous system containing a heat source is capable of producing sound provided that conditions are established to promote thermoacoustic transduction and that the heat source is located in a position where the fluctuating heat transfer and pressure are positively correlated over a cycle of oscillation. Thermoacoustic transduction is promoted when a steep gas temperature gradient is established which allows interaction between the fluctuating thermal and acoustic energy modes with a subsequent energy transfer.
2. It has been experimentally shown that both Rijke and Sondhauss modes of thermoacoustic instability can occur in the same device, operating at the same power level, simply by changing inlet end conditions. Therefore, these two types of instability which have been historically treated as distinct, are really one and the same phenomenon.
3. Non-linear behavior in the sound output of both Rijke and Sondhauss devices was observed as heater power was progressively increased. In terms of sound pressure level, both systems were found to saturate above certain power levels. The Rijke device saturated above 1400 watts, whereas the Sondhauss device became saturated above 800 watts. These values are not absolute but depend upon the geometry and other operating conditions. However, the general trend should be common to all devices.
4. The free convection configuration of the Rijke device was found to be the most efficient in terms of sound output. Any attempts to decrease or to add to the free convection flow resulted in a reduced sound output.

5. The Rijke device was found to be unstable over a very narrow range of inlet velocities. Lower velocity limits converged upon values between 0.5 and 0.75 ft/sec for all power levels. Upper limits were found to be 3.93, 5.12 and 5.67 ft/sec, respectively for 1000, 1200 and 1400 watts of heater power. The specific values are relative to the configuration investigated but the trends are general.
6. Air movements were detected throughout the entire region above the heater plane in the Sondhauss device. It is hypothesized that free convective cells were formed within the Sondhauss device although there was no net through flow. A toroidal flow pattern was found to exist at the exit plane. An inwardly directed flow was detected at the tube periphery while the central core flowed in the outward direction. The toroidal flow pattern did not persist more than a 4 or 5 inches into the tube.
7. The hot-wire anemometer provides an excellent tool for exploring the acoustic field within a thermoacoustic device.

Recommendations

1. A constant current anemometer should be used to explore the fluctuating temperature field in the vicinity of the heat source for both the Sondhauss and Rijke devices. The resulting information would be extremely useful in the study of thermoacoustic transduction.
2. The Sondhauss device should be explored more completely with a hot-wire probe to describe the existing flow patterns. This information would then prove or disprove the hypothesized existence of cellular

flow patterns within the Sondhauss device.

3. Heat loss measurements, as originally planned for this study, should be made for both the Rijke and Sondhauss devices. Heat loss data along with fluctuating and steady gas temperature measurements would allow the determination of thermoacoustic efficiency.

APPENDICES

APPENDIX A
MEASUREMENT UNCERTAINTY THEORY

All measurements have measurement errors. These errors are the differences between the measurements and the true value defined by the National Bureau of Standards (NBS). Uncertainty is the maximum error which one might reasonably expect. It is a measure of accuracy, i.e., the closeness of the measurement to the true value.

Measurement error has two components: a fixed error and a random error. The random error is seen in repeated measurements. The measurements do not agree exactly, and they are not expected to. There are always numerous small effects which cause the disagreements. The variation between repeated measurements is called precision error (figure A-1). We use the standard deviation (σ) as a measure of the precision error. A large standard deviation means large scatter in the measurements. The statistic, s , is calculated to estimate the precision error and is called the precision index

$$s = \sqrt{\frac{\sum_{i=1}^N (x_i - \bar{x})^2}{N-1}} \quad [A-1]$$

where N is the number of measurements we have made and \bar{x} is the average value of the measurement.

The second component, bias, is the constant or systematic error. In repeated measurements, each measurement has the same bias (figure A-2). The bias cannot be determined unless the measurements are compared with the true value of the quantity measured. As the true value is almost

unknown (and unknowable), the bias is also unknown. We must rely on the best available information and engineering judgement to obtain an estimate of the upper limit or bound on the bias.

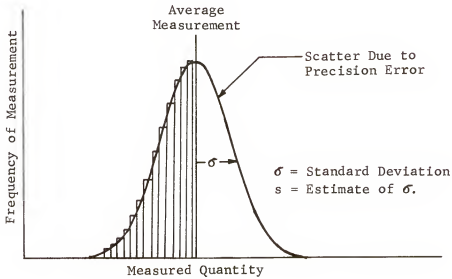


Figure A-1. Precision error.

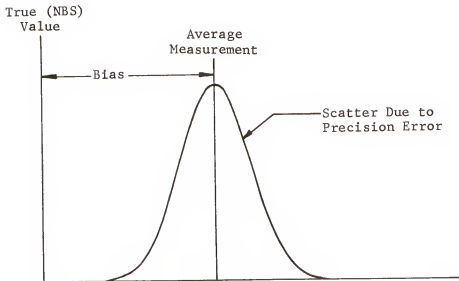


Figure A-2. Bias error.

Bias may be categorized into four classes: large known biases, small known biases, large unknown biases and small unknown biases. The large known biases are eliminated by comparing the instrument to a standard instrument and obtaining a correction. This is called calibration. Small known biases may or may not be corrected depending on the difficulty of the correction and the magnitude of the bias.

The unknown biases are not correctable. That is, we know that they may exist but we do not know the sign or magnitude of the bias. Small unknown biases stem from errors introduced from the hierarchy of calibrations that relate the NBS standard to the working instrument.

Every effort must be made to eliminate all large unknown biases. The introduction of such errors converts the controlled measurement process into an uncontrolled worthless effort. Large unknown biases usually come from human errors in data processing, incorrect handling and installation of instrumentation, and unexpected environmental disturbances. It must be assumed that in a well controlled measurement process there are no large unknown biases.

Propagation of Error

There are many parameters that cannot be measured directly. For example, the mass flow rate of a gas can be calculated from the measurement of orifice upstream pressure, temperature and differential pressure. The error in the measurements is propagated to the parameter through the function. The effect of the propagation may be approximated using Taylor series methods or as is sometimes called the "method of partial derivatives". See Reference(34) for a derivation of this method. According to this method, the error in a calculated value may be approximated as:

$$\epsilon_F = \sqrt{\left(\frac{\partial F}{\partial X_1}\right)^2 \epsilon_{X_1}^2 + \left(\frac{\partial F}{\partial X_2}\right)^2 \epsilon_{X_2}^2 + \dots + \left(\frac{\partial F}{\partial X_n}\right)^2 \epsilon_{X_n}^2} \quad [A-2]$$

where F is the calculated function, X_1, X_2, \dots, X_n are the variables used in calculating the function, $\frac{\partial F}{\partial X_1}, \dots, \frac{\partial F}{\partial X_n}$ are the partial derivatives of the calculated function with respect to the variables X_1, X_2, \dots, X_n , $\epsilon_1, \epsilon_2, \dots, \epsilon_n$ are the estimated errors in measurement of the variables X_1, X_2, \dots, X_n , ϵ_F is the estimated error in the calculated function due to the errors in the measurement of the variables X_1, X_2, \dots, X_n .

In the normal situation, precision errors (S_{X_n}) and bias errors (B_{X_n}) are known for the measurement of each X_n . The estimated bias limit (B_F) and precision error (S_F) are calculated for the function by successively applying equation [A-2].

Uncertainty

For simplicity and for comparisons, the need exists for a single number to express a reasonable limit for error, some combination of bias and precision. It is impossible to define a rigorous statistic because the bias is an upper limit based on judgement which has unknown characteristics. Any function of these two numbers must be a hybrid combination of an unknown quantity (bias) and a statistic (precision). However, the need for a single number to measure error is so great that we are forced to adopt an arbitrary standard. The one most widely used is the bias limit plus twice the precision error index. This method is recognized and recommended by the National Bureau of Standard and has been widely used in industry.

Uncertainty (figure A-3) is centered about the measurement and is

defined herein as:

$$\Omega = \pm (B + 2S).$$

Since S is an estimate of the standard deviation (σ), equation [A-3] can be expressed as

$$\Omega = \pm (B + 2\sigma). \quad [A-3]$$

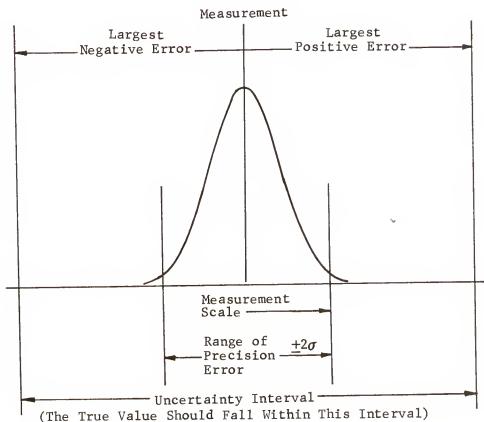


Figure A-3. Measurement uncertainty.

APPENDIX B

MEASUREMENT UNCERTAINTY ANALYSIS

In this appendix, analyses of the uncertainty in the acoustic, heater surface and velocity measurements are made. These analyses are rather lengthy and were omitted from the main body of this dissertation. However, the numerical evaluation of these measurement uncertainties are included in the appropriate sections of Chapter III. The last section of this appendix contains a table of the bias and precision errors for all instruments used in this program.

Acoustic Measurement

An estimate of the uncertainty in measuring the sound pressure and frequency are discussed in this section. With reference to figure [9] , this concerns the voltage signal path from microphone 1 to the GR-1900A Wave Analyzer and simultaneously to the CMC Preset Counter. Since the probe tube frequency response calibration involved the use of the B&K Wave Analyzer, it too must be included in the analysis. Both the Hewlett-Packard Oscilloscope and Level Recorder are excluded because they were only used to monitor data.

Equation [9] provides the functional relationship which determines the propagation of error from the individual measurements to the desired result, the sound pressure level (SPL) in decibel units. The effect of the propagation may be approximated using the "method of partial derivatives", equation [A-2] which is discussed in Appendix A. Equation [A-2] must be written and evaluated for both the bias error

limit (B) and precision error (σ).

$$B_{SPL} = \pm \sqrt{\left(\frac{\partial(SPL)}{\partial s_m} B_{s_m}\right)^2 + \left(\frac{\partial(SPL)}{\partial(SPV)} B_{SPV}\right)^2 + \left(\frac{\partial(SPL)}{\partial \Delta_f} B_{\Delta_f}\right)^2 + \left(\frac{\partial(SPL)}{\partial \Delta_{amb}} B_{\Delta_{amb}}\right)^2}$$

$$\sigma_{SPL} = \pm \sqrt{\left(\frac{\partial(SPL)}{\partial s_m} \sigma_{s_m}\right)^2 + \left(\frac{\partial(SPL)}{\partial(SPV)} \sigma_{SPV}\right)^2 + \left(\frac{\partial(SPL)}{\partial \Delta_f} \sigma_{\Delta_f}\right)^2 + \left(\frac{\partial(SPL)}{\partial \Delta_{amb}} \sigma_{\Delta_{amb}}\right)^2}$$

The partial derivatives are evaluated using equation [9], giving the working form of the equations for B_{SPL} and σ_{SPL} .

$$B_{SPL} = \pm \sqrt{B_{S_m}^2 + \left(\frac{20}{SPV} \log_{10} e\right)^2 B_{SPV}^2 + F_{\Delta_f}^2 + B_{\Delta_{amb}}^2} \quad [B-1]$$

$$\sigma_{SPL} = \pm \sqrt{\sigma_{S_m}^2 + \left(\frac{20}{SPV} \log_{10} e\right)^2 \sigma_{SPV}^2 + \sigma_{\Delta_f}^2 + \sigma_{\Delta_{amb}}^2} \quad [B-2]$$

The bias error limit B_{SPL} and precision error σ_{SPL} are combined to give the uncertainty Ω_{SPL} as explained in Appendix A.

$$\Omega_{SPL} = \pm \left(B_{SPL} + 2 \sigma_{SPL} \right) \quad [B-3]$$

B_{s_m} and σ_{s_m}

These errors were introduced by the uncertainty of the pistonphone's sound pressure level during the sensitivity calibration. The entire system, excluding the effects of the probe tube, were calibrated at one sound pressure and frequency. From data given in Table B-1,

$$B_{s_m} = \pm 0.1 \text{ db}$$

$$\sigma_{s_m} = \pm 0.05 \text{ db}$$

B_{SPV} and σ_{SPV}

These errors are due to reading the sound pressure voltage signal on the GR-1900A Wave Analyzer. Full scale deflection of 300 and 1000 mv were set on the GR-1900A for the readings, thus from Table B-1,

$$B_{SPV} = \pm 0.02 \text{ (SPV) volts}$$

$$\sigma_{SPV} = \pm 0.01 \text{ volts for 1000 mv full scale}$$

$$\pm 0.003 \text{ volts for 300 mv full scale}$$

B_{Δ_f} and σ_{Δ_f}

These errors were introduced as a result of the probe tube calibration and involve errors from several sources. First, the B&K Wave Analyzer was used to read sound pressure and its errors must be included. However, since identical measurements were made and subtracted to give Δ_f , bias errors cancel and only precision errors remain. Next, since a microphone was used, the sound pressure readings making up Δ_f are subjected to a precision error (bias errors again cancel due to differencing) of the microphone calibration. Finally, a precision error in the frequency measurement (bias error negligible) gives rise to a precision error in the evaluation of a value of Δ_f from figure [22] at a given frequency. All of the constituent errors as described above and values given in Table B-1 must be root-sum-squared to give the total value of B_{Δ_f} and σ_{Δ_f} .

$$B_{\Delta_f} \approx 0 \text{ (negligible)}$$

$$\sigma_{\Delta_f} = \pm \sqrt{(0.09)^2 + (0.05)^2 + \left[\frac{\partial \Delta_f}{\partial f} (0.033) \right]^2}$$

The term $\partial \Delta_f / \partial f$ is evaluated from the data of figure

$B_{\Delta_{amb}}$ and $\sigma_{\Delta_{amb}}$

These errors are due to making ambient pressure corrections to the microphone sensitivity using a special B&K barometer, calibrated in db.

$$B_{\Delta_{amb}} \approx 0 \text{ (negligible)}$$

$$\sigma_{\Delta_{amb}} = \pm 0.025 \text{ db}$$

An evaluation of B_{SPL} , σ_{SPL} and Ω_{SPL} is discussed in Chapter III using the various values of the component bias and precision errors as given in this section.

Heater Surface Temperature Measurement

Following the methods presented in Appendix A, the propagation of error from measurements is again determined by using the "method of partial derivatives". Bias and precision errors can be calculated from equations [B-4] and [B-4a] which were derived by using equations [A-2] and [11] .

$$B_{T_h} = \pm \sqrt{(B_{T'_h})^2 + (B_{\Delta T})^2} \quad [B-4]$$

$$\sigma_{T_h} = \pm \sqrt{(\sigma_{T'_h})^2 + (\sigma_{\Delta T})^2} \quad [B-4a]$$

$B_{T'_h}$ and $\sigma_{T'_h}$

These errors were introduced by the uncertainty associated with the IRCON Indicator Unit. Their values are given in Table B-1. For IRCON range switch in position 1,

$$B_{T'_h} = \pm 6^{\circ}\text{F}$$

$$\sigma_{T'_h} = \pm 1.07^{\circ}\text{F}$$

and for range switch in position 2,

$$B_{T'_h} = \pm 10^{\circ}\text{F}$$

$$\sigma_{T'_h} = \pm 1.8^{\circ}\text{F}$$

B ΔT and $\sigma_{\Delta T}$

These error sources are somewhat complex and involve errors associated with the calibration process, instruments used and method of measuring the percentage of reticle area filled by the target. The spread in calibration points of figure[24] from the mean value line is interpreted as a $\pm 3\sigma$ precision error. Although some bias error is undoubtedly present, it is assumed to be negligible. The error band is due to such effects as repeatability, variations in heater configuration, inaccuracies in determining the amount of metal area in the reticle, second order effects in operating the heaters over a range of power levels, unknown errors in values for emissivity from reference (29), etc. An additional error was encountered when reading the calibration curve in that an uncertainty in calculating α , the percent of reticle filled by target, gives rise to an additional uncertainty as shown in figure B-1. The symbol $\sigma'_{\Delta T}$ is the precision error in obtaining a ΔT correction and is 1/3 of the error magnitude in figure[24]. K_{α} is the slope of the $\sigma'_{\Delta T}$ versus α curve.

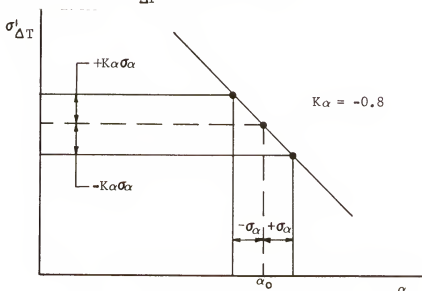


Figure B-1. Precision error in ΔT correction.

A precision error of $\pm 1.0\%$ was estimated for the process of calculating the percent of reticle area filled by target with an assumed bias error of zero. Bias and precision errors for both the IRCON and L&N Optical Pyrometer are listed in Table B-1. In order to obtain $B_{\Delta T}$ and $\sigma_{\Delta T}$, the component errors must be root-sum-squared as shown below. When the IRCON range switch is in position 1,

$$B_{\Delta T} = \pm 6.7^{\circ}\text{F}$$

$$\sigma_{\Delta T} = \pm \sqrt{(\sigma'_{\Delta T})^2 + (-0.8 \times 1.0)^2 + (2.5)^2 + (1.07)^2}$$

and for range 2,

$$B_{\Delta T} = \pm 10^{\circ}\text{F and}$$

$$\sigma_{\Delta T} = \pm \sqrt{(\sigma'_{\Delta T})^2 + (-0.8 \times 1.0)^2 + (2.5)^2 + (1.8)^2}$$

Velocity Measurement

An analysis of the uncertainty involved in measuring the time mean and fluctuating components of velocity using hot-wire anemometry is considered here. The analysis is somewhat complex due to the long chain of errors that must be considered.

Time mean velocity

Two main sources of error contributed to the uncertainty in the time mean velocity measurement. The first was due to combined errors in obtaining the static calibration curve while the second was due to the operational techniques involved in maintaining the overheat ratio constant in an attempt to compensate for temperature non-uniformity in the test apparatus. In keeping the overheat ratio constant, local values of ambient resistance R_g at some temperature, T_g , must be measured and then

multiplied by one plus the over heat ratio to give the operating resistance R_w . The operating resistance was then set on the CTA by means of decade switches provided.

The contribution to measurement uncertainty from the static calibration curve was due to errors involved in determining U_o and V , the time mean velocity and DC bridge voltage. The time mean velocity was calculated from primary measurements as given by equation [19].

Bias and precision errors that were propagated in calculating U are designated B_{U_1} and σ_{U_1} . Bias and precision errors associated with measuring V on the Doric microvoltmeter are designated B_{U_2} and σ_{U_2} . Equation [19] can be rewritten as [B-5] by considering $(\tilde{v}/v)(8R/\pi D^2) = C_c$ a constant. This is true once a hot-wire probe and laminar flow tube are specified.

$$U_o = C_c \frac{\dot{m} T}{p} \quad [B-5]$$

Using equation [B-4] as the function F in equation [A-2] of Appendix A yields [B-5a], the error propagation in calculating U_o .

$$\epsilon_{U_1} = \pm \sqrt{\left[\left(\frac{C_c T}{p} \right) \epsilon_{\dot{m}} \right]^2 + \left[\frac{C_c \dot{m}}{p} \epsilon_T \right]^2 + \left[\frac{-C_c \dot{m} T}{p^2} \epsilon_p \right]^2} \quad [B-5a]$$

In equation [B-5a], $\epsilon_{\dot{m}}$ symbolically represents bias and precision errors involved in measuring the hot-wire calibration air flow rate. The uncertainty in measuring \dot{m} is $\pm 2\%$ of reading over the entire range of calibration. The estimated bias error limit is $B_{\dot{m}} = \pm 1\%$ of reading and the precision error is $\sigma_{\dot{m}} = \pm 0.5\%$ of reading. The error term ϵ_T represents the bias and precision errors associated with the gas temperature measurement at the block. From Table 6, at a calibra-

tion air temperature of 70°F, $B_T = \pm 2.07^\circ\text{F}$ and $\sigma_T = \pm 0.29^\circ\text{F}$. The term ϵ_p represents the bias and precision errors associated with the ambient pressure measurement at the exit of the laminar flow tube. Ambient pressure was obtained from the P&WA weather station which gives readings accurate to within an uncertainty of ± 0.005 in. Hg. It has been assumed that the bias error is negligible thus the precision error is taken as $\epsilon_p = \pm 0.0025$ in. Hg.

Errors in the operational procedure of keeping the hot-wire overheat ratio constant can be evaluated analytically. Starting with equation [14] and substituting V^2/R_w for I^2R and evaluating A_w of the resulting expression for $U_o = 0$, letting $V = V_o$ gives equation [B-6] in terms of U_o . U_o is restricted to values greater than U^* .

$$U_o = \left[\frac{V^2 - V_o^2}{B_w(R_w^2 - R_w R_g)} \right]^2 \quad [\text{B-6}]$$

The propagation of errors in the measurement of V , V_o , R_w and R_g to the uncertainty in U_o is found by utilizing equation [B-6] as the function F in equation [A-2]. Equation [B-7] gives the error contribution due to maintaining a constant overheat ratio during hot-wire probing.

$$\epsilon_{U_3} = \pm \sqrt{(4V\sqrt{U_o}\epsilon_V)^2 + (4V_o\sqrt{U_o}\epsilon_{V_o})^2 + \left[\frac{2U_o(2R_w - R_g)}{(R_w^2 - R_w R_g)} \epsilon_{R_w} \right]^2 + \left[\frac{2U_o R_w}{(R_w^2 - R_w R_g)} \epsilon_{R_g} \right]^2} \quad [\text{B-7}]$$

The error term ϵ_{U_3} symbolically represents the bias and precision errors B_{U_3} and σ_{U_3} respectively. In equation [B-7] ϵ_V and ϵ_{V_o} represent errors associated with reading voltages on the Doric micro-voltmeter¹. The errors ϵ_{R_g} and ϵ_{R_w} are associated with measuring ambient and operating resistances using the DISA 55A01 CTA. These

errors can be found in Table B-1. Thus, the total bias and precision errors associated with measuring the time velocity are given by equation [B-8] and [B-9] and the resulting uncertainty by equation [B-10] .

$$B_{U_o} = \pm \sqrt{B_{U_1}^2 + B_{U_2}^2 + B_{U_3}^2} \quad [B-8]$$

$$\sigma_{U_o} = \pm \sqrt{\sigma_{U_1}^2 + \sigma_{U_2}^2 + \sigma_{U_3}^2} \quad [B-9]$$

$$\Omega_{U_o} = \pm (B_U + 2 \sigma_U) \quad [B-10]$$

Fluctuating velocity

The uncertainty in the measurement of fluctuating velocity was due to errors which were inherent in developing the sensitivity curve plus errors in reading the RMS AC bridge voltage on the DISA CTA. In order to simplify the analysis, it will be assumed that $U_o > U^*$ and that equation [B-6] describes the physical situation existing. Solving for V and differentiating V with respect to U_o gives the sensitivity, S as in equation [B-11] .

$$S_{hw} = \frac{dV}{dU_o} = \frac{B_w(R_w^2 - R_w R_g)}{4 \left[V_o U_o + B_w(R_w^2 - R_w R_g) U_o^{3/2} \right]^{1/2}} \quad [B-11]$$

The fluctuating velocity is calculated from equation [B-12] where B_w was replaced using

$$\bar{u} = \frac{V_{AC}}{S_{hw}} = \frac{4 V_{AC} U_o V}{V^2 - V_o^2} \quad [B-12]$$

¹All DC bridge voltages for the 55F33 (miniature) probes were read from the Doric microvoltmeter, whereas as Esterline-Angus strip chart was used for the 55A75 (high temperature) probe. The strip chart recorder was used during a brief period when the Doric microvoltmeter was unavailable to the research program.

equation [B-6] . The propagation of error from measurements of U_o , V_{AC} , V_o , and V to the fluctuating velocity \bar{u} can be calculated by letting equation [B-12] represent the function F in equation [A-2] of Appendix A. In equation [B-13], $\epsilon_{\bar{u}}$ symbolically represents the bias and precision errors, $B_{\bar{u}}$ and $\sigma_{\bar{u}}$.

$$\epsilon_{\bar{u}} = \pm \left[\left(\frac{4 V_{AC} V}{V^2 - V_o^2} \epsilon_{U_o} \right)^2 + \left(\frac{4 V_o V}{V^2 - V_o^2} \epsilon_{V_{AC}} \right)^2 + \left(\frac{8 V_{AC} U_o V V_o}{(V^2 - V_o^2)^2} \epsilon_{V_o} \right)^2 + \left(\frac{-4 V_{AC} U_o V_o^2 + V^2}{(V^2 - V_o^2)^2} \epsilon_V \right)^2 \right]^{1/2} \quad [B-13]$$

The error term ϵ_{U_o} represents the error in measuring the time mean velocity and is evaluated from equations [B-8] and [B-9] . $\epsilon_{V_{AC}}$ is the error involved in measuring the RMS AC voltage from the DISA CTA. See Table B-1 for bias and precision error estimates. As mentioned previously ϵ_{V_o} and ϵ_V are errors introduced in reading the DC bridge voltages. The uncertainty is given by equation [B-14] .

$$\Omega_{\bar{u}} = \pm (B_{\bar{u}} + 2 \sigma_{\bar{u}}) \quad [B-14]$$

Instrument Bias and Precision Errors

Table B-1 contains a list of instruments used in the experimental program along with assigned bias and precision error estimates. The error values were obtained from P&WA Instrumentation Standards or estimated from the manufacturers data.

Table B-1. Instrument Bias and Precision Errors

Instrument Identification	Bias Error Limit	Precision Error One Standard Deviation (σ)
Computer Measurements Co., Model 702 A, Preset Counter	Negligible	± 0.033 counts
Esterline Angus Strip Chart	$\pm 0.25\%$ full scale	$\pm 0.125\%$ full scale
Doric Integrating Microvolt- meter, DS 100	10 mv range: $\pm (0.02\% \text{ reading} + 2.3 \mu\text{v})$ 100 mv range: $\pm (0.01\% \text{ reading} + 10 \mu\text{v})$ 1 volt range: $\pm (0.01\% \text{ reading} + 100 \mu\text{v})$ 10 volt range: $\pm (0.01\% \text{ reading} + 1 \text{ mv})$	10 mv range: $\pm (0.0083\% \text{ reading} + 1.1 \mu\text{v})$ 100 mv range: $\pm (0.005\% \text{ reading} + 10.3 \mu\text{v})$ 1 volt range: $\pm (0.005\% \text{ reading} + 100 \mu\text{v})$ 10 volt range: $\pm (0.005\% \text{ reading} + 1 \text{ mv})$
Hewlett-Packard, 132A Dual Beam Oscilloscope	Voltage: $\pm 2\%$ reading Phase: $\pm 2^\circ$ degrees	Voltage: $\pm 1\%$ reading Phase: $\pm 1^\circ$ degree
Bruel & Kjaer Audio Frequency Spectrometer, Type 2112	± 0.3 db	± 0.09 db
General Radio Wave Analyzer, Type 1900A	$\pm 2\%$ reading	$\pm 1\%$ full scale
Bruel & Kjaer Pistonphone Type 4220	± 0.1 db	± 0.05 db
Leeds & Northrup Co. Optical Pyrometer, Type 8622	$\pm 3^\circ\text{F}$	$\pm 2.5^\circ\text{F}$
IRCON Infrared Radiation Thermometer, Model 640	$\pm 6^\circ\text{F}$ for range 1 $\pm 10^\circ\text{F}$ for range 2	$\pm 1.07^\circ\text{F}$ for range 1 $\pm 1.8^\circ\text{F}$ for range 2
DISA 55A01 Constant Temperature Anemometer	RMS Indicator: $\pm 1\%$ reading Cold Resistance Measurement: Negligible Operating Resistance: Negligible	RMS Indicator: $\pm 1/3\%$ reading Cold Resistance Measurement: $\pm 0.167\%$ reading Operating Resistance: $\pm 0.0333\%$ reading
Weston Instruments Div., Wattmeter, Model 310	± 12.5 watts for 0-5000 watt scale	± 2.5 watts for 0-5000 watt scale
Weston Instruments Div., AC Voltmeter, Model 903	± 1.5 volts for 0-150v scale	± 0.075 volts for 0-150v scale
Rubicon Instruments, Wheatstone Bridge, Model 1052	$\pm 0.05\%$ reading	$\pm 0.033\%$ reading
Barton Instruments Corp. 0-100 in. H_2O Pressure Gage	± 0.6 inches H_2O	± 0.3 inches H_2O
Meriam Instruments Co., 0-15 in. H_2O U-tube Manometer	Negligible	± 0.025 inches

APPENDIX C
TABULATED TEST DATA

TABLE C-1. MICROPHONE DATA REDUCTION FOR
RIJKE CONFIGURATION, TEST NO.12

FITTING NUMBER	FREQUENCY (HERTZ)	SOUND PRESSURE LEVEL (DB)	SOUND PRESSURE (LB/SQ IN)
1	218.10	133.61	0.1376E-01
2	218.20	143.28	0.4187E-01
3	218.10	143.74	0.4417E-01
4	218.00	144.29	0.4704E-01
5	218.10	145.66	0.5507E-01
6	218.10	146.43	0.6023E-01
7	218.20	147.00	0.6425E-01
8	218.20	147.00	0.6425E-01
9	218.20	146.01	0.5736E-01
10	218.20	142.66	0.3901E-01
11	218.20	129.98	0.9064E-02

TABLE C-2. MICROPHONE DATA REDUCTION FOR
RIJKE CONFIGURATION, TEST NO.1

FITTING NUMBER	FREQUENCY (HERTZ)	SOUND PRESSURE LEVEL (DB)	SOUND PRESSURE (LB/SQ IN)
1	217.8	141.20	0.3440E-01
2	217.60	145.19	0.5219E-01
3	217.70	146.68	0.6195E-01
4	217.60	147.52	0.6825E-01
5	217.40	147.88	0.7112E-01
6	217.30	148.49	0.7628E-01
7	217.20	148.81	0.7915E-01
8	217.10	148.68	0.7800E-01
9	217.00	147.66	0.6939E-01
10	217.00	144.90	0.5047E-01
11	216.70	132.53	0.1215E-01

TABLE C-3. MICROPHONE DATA REDUCTION FOR
RIJKE CONFIGURATION, TEST NO.2

FITTING NUMBER	FREQUENCY (HERTZ)	SOUND PRESSURE LEVEL (DB)	SOUND PRESSURE (LB/SQ IN)
1	222.3	143.50	0.4300E-01
2	222.10	148.66	0.7779E-01
3	222.10	148.59	0.7717E-01
4	222.10	148.79	0.7904E-01
5	221.90	150.80	0.9957E-01
6	222.40	151.02	0.1020E 00
7	222.10	151.12	0.1033E 00
8	221.60	151.01	0.1020E 00
9	222.10	150.36	0.9460E-01
10	222.20	147.39	0.6721E-01
11	222.20	135.79	0.1767E-01

TABLE C-4. MICROPHONE DATA REDUCTION FOR
RIJKE CONFIGURATION, TEST NO.3

FITTING NUMBER	FREQUENCY (HERTZ)	SOUND PRESSURE LEVEL (DB)	SOUND PRESSURE (LB/SQ IN)
1	226.2	144.30	0.4680E-01
2	225.60	148.46	0.7602E-01
3	225.70	149.27	0.8351E-01
4	225.80	149.57	0.8640E-01
5	225.50	150.29	0.9388E-01
6	225.60	150.65	0.9791E-01
7	225.60	150.86	0.1002E 00
8	225.70	150.86	0.1002E 00
9	225.70	150.07	0.9158E-01
10	225.40	147.18	0.6565E-01
11	225.20	136.04	0.1919E-01

TABLE C-5. MICROPHONE DATA REDUCTION FOR
RIJKE CONFIGURATION, TEST NO.4

FITTING NUMBER	FREQUENCY (HERTZ)	SOUND PRESSURE LEVEL (DB)	SOUND PRESSURE (LB/SQ IN)
1	229.80	144.42	0.4774E-01
2	227.80	148.57	0.7704E-01
3	229.90	147.97	0.7190E-01
4	230.20	148.18	0.7363E-01
5	230.20	149.67	0.8744E-01
6	228.90	150.79	0.9949E-01
7	229.80	151.04	0.1023E 00
8	229.90	150.99	0.1018E 00
9	228.20	149.78	0.8855E-01
10	228.90	147.02	0.6441E-01
11	229.60	136.56	0.1932E-01

TABLE C-6. MICROPHONE DATA REDUCTION FOR
RIJKE CONFIGURATION, TEST NO.17

FITTING NUMBER	FREQUENCY (HERTZ)	SOUND PRESSURE LEVEL (DB)	SOUND PRESSURE (LB/SQ IN)
1	221.50	150.62	0.9748E-01
2	221.60	150.51	0.9634E-01
3	100.00	0.00	0.2870E-08
4	125.00	0.00	0.2870E-08
5	150.00	0.00	0.2870E-08
6	175.00	79.44	0.2692E-04
7	185.00	86.70	0.6212E-04
8	190.00	91.01	0.1020E-03
9	196.00	98.49	0.2412E-03
10	200.00	105.61	0.5478E-03
11	205.00	112.74	0.1245E-02
12	210.00	124.68	0.4924E-02
13	214.00	135.54	0.1719E-01
14	214.80	139.98	0.2866E-01
15	215.50	142.40	0.3783E-01
16	216.40	145.09	0.5161E-01
17	217.10	146.68	0.6194E-01
18	218.00	148.42	0.7572E-01
19	218.80	149.30	0.8376E-01
20	219.50	149.99	0.9066E-01
21	222.20	150.47	0.9589E-01
22	223.80	150.37	0.9478E-01
23	225.40	149.88	0.8953E-01
24	226.10	149.06	0.8151E-01
25	226.50	148.02	0.7233E-01
26	227.70	146.36	0.5972E-01
27	230.10	139.09	0.2585E-01
28	231.00	134.65	0.1551E-01
29	233.00	130.43	0.9544E-02
30	235.00	125.50	0.5407E-02
31	237.00	120.36	0.2992E-02
32	240.00	114.21	0.1474E-02
33	243.00	107.63	0.6915E-03
34	250.00	98.11	0.2308E-03
35	260.00	75.69	0.1747E-04
36	270.00	76.33	0.1881E-04
37	280.00	0.00	0.2870E-08
38	300.00	0.00	0.2870E-08
39	320.00	0.00	0.2870E-08
40	415.00	81.09	0.3255E-04
41	420.00	88.11	0.7304E-04
42	430.00	77.26	0.2094E-04
43	434.00	87.17	0.6553E-04
44	438.40	99.64	0.2756E-03
45	440.90	105.03	0.5123E-03
46	442.90	105.25	0.5258E-03
47	444.10	105.68	0.5523E-03
48	446.50	104.82	0.5001E-03
49	448.60	103.33	0.4215E-03
50	450.80	99.04	0.2570E-03
51	453.80	87.40	0.6730E-04
52	455.70	81.88	0.3565E-04
53	460.00	0.00	0.2870E-08

TABLE C-7. MICROPHONE DATA REDUCTION FOR
RIJKE CONFIGURATION, TEST NO.18

FITTING NUMBER	FREQUENCY (HERTZ)	SOUND PRESSURE LEVEL (DB)	SOUND PRESSURE (LB/SQ IN)
1	100.00	78.34	0.2373E-04
2	125.00	95.46	0.1702E-03
3	150.00	94.68	0.1556E-03
4	160.00	97.78	0.2222E-03
5	170.00	102.05	0.3637E-03
6	175.00	105.10	0.5165E-03
7	180.00	108.13	0.7324E-03
8	185.30	112.81	0.1255E-02
9	189.50	117.46	0.2143E-02
10	191.70	120.41	0.3010E-02
11	194.30	125.94	0.5690E-02
12	196.00	130.03	0.9115E-02
13	196.80	132.80	0.1254E-01
14	197.50	134.26	0.1482E-01
15	198.00	133.92	0.1426E-01
16	198.80	132.24	0.1175E-01
17	200.20	128.77	0.7884E-02
18	205.00	123.01	0.4060E-02
19	210.00	119.83	0.2817E-02
20	225.00	118.89	0.2528E-02
21	250.00	115.62	0.1733E-02
22	275.00	111.09	0.1028E-02
23	300.00	108.20	0.7382E-03
24	325.00	103.02	0.4063E-03
25	350.00	99.24	0.2630E-03
26	368.00	96.99	0.2029E-03
27	371.00	96.56	0.1932E-03
28	375.00	104.07	0.4588E-03
29	380.00	111.46	0.1074E-02
30	385.00	118.01	0.2284E-02
31	389.00	121.66	0.3474E-02
32	390.80	123.41	0.4252E-02
33	391.70	123.15	0.4126E-02
34	396.10	122.90	0.4009E-02
35	397.30	123.71	0.4400E-02
36	400.80	122.04	0.3632E-02
37	404.00	119.47	0.2701E-02
38	409.00	117.31	0.2106E-02
39	414.00	115.01	0.1615E-02
40	420.00	112.04	0.1149E-02
41	430.00	109.96	0.9041E-03
42	446.00	109.22	0.8300E-03
43	459.00	107.75	0.7012E-03

TABLE C-8. MICROPHONE DATA REDUCTION FOR
RIJKE CONFIGURATION, TEST NO.18

FITTING NUMBER	FREQUENCY (HERTZ)	SOUND PRESSURE LEVEL (DB)	SOUND PRESSURE (LB/SQ IN)
1	222.30	133.98	0.1435E-01
2	222.30	132.87	0.1263E-01
3	222.30	130.83	0.9991E-02
4	222.30	128.94	0.8039E-02
5	222.30	128.03	0.7235E-02
6	222.30	126.02	0.5742E-02
7	222.30	123.64	0.4364E-02
8	222.30	122.67	0.3904E-02
9	222.30	122.67	0.3904E-02

TABLE C-9. MICROPHONE DATA REDUCTION FOR
RIJKE CONFIGURATION, TEST NO.18

FITTING NUMBER	FREQUENCY (HERTZ)	SOUND PRESSURE LEVEL (DB)	SOUND PRESSURE (LB/SQ IN)
1	222.20	134.96	0.1607E-01
2	221.80	132.87	0.1263E-01
3	222.20	130.73	0.9876E-02
4	222.30	129.06	0.8153E-02
5	222.40	127.60	0.6890E-02
6	222.20	126.52	0.6086E-02
7	222.30	125.29	0.5282E-02
8	222.10	124.29	0.4708E-02
9	222.10	124.29	0.4708E-02
10	222.10	124.08	0.4593E-02
11	222.60	123.52	0.4306E-02
12	222.20	122.91	0.4014E-02
13	221.90	121.57	0.3441E-02
14	222.20	120.82	0.3154E-02

TABLE C-10. MICROPHONE DATA REDUCTION FOR
RIJKE CONFIGURATION, TEST NO.16

FITTING NUMNER	FREQUENCY (HERTZ)	SOUND PRESSURE LEVEL (DB)	SOUND PRESSURE (LB/SQ IN)
1	223.60	150.46	0.9572E-01
2	227.10	150.87	0.1003E 00
3	221.30	149.23	0.8314E-01
4	219.90	147.53	0.6831E-01
5	218.50	144.00	0.4552E-01

TABLE C-11. MICROPHONE DATA REDUCTION FOR
RIJKE CONFIGURATION, TEST NO.16

FITTING NUMNER	FREQUENCY (HERTZ)	SOUND PRESSURE LEVEL (DB)	SOUND PRESSURE (LB/SQ IN)
1	226.70	151.98	0.1140E 00
2	223.50	151.53	0.1082E 00
3	220.20	150.35	0.9451E-01
4	219.10	149.46	0.8537E-01
5	217.30	145.94	0.5689E-01

TABLE C-12. HOT-WIRE DATA REDUCTION FOR RIJKE
CONFIGURATION, TEST NO.1 ,FITTING 12

R (IN)	VDC (VOLTS)	VAC (MVOLTS)	U (FPS)	UBAR (FPS)	S (FPS/VOLT)
-1.6069	6.148	176.	2.938	1.131	6.42
-1.4769	6.090	368.	2.582	2.145	5.83
-0.6770	6.194	397.	3.244	2.712	6.83
0.0000	6.226	368.	3.467	2.593	7.04
0.5730	6.174	306.	3.109	2.040	6.66
1.3230	6.244	269.	3.596	1.919	7.13
1.5540	6.160	232.	3.016	1.517	6.54

TABLE C-13. HOT-WIRE DATA REDUCTION FOR RIJKE
CONFIGURATION, TEST NO.1 ,FITTING 13

R (IN)	VDC (VOLTS)	VAC (MVOLTS)	U (FPS)	UBAR (FPS)	S (FPS/VOLT)
-1.6389	5.890	159.	1.623	0.617	3.88
-1.5189	6.177	334.	3.129	2.235	6.69
-0.7190	6.196	389.	3.258	2.663	6.84
0.0000	6.212	349.	3.369	2.429	6.96
0.5309	6.192	327.	3.231	2.228	6.81
1.2809	6.214	347.	3.383	2.420	6.97
1.4309	6.227	265.	3.474	1.868	7.05
1.5399	6.080	265.	2.524	1.516	5.72

TABLE C-14. HOT-WIRE DATA REDUCTION FOR RIJKE
CONFIGURATION, TEST NO.2 ,FITTING 12

R (IN)	VDC (VOLTS)	VAC (MVOLTS)	U (FPS)	UBAR (FPS)	S (FPS/VOLT)
1.5540	6.550	275.	4.583	1.939	7.05
1.4230	6.530	296.	4.445	2.045	6.91
1.3230	6.550	296.	4.583	2.087	7.05
1.0730	6.590	300.	4.871	2.175	7.25
0.8230	6.490	292.	4.173	1.976	6.76
0.5730	6.580	301.	4.797	2.157	7.16
0.3230	6.570	314.	4.725	2.234	7.11
0.0000	6.590	321.	4.871	2.327	7.25
-0.1770	6.610	320.	5.019	2.395	7.48
-0.4270	6.570	321.	4.725	2.284	7.11
-0.6770	6.580	324.	4.797	2.322	7.16
-0.9270	6.470	350.	4.039	2.358	6.73
-1.1770	6.590	350.	4.871	2.537	7.25
-1.3770	6.620	355.	5.088	2.709	7.63
-1.4769	6.590	300.	4.871	2.175	7.25
-1.5769	6.620	317.	5.088	2.419	7.63
-1.6060	6.538	292.	4.500	2.032	6.96

TABLE C-15. HOT-WIRE DATA REDUCTION FOR RIJKE
CONFIGURATION, TEST NO.2 ,FITTING 13

R (IN)	VDC (VOLTS)	VAC (MVOLTS)	U (FPS)	UBAR (FPS)	S (FPS/VOLT)
1.4230	6.550	341.	4.583	2.405	7.05
1.3810	6.530	341.	4.445	2.356	6.91
1.2809	6.520	333.	4.377	2.284	6.86
1.0309	6.500	334.	4.241	2.268	6.79
0.7809	6.480	316.	4.106	2.133	6.75
0.5309	6.480	316.	4.106	2.133	6.75
0.2809	6.500	315.	4.241	2.139	6.79
0.0000	6.480	323.	4.106	2.180	6.75
-0.2190	6.480	325.	4.106	2.194	6.75
-0.4690	6.450	325.	3.904	2.184	6.72
-0.7190	6.450	332.	3.904	2.231	6.72
-0.9690	6.440	326.	3.837	2.188	6.71
-1.2190	6.440	328.	3.837	2.201	6.71
-1.4190	6.440	335.	3.837	2.248	6.71
-1.5189	6.420	300.	3.703	2.008	6.69
-1.6190	6.450	235.	3.904	1.579	6.72
-1.6369	6.470	251.	4.039	1.691	6.73

TABLE C-16. HOT-WIRE DATA REDUCTION FOR RIJKE
CONFIGURATION, TEST NO.3 ,FITTING 12

R (IN)	VDC (VOLTS)	VAC (MVOLTS)	U (FPS)	UBAR (FPS)	S (FPS/VOLT)
1.5130	6.405	282.	4.780	2.222	7.88
1.4230	6.397	308.	4.713	2.407	7.81
1.3230	6.379	310.	4.564	2.377	7.66
1.0730	6.358	305.	4.415	2.274	7.45
0.8230	6.344	300.	4.318	2.189	7.29
0.5730	6.347	306.	4.339	2.243	7.33
0.3230	6.347	310.	4.339	2.273	7.33
0.0729	6.345	315.	4.325	2.302	7.31
-0.1770	6.358	319.	4.415	2.379	7.45
-0.4270	6.358	325.	4.415	2.423	7.45
-0.6770	6.349	324.	4.353	2.383	7.35
-0.9270	6.369	330.	4.489	2.499	7.57
-1.1770	6.375	330.	4.533	2.518	7.63
-1.4270	6.385	308.	4.613	2.377	7.71
-1.5269	6.394	281.	4.688	2.189	7.79
-1.5769	6.369	282.	4.489	2.136	7.57

TABLE C-17. HOT-WIRE DATA REDUCTION FOR RIJKE
CONFIGURATION, TEST NO.3 ,FITTING 13

R (IN)	VDC (VOLTS)	VAC (MVOLTS)	U (FPS)	UBAR (FPS)	S (FPS/VOLT)
1.5455	6.368	286.	4.482	2.163	7.56
1.4260	6.357	322.	4.408	2.398	7.44
1.2809	6.372	321.	4.510	2.440	7.60
1.0309	6.363	315.	4.448	2.366	7.51
0.7809	6.361	323.	4.436	2.419	7.49
0.5309	6.349	322.	4.353	2.368	7.35
0.2809	6.345	321.	4.325	2.346	7.31
0.0309	6.348	320.	4.346	2.350	7.34
-0.2190	6.351	322.	4.367	2.376	7.37
-0.4690	6.362	316.	4.442	2.370	7.50
-0.7190	6.366	315.	4.468	2.376	7.54
-0.9690	6.362	319.	4.442	2.393	7.50
-1.2689	6.374	321.	4.525	2.446	7.62
-1.4690	6.397	311.	4.713	2.430	7.81
-1.5690	6.345	281.	4.325	2.054	7.31
-1.6190	6.381	266.	4.580	2.044	7.68
-1.6389	6.285	205.	3.892	1.481	7.22

TABLE C-18. HOT-WIRE DATA REDUCTION FOR RIJKE
CONFIGURATION, TEST NO.4 ,FITTING 12

R (IN)	VDC (VOLTS)	VAC (MVOLTS)	U (FPS)	UBAR (FPS)	S (FPS/VOLT)
1.5330	6.381	285.	4.580	2.190	7.68
1.4230	6.354	300.	4.388	2.223	7.41
1.3230	6.384	305.	4.605	2.351	7.71
1.0730	6.332	300.	4.232	2.153	7.17
0.8230	6.348	302.	4.346	2.218	7.34
0.5730	6.345	302.	4.325	2.207	7.31
0.3230	6.346	312.	4.332	2.284	7.32
0.0729	6.347	314.	4.339	2.302	7.33
-0.1770	6.330	315.	4.218	2.256	7.16
-0.4270	6.347	325.	4.339	2.383	7.33
-0.6770	6.342	326.	4.303	2.372	7.27
-0.9270	6.348	331.	4.346	2.431	7.34
-1.1770	6.355	336.	4.395	2.494	7.42
-1.4270	6.384	324.	4.605	2.498	7.71
-1.5269	6.364	270.	4.454	2.031	7.52
-1.5769	6.298	235.	3.987	1.695	7.21
-1.6069	6.270	210.	3.783	1.514	7.21

TABLE C-19. HOT-WIRE DATA REDUCTION FOR RIJKE
CONFIGURATION, TEST NO.4 ,FITTING 13

R (IN)	VDC (VOLTS)	VAC (MVOLTS)	U (FPS)	UBAR (FPS)	S (FPS/VOLT)
1.5559	6.419	285.	4.896	2.289	8.03
1.3810	6.351	322.	4.367	2.376	7.37
1.2809	6.353	318.	4.381	2.353	7.40
1.0309	6.334	315.	4.247	2.266	7.19
0.7809	6.347	312.	4.339	2.287	7.33
0.5309	6.356	312.	4.402	2.320	7.43
0.2809	6.356	312.	4.402	2.320	7.43
0.0309	6.351	313.	4.367	2.309	7.37
-0.2190	6.339	315.	4.282	2.282	7.24
-0.4690	6.349	318.	4.353	2.339	7.35
-0.7190	6.355	319.	4.395	2.368	7.42
-0.9690	6.363	320.	4.448	2.404	7.51
-1.2190	6.362	325.	4.442	2.438	7.50
-1.4690	6.378	314.	4.556	2.404	7.65
-1.5690	6.423	281.	5.010	2.265	8.06
-1.6190	6.424	288.	5.018	2.321	8.05
-1.6389	6.322	220.	4.161	1.567	7.12

TABLE C-20. HOT-WIRE DATA REDUCTION FOR RIJKE
CONFIGURATION, TEST NO.5 ,FITTING 14

R (IN)	VDC (VOLTS)	VAC (MVOLTS)	U (FPS)	UBAR (FPS)	S (FPS/VOLT)
-1.4550	11.090	372.	7.200	1.914	5.14
-1.3250	11.920	540.	12.415	3.938	7.29
-1.2250	11.880	560.	12.122	4.117	7.35
-0.9750	11.180	560.	7.669	3.002	5.36
-0.7250	10.890	540.	6.184	2.559	4.73
-0.4749	10.850	530.	5.999	2.505	4.72
-0.2249	10.890	535.	6.184	2.535	4.73
0.0250	11.030	530.	6.891	2.746	5.18
0.2750	11.060	545.	7.046	2.809	5.15
0.5270	10.960	530.	6.527	2.699	5.09
0.7770	11.280	535.	8.226	3.076	5.75
1.0259	11.180	540.	7.669	2.895	5.36
1.2750	11.390	545.	8.870	3.211	5.89
1.5250	11.920	560.	12.415	4.084	7.29
1.6289	11.880	510.	12.122	3.749	7.35
1.6349	11.750	462.	11.165	3.336	7.22

TABLE C-21. HOT-WIRE DATA REDUCTION FOR RIJKE
CONFIGURATION, TEST NO.5 ,FITTING 15

R (IN)	VDC (VOLTS)	VAC (MVOLTS)	U (FPS)	UBAR (FPS)	S (FPS/VOLT)
-1.4510	10.260	107.	3.646	0.362	3.38
-1.3310	11.410	119.	8.988	0.701	5.89
-1.2310	11.780	135.	11.384	0.986	7.31
-0.9810	11.390	200.	8.870	1.178	5.89
-0.7310	10.880	161.	6.138	0.761	4.72
-0.4810	10.800	121.	5.758	0.574	4.74
-0.2309	10.960	105.	6.527	0.534	5.09
0.0190	11.090	97.	7.200	0.499	5.14
0.2690	11.000	100.	6.735	0.518	5.18
0.5190	11.190	107.	7.723	0.578	5.40
0.7690	11.110	107.	7.303	0.552	5.16
1.0190	11.190	108.	7.723	0.583	5.40
1.2690	11.340	148.	8.576	0.868	5.86
1.5190	11.200	147.	7.777	0.800	5.44
1.6139	11.110	123.	7.303	0.635	5.16
1.6349	10.990	102.	6.683	0.528	5.17

TABLE C-22. HOT-WIRE DATA REDUCTION FOR RIJKE
CONFIGURATION, TEST NO.5 ,FITTING 16

R (IN)	VDC (VOLTS)	VAC (MVOLTS)	U (FPS)	UBAR (FPS)	S (FPS/VOLT)
-1.4205	10.530	472.	4.611	1.802	3.81
-1.3270	11.310	590.	8.400	3.425	5.82
-1.2270	11.650	660.	10.466	4.428	6.71
-0.9769	11.430	690.	9.106	4.074	5.90
-0.7269	11.380	690.	8.812	4.064	5.89
-0.4769	10.990	670.	6.683	3.470	5.17
-0.2269	10.900	650.	6.231	3.097	4.76
0.0230	10.930	650.	6.375	3.201	4.92
0.2730	11.220	680.	7.887	3.760	5.53
0.5230	11.390	680.	8.870	4.007	5.89
0.7730	11.190	670.	7.723	3.619	5.40
1.0230	11.110	660.	7.303	3.407	5.16
1.2730	11.060	660.	7.046	3.402	5.15
1.5230	10.900	630.	6.231	3.002	4.76
1.6199	10.810	560.	5.806	2.664	4.75
1.6349	10.670	540.	5.173	2.292	4.24

TABLE C-23. HOT-WIRE DATA REDUCTION FOR RIJKE
CONFIGURATION, TEST NO.5 ,FITTING EXIT

R (IN)	VDC (VOLTS)	VAC (MVOLTS)	U (FPS)	UBAR (FPS)	S (FPS/VOLT)
-1.6349	11.200	560.	7.777	3.049	5.44
-1.5699	11.200	550.	7.777	2.994	5.44
-1.2699	11.240	635.	7.998	3.563	5.61
-0.9199	12.390	850.	15.852	6.259	7.36
-0.6699	12.220	900.	14.590	6.680	7.42
-0.4199	12.190	890.	14.368	6.572	7.38
-0.1699	12.340	890.	15.483	6.582	7.39
0.0000	12.030	865.	13.208	6.202	7.17
0.3300	12.120	790.	13.855	5.734	7.25
0.5800	12.200	770.	14.442	5.697	7.39
0.8300	12.320	720.	15.335	5.338	7.41
1.0800	12.190	650.	14.368	4.799	7.38
1.3300	11.500	600.	9.521	3.599	5.99
1.4300	11.400	570.	8.929	3.360	5.89
1.5099	11.400	520.	8.929	3.065	5.89

TABLE C-24. HEATER SURFACE TEMPERATURE
FOR RIJKE CONFIGURATION,
TEST NO.1, 1000 WATTS

POINT	RADIUS (IN.)	PLANE	TEMPERATURE (DEG.F)
1	1.540	A	1396.
2	1.070	A	1055.
3	0.531	A	1186.
4	0.000	A	1243.
5	-0.371	A	1296.
6	-0.728	A	1203.
7	-1.058	A	1180.
8	-1.370	A	1208.
9	-1.551	A	1320.
10			1365.
11	1.490	B	1396.
12	1.230	B	1202.
13	.952	B	1171.
14	.671	B	1217.
15	.372	B	1322.
16	0.224	B	1217.
17	-0.307	B	1151.
18	-0.573	B	1165.
19	-0.868	B	1465.
20	-1.169	B	1258.
21	-1.412	B	1189.
22	1.454	C	1595.
23	0.742	C	1273.
24	-0.797	C	1420.
25	-1.560	C	1117.
26	1.210	D	1415.
27	0.812	D	1211.
28	-0.770	D	1282.
29	-1.518	D	1147.
30	1.531	E	1529.
31	0.868	E	1281.
32	-0.511	E	1398.
33	-0.854	E	1330.
34	-1.218	E	1376.
35	-1.449	E	1123.
36	1.511	F	1393.
37	1.050	F	1336.
38	.357	F	1262.
39	-0.574	F	1120.
40	-0.952	F	1429.
41	-1.449	F	1187.

TABLE C-25. HEATER SURFACE TEMPERATURE
FOR RIJKE CONFIGURATION,
TEST NO.2, 1200 WATTS

POINT	RADIUS (IN.)	PLANE	TEMPERATURE (DEG.F)
1	1.540	A	1537.
2	1.070	A	1184.
3	0.531	A	1392.
4	0.000	A	1363.
5	-0.371	A	1401.
6	-0.728	A	1340.
7	-1.058	A	1305.
8	-1.370	A	1301.
9	-1.551	A	1471.
10			1566.
11	1.490	B	1631.
12	1.230	B	1402.
13	.952	B	1370.
14	.671	B	1408.
15	.372	B	1382.
16	0.224	B	1453.
17	-0.307	B	1283.
18	-0.573	B	1216.
19	-0.868	B	1545.
20	-1.169	B	1364.
21	-1.412	B	1340.
22	1.454	C	1571.
23	0.742	C	1413.
24	-0.797	C	1528.
25	-1.560	C	1268.
26	1.210	D	1583.
27	0.812	D	1290.
28	-0.770	D	1375.
29	-1.518	D	1317.
30	1.531	E	1497.
31	0.868	E	1431.
32	-0.511	E	1457.
33	-0.854	E	1420.
34	-1.218	E	1531.
35	-1.449	E	1334.
36	1.511	F	1513.
37	1.050	F	1506.
38	.357	F	1557.
39	-0.574	F	1208.
40	-0.952	F	1630.
41	-1.449	F	1347.

TABLE C-26. HEATER SURFACE TEMPERATURE
FOR RIJKE CONFIGURATION,
TEST NO.3, 1400 WATTS

POINT	RADIUS (IN.)	PLANE	TEMPERATURE (DEG.F)
1	1.540	A	1619.
2	1.070	A	1402.
3	0.531	A	1464.
4	0.000	A	1511.
5	-0.371	A	1582.
6	-0.728	A	1550.
7	-1.058	A	1517.
8	-1.370	A	1537.
9	-1.551	A	1595.
10			1759.
11	1.490	B	1645.
12	1.230	B	1581.
13	.952	B	1548.
14	.671	B	1527.
15	.372	B	1555.
16	0.224	B	1539.
17	-0.307	B	1331.
18	-0.573	B	1346.
19	-0.868	B	1148.
20	-1.169	B	1495.
21	-1.412	B	1512.
22	1.454	C	1214.
23	0.742	C	1517.
24	-0.797	C	1181.
25	-1.560	C	1335.
26	1.210	D	1136.
27	0.812	D	1448.
28	-0.770	D	1114.
29	-1.518	D	1280.
30	1.531	E	1214.
31	0.868	E	1510.
32	-0.511	E	1149.
33	-0.854	E	1556.
34	-1.218	E	1130.
35	-1.449	E	1387.
36	1.511	F	1102.
37	1.050	F	1526.
38	.357	F	1183.
39	-0.574	F	1544.
40	-0.952	F	1373.
41	-1.449	F	1316.

TABLE C-27. HEATER SURFACE TEMPERATURE
FOR RIJKE CONFIGURATION,
TEST NO.4, 1600 WATTS

POINT	RADIUS (IN.)	PLANE	TEMPERATURE (DEG.F)
1	1.540	A	1650.
2	1.070	A	1294.
3	0.531	A	1369.
4	0.000	A	1498.
5	-0.371	A	1370.
6	-0.728	A	1430.
7	-1.058	A	1359.
8	-1.370	A	1462.
9	-1.551	A	1542.
10			1687.
11	1.490	B	1618.
12	1.230	B	1410.
13	.952	B	1438.
14	.671	B	1449.
15	.372	B	1445.
16	0.224	B	1629.
17	-0.307	B	1447.
18	-0.573	B	1459.
19	-0.868	B	1288.
20	-1.169	B	1636.
21	-1.412	B	1470.
22	1.454	C	1445.
23	0.742	C	1540.
24	-0.797	C	1332.
25	-1.560	C	1524.
26	1.210	D	1467.
27	0.812	D	1562.
28	-0.770	D	1379.
29	-1.518	D	1405.
30	1.531	E	1454.
31	0.868	E	1547.
32	-0.511	E	1180.
33	-0.854	E	1553.
34	-1.218	E	1171.
35	-1.449	E	1510.
36	1.511	F	1242.
37	1.050	F	1553.
38	.357	F	1303.
39	-0.574	F	1396.
40	-0.952	F	1472.
41	-1.449	F	1645.

TABLE C-28. MICROPHONE DATA REDUCTION FOR
SONDHAUSS CONFIGURATION TEST NO.22

FITTING NUMBER	FREQUENCY (HERTZ)	SOUND PRESSURE LEVEL (DB)	SOUND PRESSURE (LB/SQ IN)
1	79.20	111.43	0.1070E-02
2	79.20	122.31	0.3746E-02
3	79.60	130.98	0.1016E-01
4	79.80	133.01	0.1284E-01
5	80.20	134.35	0.1497E-01
6	80.40	135.23	0.1658E-01
7	80.60	136.28	0.1871E-01
8	80.80	137.00	0.2031E-01
9	81.10	137.44	0.2138E-01
10	81.30	137.86	0.2244E-01

TABLE C-29. MICROPHONE DATA REDUCTION FOR
SONDHAUSS CONFIGURATION TEST NO.20

FITTING NUMBER	FREQUENCY (HERTZ)	SOUND PRESSURE LEVEL (DB)	SOUND PRESSURE (LB/SQ IN)
1	80.90	136.94	0.2020E-01
2	80.80	136.71	0.1967E-01
3	80.80	135.98	0.1807E-01
4	80.90	135.45	0.1701E-01
5	80.80	134.89	0.1594E-01
6	80.90	133.65	0.1382E-01
7	80.90	132.20	0.1169E-01
8	80.90	128.02	0.7229E-02
9	80.90	117.39	0.2126E-02
10	80.90	111.19	0.1041E-02

TABLE C-30. HOT-WIRE DATA REDUCTION, SONDHAUSS
CONFIGURATION, TEST NO. 21, FITTING 13
SENSOR POINTING TOWARD HEATER

R (IN)	VDC (VOLTS)	VAC (MVOLTS)	U (FPS)	UBAR (FPS)	S (FPS/VOLT)
1.6170	5.630	116.	0.801	0.311	2.68
1.5810	5.620	120.	0.775	0.319	2.66
1.4809	5.660	125.	0.883	0.345	2.76
1.2809	5.670	126.	0.911	0.351	2.79
1.0309	5.670	133.	0.911	0.371	2.79
0.7809	5.700	132.	0.996	0.380	2.88
0.2809	5.670	124.	0.911	0.346	2.79
0.0309	5.670	127.	0.911	0.354	2.79
-0.2190	5.710	126.	1.024	0.367	2.91
-0.7190	5.690	121.	0.967	0.344	2.84
-0.9690	5.710	125.	1.024	0.364	2.91
-1.2190	5.670	129.	0.911	0.360	2.79
-1.4690	5.640	125.	0.828	0.339	2.71
-1.5690	5.550	105.	0.593	0.264	2.52
-1.6190	5.490	96.	0.446	0.230	2.40

TABLE C-31. HOT-WIRE DATA REDUCTION, SONDHAUSS
CONFIGURATION, TEST NO. 21, FITTING 13
SENSOR POINTING AWAY FROM HEATER

R (IN)	VDC (VOLTS)	VAC (MVOLTS)	U (FPS)	UBAR (FPS)	S (FPS/VOLT)
1.6170	5.670	116.	0.911	0.323	2.79
1.5810	5.780	120.	1.237	0.383	3.19
1.4809	5.660	125.	0.883	0.345	2.76
1.2809	5.690	126.	0.967	0.358	2.84
1.0309	5.640	133.	0.828	0.360	2.71
0.7809	5.670	132.	0.911	0.368	2.79
0.2809	5.640	124.	0.828	0.336	2.71
0.0309	5.650	127.	0.856	0.347	2.73
-0.2190	5.660	126.	0.883	0.348	2.76
-0.7190	5.650	121.	0.856	0.331	2.73
-0.9690	5.660	125.	0.883	0.345	2.76
-1.2190	5.700	129.	0.996	0.371	2.88
-1.4690	5.700	125.	0.996	0.360	2.88
-1.5690	5.720	105.	1.054	0.309	2.94
-1.6190	5.580	96.	0.670	0.247	2.58

TABLE C-32. HOT-WIRE DATA REDUCTION, SONDHAUSS
CONFIGURATION, TEST NO. 21, FITTING 14
SENSOR POINTING TOWARD HEATER

R (IN)	VDC (VOLTS)	VAC (MVOLTS)	U (FPS)	UBAR (FPS)	S (FPS/VOLT)
1.6152	5.680	125.	0.939	0.352	2.81
1.5480	5.670	134.	0.911	0.373	2.79
1.5230	5.700	137.	0.996	0.394	2.88
1.4230	5.670	133.	0.911	0.371	2.79
1.3230	5.690	139.	0.967	0.396	2.84
1.0980	5.680	135.	0.939	0.380	2.81
0.8230	5.660	135.	0.883	0.373	2.76
0.3230	5.680	131.	0.939	0.369	2.81
0.0729	5.690	131.	0.967	0.373	2.84
-0.1770	5.690	131.	0.967	0.373	2.84
-0.6770	5.680	126.	0.939	0.355	2.81
-0.9270	5.710	131.	1.024	0.381	2.91
-1.1770	5.730	131.	1.083	0.391	2.98
-1.4270	5.650	125.	0.856	0.342	2.73
-1.5269	5.560	94.	0.619	0.238	2.54
-1.5769	5.470	86.	0.398	0.203	2.36

TABLE C-33. HOT-WIRE DATA REDUCTION, SONDHAUSS
CONFIGURATION, TEST NO. 21, FITTING 14
SENSOR POINTING AWAY FROM HEATER

R (IN)	VDC (VOLTS)	VAC (MVOLTS)	U (FPS)	UBAR (FPS)	S (FPS/VOLT)
1.6152	5.705	125.	1.010	0.362	2.89
1.5480	5.650	127.	0.856	0.347	2.73
1.5230	5.660	137.	0.883	0.378	2.76
1.4230	5.690	133.	0.967	0.378	2.84
1.3230	5.680	139.	0.939	0.391	2.81
1.0980	5.640	135.	0.828	0.366	2.71
0.8230	5.650	135.	0.856	0.369	2.73
0.3230	5.630	131.	0.801	0.352	2.68
0.0729	5.650	131.	0.856	0.358	2.73
-0.1770	5.640	130.	0.828	0.352	2.71
-0.6770	5.680	126.	0.939	0.355	2.81
-0.9270	5.730	131.	1.083	0.391	2.98
-1.1770	5.730	131.	1.083	0.391	2.98
-1.4270	5.720	125.	1.054	0.368	2.94
-1.5269	5.730	94.	1.083	0.280	2.98
-1.5769	5.640	86.	0.828	0.233	2.71

TABLE C-34. HOT-WIRE DATA REDUCTION, SONDHAUSS
CONFIGURATION, TEST NO. 21, FITTING 15
SENSOR POINTING TOWARD HEATER

R (IN)	VDC (VOLTS)	VAC (MVOLTS)	U (FPS)	UBAR (FPS)	S (FPS/VOLT)
1.5190	5.670	105.	0.911	0.293	2.79
1.2929	5.700	99.	0.996	0.285	2.88
0.7929	5.740	105.	1.113	0.317	3.02
0.2929	5.750	116.	1.144	0.355	3.06
0.0429	5.740	108.	1.113	0.326	3.02
-0.2070	5.710	115.	1.024	0.335	2.91
-0.7070	5.680	105.	0.939	0.296	2.81
-1.2070	5.650	96.	0.856	0.262	2.73
-1.4070	5.490	80.	0.446	0.192	2.40

TABLE C-35. HOT-WIRE DATA REDUCTION, SONDHAUSS
CONFIGURATION, TEST NO. 21, FITTING 17
SENSOR POINTING TOWARD HEATER

R (IN)	VDC (VOLTS)	VAC (MVOLTS)	U (FPS)	UBAR (FPS)	S (FPS/VOLT)
1.4560	5.750	140.	1.144	0.428	3.06
1.3980	5.830	135.	1.403	0.468	3.47
1.2980	5.780	135.	1.237	0.431	3.19
0.7979	5.700	150.	0.996	0.432	2.88
0.2979	5.720	105.	1.054	0.309	2.94
0.0479	5.710	105.	1.024	0.305	2.91
-0.2020	5.720	85.	1.054	0.250	2.94
-0.7020	5.710	110.	1.024	0.320	2.91
-1.2020	5.700	105.	0.996	0.302	2.88
-1.4520	5.480	50.	0.422	0.119	2.38

APPENDIX D

DATA REDUCTION

All test data taken during this experimental program was hand recorded, keypunched on cards and subsequently processed through a number of digital computer programs. The computer programs were very simple and will not be reproduced here. Instead, the basic equations that were used will be explained in this appendix.

Microphone Probe

The sound pressure level, SPL, was calculated using equation [D-1].

$$\text{SPL} = 124.1 - S_m + 20 \log_{10} \text{SPV} + \Delta_f + \Delta_{\text{amb}} \quad [\text{D-1}]$$

In equation [D-1], SPL is in db re 0.0002 μ bars, SPV is the sound pressure signal in volts, S_m is the microphone sensitivity in db re 1 volt/ μ bar, Δ_{abm} is the ambient pressure correction and Δ_f is the change in microphone sensitivity due to the response of the probe tube as given in figure 22. Equation [D-2] was used to compute the sound pressure in psia.

$$p = 2.87 \times 10^{-9} \exp (\text{SPL}/8.68589) \quad [\text{D-2}]$$

Hot Wire Calibration

The procedure for calibrating the hot-wire probe using a laminar flow tube is outlined in Chapter III. With reference to the flow schematic given in figure 29, the mass flow rate through the orifice is given by equation [D-3] in terms of orifice upstream pressure, differential pressure and temperature. The orifice calibration coefficient, β_{ori} ,

$$m_L = \frac{\beta_{ori} P_{ori}}{\sqrt{T_{ori} + 459.7}} \quad [D-3]$$

is given by a pair of polynomial curve fits with $\Delta P_{ori}/P_{ori}$ as the independent variable.

For $\Delta P_{ori}/P_{ori} \leq 0.01$,

$$N_p = K_1 (P_{ori}/P_{ori}) + K_2$$

$$m_{ori} = C_1 + C_2 N_p + C_2 N_p^2 + \dots C_5 N_p^4 \quad [D-4]$$

$$\text{where, } K_1 = 2.222222 \times 10^1$$

$$K_2 = -1.0$$

$$C_1 = 4.712143 \times 10^{-4}$$

$$C_2 = 2.245352 \times 10^{-4}$$

$$C_3 = -5.719293 \times 10^{-5}$$

$$C_4 = 4.81703 \times 10^{-5}$$

$$C_5 = -2.776719 \times 10^{-5}$$

For $0.01 < P_{ori}/P_{ori} \leq 0.9$,

$$K_1 = 200.$$

$$K_2 = -1.0$$

$$C_1 = 1.57 \times 10^{-4}$$

$$C_2 = 8.599999 \times 10^{-5}$$

$$C_3 = -1.50 \times 10^{-5}$$

$$C_4 = 2.8 \times 10^{-5}$$

$$C_5 = -2.79999 \times 10^{-5}$$

In equations [D-3] and [D-4], P_{ori} has units of psia, ΔP_{ori} has units of psi and the T_{ori} has units of deg F. Temperature measurements were recorded in milli-volts and converted to deg F using NBS conversion charts.

The mean velocity across the hot-wire placed in the calibrating stream was calculated from equation D-5.

$$U_{cal} = \left(\frac{\bar{v}}{\bar{v}} \right) \left(\frac{8 R}{\pi D_L^2} \right) \frac{\dot{m}_L T_{blk}}{p_{amb}} \quad [D-5]$$

In this equation (\bar{v}/\bar{v}) and D_L are obtained from Table 9, T_{blk} is the temperature of the air stream in deg F measured at the calibrating block and p_{amb} is the ambient pressure in psia.

Results from [D-5] and measured hot-wire voltages were used to construct the hot-wire calibration curves, figures 31 and 32.

Velocity Calculations

The hot-wire calibration curves were curve fitted using polynomial equations and sectioned for greater accuracy. Because of the numerous coefficients involved, the curve fit equations will not be given here.

Time mean velocity, U , was calculated from the appropriate calibration curve by using the measured bridge DC voltage (V_{DC}). The fluctuating velocity was calculated from the AC RMS bridge voltage and hot-wire sensitivity using equation [D-6]. Hot-wire sensitivities were computed

$$\bar{u} = \frac{V_{AC}}{S_{hw}} \quad [D-6]$$

by taking the first derivative of the appropriate calibration curve fit equation and evaluating it at the corresponding bridge DC voltage. However, the first derivative was approximated by taking differentials of velocity and voltage at the point in question.

Mass Flow Calculation

The mass flow rate through the Rijke device was calculated at the plane of fittings 2, 12 and 13 by using profiles of the measured gas

temperature and velocity and assuming that the pressure was ambient. The continuity equation, [D-7], is the starting point for the calculation.

$$\dot{m} = \int_0^{D/2} \int_0^{2\pi} \rho(r) U_o(r) r d\phi dr \quad [D-7]$$

If we assume that measured values of gas temperature and velocity are constant from $\pi/4$ to $-\pi/4$ of the line of measurement (I), the integral from 0 to 2π can be replaced by a sum over the 4 quadrants of a circle as shown in Figure D-1. The integral in the r direction was replaced by quadrature. The simple trapezoidal rule was found to be sufficient for this task. The final relationship used to calculate the mass flow rate is given by equation [D-8], where the perfect gas law has been used for the density.

$$\dot{m} = \left(\frac{\pi}{2R} \right) P_{amb} \sum_1^4 \sum_0^{D/2} \bar{F}(r) \Delta r \quad [D-8]$$

where,

$$F(r) = \frac{r U(r)}{T(r)} \quad [D-9]$$

and,

$$\bar{F}(r) = \frac{1}{2} \left[F\left(r + \frac{\Delta r}{2}\right) + F\left(r - \frac{\Delta r}{2}\right) \right] \quad [D-10]$$

In this procedure, $U_o(r)$ and $T(r)$ were input into an interpolation table and evaluated by using second order interpolation.

Bulk Temperature Calculation

The bulk average temperature was calculated from measured values of gas temperature, velocity and calculated mass flow rate. Equation [D-11] was used for that purpose.

$$T_{av} = \frac{\bar{C}_p \int_0^{D/2} \int_0^{2\pi} T(r) \rho(r) U_o(r) r d\phi dr}{\bar{C}_p \int_0^{D/2} \int_0^{2\pi} \rho(r) U_o(r) r d\phi dr} \quad [D-11]$$

The double integral in the denominator of equation D-11 is recognized to be equal to \dot{m} . Following the same line of reasoning as for the mass flow calculation, the final equation for average temperature is given by equation [D-12] .

$$T_{av} = \left(\frac{\pi}{2\theta} \right) \frac{P_{amb}}{\dot{m}} \sum_1^4 \sum_0^{D/2} \bar{G}(r) \Delta r \quad [D-12]$$

where,

$$G(r) = \frac{T(r) U_o(r) r}{(T_r + 460)} \quad [D-13]$$

and,

$$\bar{G}(r) = \frac{1}{2} \left[G(r + \frac{\Delta r}{2}) + G(r - \frac{\Delta r}{2}) \right] \quad [D-14]$$

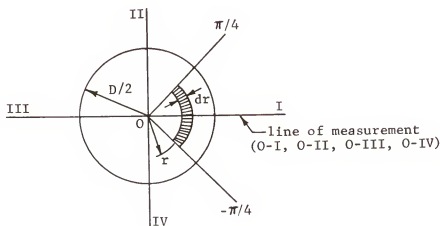


Figure D-1. Geometry for mass flow calculation.

The bulk average density and velocity are given by [D-15] and [D-16] respectively.

$$\rho_{av} = \frac{p_{atm}}{R T_{av}} \quad [D-15]$$

$$U_{av} = \frac{\dot{m}}{\rho_{av} \pi D^2/4} \quad [D-16]$$

BIBLIOGRAPHY

1. Higgins, B., Nicholson's Journal I, 130 (1802).
2. Sondhauss, C., "Über die Schallschwingungen der Luft in erhitzten Glasrohren und in gedeckten Pfeifen von ungleicher Weite," Annln Phys. 79, 1 (1850).
3. Rijke, P.L., "Notiz über eine neue Art, die in einer an beiden Enden offenen Rohre enthaltene Luft in Schwingungen zu versetzen," Annln Phys. 107, 339 (1859).
4. Clement, J.R. and J. Gaffney, "Thermal Oscillations in Low Temperature Apparatus," Advances in Cryo. Engrg. 1, 302 (1954).
5. Bannister, J.D., "Spontaneous Pressure Oscillations in Tubes Connecting Liquid Helium Reservoirs to 300°K Environments," Bull. Int. Instr. of Refr. Annexe, 1966-5 (1966).
6. Ditmars, D.A. and T.G. Furukawa, "Detection and Damping of Thermal-Acoustic Oscillations in Low Temperature Apparatus," J. of Res., N.B.S. 69C, 38 (1964).
7. Thurston, R.S., "Probing Experiments on Pressure Oscillations in Two-Phase and Supercritical Hydrogen with Forced Convection Heat Transfer," Adv. in Cryogenic Engrg. 10, 305 (1965).
8. Kaminski, W.R. et al., "JP-7 Regenerative Cooling Investigation," Pratt and Whitney Aircraft, Florida Research and Development Center Report, SMR FR-3607, (1970).
9. Mawardi, O.K., "On Thermoacoustic Transduction in a Potential Flow," J. Acoustic Soc. Am. 28, No. 2, 239 (1956).
10. Lord Rayleigh, Theory of Sound, Dover Publications, 1954 re-issue, Volume II, New York.
11. Putnam, A.A. and W.R. Dennis, "Survey of Organ-Pipe Oscillations in Combustion Systems," J. Acoustic Soc. Am. 28, No. 2, 246 (1956).
12. Chu, B.T., "Stability of Systems Containing a Heat Source - The Rayleigh Criterion," NACA RM 56D27 (1956).
13. Kerwin, E.M., Jr., "A Study of a Class of Thermoacoustical Oscillations," Sc. D. Dissertation, Massachusetts Institute of Technology (1954).

14. Carrier, G.F., "The Mechanics of the Rijke Tube," Q. Appl. Math. 12, 383 (1955).
15. Merk, H.J., "Analysis of Heat Driven Oscillations of Gas Flow," Part I and II, Appl. Scient. Res. A6, 317, 402 (1956).
16. Feldman, K.T., Jr., "Review of the Literature on Rijke Thermoacoustic Phenomena," J. Sound Vib. 7, (1), 83-99 (1968).
17. Feldman, K.T., Jr., "Review of the Literature on Sondhauss Thermoacoustic Phenomena," J. Sound Vib. 7, (1), 72-83 (1968).
18. Mawardi, O.K., "Aero-Thermoacoustics (The Generation of Sound by Turbulence and by Heat Processes)," Reports on Progress in Physics 19, 156 (1956).
19. Kovasznyai, L.S.G., "Turbulence in Supersonic Flow," J. Aero. Sci. 20, No. 10, Oct., 657-682 (1953).
20. Maling, G.C., Jr., "A Study of the Propagation of Acoustic Waves and Instabilities in Inhomogeneous Media," Ph.D. Dissertation, Physics Department, M.I.T. (1963).
21. Friedlander, M.M. and Smith, T.J.B., "Experiments on the Rijke Tube Phenomenon," J. Acoust. Soc. Am. 36, 1737 (1964).
22. Kramers, H.A., "Vibrations of a Gas Column," Physica, 's Grav. 15, 971 (1949).
23. Carter, R.L., et. al., "Applicability of Thermoacoustic Phenomena to MHD Conversion Systems," University of Missouri Engineering Experiment Station, Reprint No. 64 (1964).
24. Feldman, K.T., Jr., "A Study of Heat Generated Pressure Oscillations in a Closed End Pipe," Ph.D. Dissertation, Mechanical Engineering, University of Missouri (1966).
25. Carter, R.L. and K.T. Feldman, Jr., "A Study of Heat Driven Pressure Oscillations in a Gas," ASME Paper No. 69-WA/HT-11 (1969).
26. Pohl, J.H., "Thermally Induced Acoustic Oscillations Caused by "Steep" Temperature Gradients," Ph.D. Dissertation, Mechanical Engineering, University of Florida (1971).
27. Lehmann, K.O., "Über die Theorie der Netztöne," Annln Phys. 421, 527 (1937).
28. Allan, J., Private Communication.
29. Gubareff, G.G. et al., Thermal Radiation Properties Survey, Honeywell Research Center, Minneapolis, Minnesota, (1960).

30. Hinze, J.O., Turbulence, an Introduction to its Mechanisms and Theory, McGraw-Hill (1959).
31. Rasmussen, C.G., "The Air Jet Hot-Wire Microphone," DISA Information No. 4, 30-35 (1966).
32. Kinsler, L.E., Frey, A.R., Fundamentals of Acoustics, 2nd Edition, John Wiley and Sons, Inc., New York (1962).
33. Ingard, K.U. and P.M. Morse, "Linear Acoustic Theory," Encyclopedia of Physics, Vol. XI/1, Acoustics I, Edited by S. Flugge, Springer-Verlag (1961).
34. Colbert, D.L. et al., "ICRPG Measurement Uncertainty Handbook for Liquid Rocket Engines," CPIA 180, AD 851127, (PWA FR-2974B) (1969).

BIOGRAPHICAL SKETCH

Walter Reginald Kaminski was born in Hamtramck, Michigan, on December 1, 1935. He was the first child by Mr. and Mrs. Walter M. Kaminski, and has one sister, Mrs. Elizabeth Ann Burk. Mr. Kaminski attended the St. Ladislaus Elementary and High Schools where he participated in athletics and had the distinction of being elected class president for all four years.

Mr. Kaminski attended the University of Detroit, Detroit, Michigan from September, 1953 to June, 1959, where he received a co-operative mechanical engineering education. He was employed by the Continental Aviation and Engineering Corporation during his co-operative training assignment. Upon graduation from the University of Detroit, with a B.M.E. degree, he joined the Holley Carburetor Company and worked in the Research and Advanced Engineering Department. While at Holley Carburetor, Mr. Kaminski attended the University of Michigan, Ann Arbor, Michigan, and received an M.S.E. degree in December, 1963.

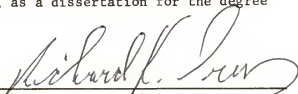
In August, 1964, Mr. Kaminski joined the Pratt & Whitney Aircraft, Florida Research and Development Center to work in the Applied Research Department. Mr. Kaminski is currently an Assistant Project Engineer assigned to the Applied Research Combustor Group and is responsible for turbine exhaust pollution emission investigations.

In September, 1969, Mr. Kaminski enrolled at the University of Florida and entered the Doctoral Program in Mechanical Engineering. His studies were sponsored by the Pratt & Whitney Aircraft Company. A year

later Mr. Kaminski was granted a leave-of-absence from Pratt & Whitney to attend the University of Florida on a full-time basis. After completing his course work on campus, Mr. Kaminski returned to Pratt & Whitney where he subsequently completed his dissertation.

On November 22, 1958, Mr. Kaminski married the former Mary Jane Armstrong of Ferndale, Michigan. They have six children, Michael, Mark, Elaine, Jane, Karen and Donna. The family resides in North Palm Beach, Florida.


I certify that I have read this study and that in my opinion it conforms to acceptable standards of scholarly presentation and is fully adequate, in scope and quality, as a dissertation for the degree of Doctor of Philosophy


Richard K. Ireys, Chairman
Professor of Mechanical Engineering

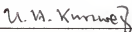
I certify that I have read this study and that in my opinion it conforms to acceptable standards of scholarly presentation and is fully adequate, in scope and quality, as a dissertation for the degree of Doctor of Philosophy.


Calvin C. Oliver
Professor of Mechanical Engineering

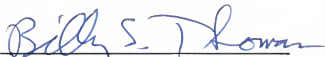
I certify that I have read this study and that in my opinion it conforms to acceptable standards of scholarly presentation and is fully adequate, in scope and quality, as a dissertation for the degree of Doctor of Philosophy.


Roger A. Gater
Associate Professor of Mechanical
Engineering

I certify that I have read this study and that in my opinion it conforms to acceptable standards of scholarly presentation and is fully adequate, in scope and quality, as a dissertation for the degree of Doctor of Philosophy.


Ulrich H. Kurzweg
Associate Professor of Engineering
Science and Mechanics

I certify that I have read this study and that in my opinion it conforms to acceptable standards of scholarly presentation and is fully adequate, in scope and quality, as a dissertation for the degree of Doctor of Philosophy.

A handwritten signature in blue ink, reading "Billy S. Thomas".

Billy S. Thomas
Assistant Professor of Physics

This dissertation was submitted to the Dean of the College of Engineering and to the Graduate Council, and was accepted as partial fulfillment of the requirements for the degree of Doctor of Philosophy.

December, 1972

A handwritten signature in blue ink, reading "Robert E. Wherry".
Dean, College of Engineering

Dean, Graduate School